

PLASMONIC MICROSTRUCTURED  
OPTICAL FIBRES

—

AN EFFICIENT PLATFORM TOWARDS BIOSENSING

---

**DISSERTATION**

for the acquisition  
of the academic title

**Doctor rerum naturalium (Dr. rer. nat.)**

submitted to the council of the  
**Faculty of Physics and Astronomy**

of the



**FRIEDRICH-SCHILLER-  
UNIVERSITÄT  
JENA**

by MSc. **BRENDA DOHERTY**

born on 29th of March 1990, in Waterford, Ireland

**REVIEWERS:**

1. Prof. Dr. Markus A. Schmidt  
Friedrich-Schiller-Universität Jena, Germany
2. Prof. Dr. Rachel Grange  
Swiss Federal Institute of Technology Zürich, Switzerland
3. Jun. Prof. Dr. Isabelle Staude  
Friedrich-Schiller-Universität Jena, Germany

**DATE OF THE DISPUTATION: 17th of March 2020**

## ABSTRACT

---

Detecting life-threatening diseases is a major challenge in biomedicine, as it requires pathogen identification on the molecular level. One promising detection strategy relies on attaching molecular probes to nanoparticles (NPs). The NPs' electron ensemble is collectively excited by an external electromagnetic wave at a characteristic wavelength, creating localised surface plasmon resonances (LSPRs). Probe-functionalised NPs can then detect molecular DNA-binding events via a macroscopic change of the optical plasmonic response. Until now, NP-sensing schemes have been primarily implemented using planar substrates, requiring complex launching techniques and cost-intensive microscopy. An alternative approach involves infiltrating optical fibres with NPs allowing LSPR excitation and spectral multiplexing within one device. Fibres principally enable *in vivo* application, rendering them an attractive platform for medical needs. An important class of innovative fibres exploited in this work are microstructured optical fibres (MOFs), which can include either longitudinally invariant microstructures or optically resonant elements. Their complex self-contained geometry allows analyte infiltration, mechanical stability, and a high degree of sensitivity.

This thesis assesses the feasibility of a plasmonic biosensor based on suspended-core (SC-) MOFs, with outlook for future DNA biosensing application. The concept in its entirety is to combine label-free NP-based molecular DNA-sensing with MOFs and apply the sensors to detect a real world life-threatening disease, i.e. connecting the molecular level via LSPR-mediated sensing with the macroscopic world. A study of the homogeneous functionalisation of the interior capillary walls of a tri-hole suspended-core fibre (SCF), and the open channel of an exposed-core SCF, with various gold nanosphere densities is presented. Subsequent LSPR excitation is generated by overlap with the evanescent field of the core guided mode fields. This work theoretically and experimentally investigates the sensitivity offered by small core suspended-core MOFs. The impact of parameters such as modal scattering area and attenuation with varying core sizes is assessed. The resulting plasmonic-induced attenuation from multiple ensemble densities is shown experimentally and optofluidic strategies for sensing are addressed. The sensitivity of the complete plasmonic fibre system is calculated and verified experimentally. Furthermore, the generation of LSPR modes and subsequent binding induced resonance shifts of capture and target single strand (ss) DNA are shown on planar substrate. Preliminary work for near-future disease detection via nucleic acid plasmonic MOF sensing is laid.

This study shows that combining plasmonically-active fibre waveguides with microfluidics represents an easy to use, highly integrated, optofluidic platform for efficient refractive index (RI) sensing. The system requires low sample volumes and allows for real-time analyte monitoring, high sensitivity, and spectral multiplexing with the vision for *in vivo* application. All of which are highly relevant for molecular disease diagnostics and environmental science.

## ZUSAMMENFASSUNG

---

Die Identifikation von Pathogenen auf molekularer Ebene bildet heutzutage die Grundlage zur Detektion lebensgefährlicher Krankheiten und stellt somit eine der Hauptherausforderungen moderner Biomedizin dar. Eine vielversprechende Strategie zur Detektion basiert hierbei auf der Verbindung von molekularen Sensoren mit Nanopartikeln (NPs). Dabei wird das Elektronenensemble der NP kollektiv durch eine externe elektromagnetische Welle charakteristischer Wellenlänge angeregt, wodurch lokalisierte Oberflächenplasmonenresonanzen (engl. "localized surface plasmon resonances", LSPR) entstehen. Funktionalisierte Sensor-NP Verbindungen detektieren dann Events molekularer DNS-Bindung mittels einer makroskopischen Veränderung in der optischen Plasmonenantwort. Bisher wurden Konfigurationen von NP-Sensoren hauptsächlich mittels planarer Substrate implementiert, was komplexe Einkopplungsverfahren und kostenintensive Mikroskopieverfahren bedingt. Ein alternativer Ansatz basiert auf der Kombination von optischen Fasern mit NPn, so dass die Anregung von LSPR und spektrales Multiplexing in einem einzelnen Bauteil zusammengefasst werden können. Die in vivo Anwendbarkeit der Fasern macht sie gleichzeitig zu einer attraktiven Lösung für medizinische Untersuchungen. Eine wichtige Klasse neuartiger Fasern stellen sogenannte mikrostrukturierte optische Fasern (MOFs) dar, welche in der vorliegenden Arbeit untersucht werden. Sie zeichnen sich dadurch aus, dass sie entweder longitudinal invariante Mikrostrukturen oder optisch resonante Elemente enthalten. Zusätzlich ermöglicht ihre komplexe, in sich geschlossene Geometrie die Befüllung mit einer Analytlösung, mechanische Stabilität und eine hohe Messgenauigkeit.

Diese Dissertation bewertet die Umsetzbarkeit von plasmonischen Biosensoren auf der Basis von MOFs mit frei-aufgehängtem Kern (engl. "suspended core", SC-) mit Ausblick auf künftige Anwendung zur gezielten DNS-Detektion. Das Konzept beruht hierbei darauf, NP-basierte molekulare DNS-Sensorik mit MOFs zu kombinieren, ohne zusätzliche Marker zu verwenden. Die Brücke zwischen makroskopischer Welt und Strukturen auf molekularer Ebene wird dabei mittels LSPR geschlagen. Die homogene Funktionalität an den inneren Kapillarwänden einer SC-MOF mit drei Kanälen, sowie am offenen Kanal eines exponierten Kerns (engl. "exposed core", EC-) einer SC-MOF wird in Bezug auf verschiedene Teilchendichten von Goldnanosphären untersucht. Eine Anregung von LSPR wird anschließend durch Überlagerung mit dem Evaneszenzfeld der Kernmode erzielt. Die vorliegende Arbeit untersucht dazu theoretisch sowohl experimentell die Sensitivität von SC-MOFs mit kleinen Kerndurchmessern. Die Wirkung von Parametern wie der modalen Streufläche und Dämpfung wird analysiert. Die resultierende Plasmon-induzierte Dämpfung von verschiedenen Ensembledichten wird experimentell aufgezeigt und optofluide Strategien zur Sensorik werden diskutiert. Die Sensitivität des gesamten plasmonischen Fasersystems wird berechnet und experimentell bestätigt. Darüber hinaus werden gezielt adressierte Bindungsübergänge auf planaren Substraten

vorgestellt und die Vorarbeit für künftige in vivo Krankheitsdetektion mittels *nucleic acid plasmonic MOF sensing* geleistet.

Die vorliegende Arbeit demonstriert, dass die Kombination von plasmonisch aktiven Faserwellenleitern mit Mikrofluidik ein einfach zu nutzendes, hoch-integriertes, optofluides Verfahren zur effizienten Messung des Brechungsindex darstellt. Hierbei benötigt das verwendete System nur kleine Probenmengen und erlaubt dabei Echtzeitkontrolle des Analyten, hohe Sensitivität und spektrales Multiplexing mit Aussicht auf in vivo Anwendung – alles essentielle Aspekte der molekularen Krankheitsdiagnose und der Umweltwissenschaften allgemein.

## ACRONYMS

---

<b>AFM</b> atomic force microscopy	<b>OSA</b> optical spectrum analyser
<b>APTES</b> (3-aminopropyl)triethoxysilane	<b>PAH</b> poly(allylamine hydrochloride)
<b>CB</b> citrate buffer	<b>PCF</b> photonic crystal fibre
<b>CVD</b> chemical vapour deposition	<b>PDDA</b> poly(diallyldimethylammonium chloride)
<b>DDA</b> discrete dipole approximation	<b>PDMS</b> polydimethylsiloxane
<b>DNA</b> deoxyribonucleic acid	<b>PE</b> polyelectrolyte
<b>dsDNA</b> double strand DNA	<b>PEL</b> polyelectrolyte layers
<b>EC-</b> exposed core	<b>PROSI</b> n-propyltriethoxysilane
<b>ECF</b> exposed core fibre	<b>PSS</b> poly(sodium 4-styrenesulfonate)
<b>EM</b> electromagnetic	<b>PTFE</b> polytetrafluoroethylene
<b>FBG</b> fibre bragg grating	<b>RI</b> refractive index
<b>FDTD</b> finite time domain	<b>RIU</b> refractive index unit
<b>FEM</b> finite element method	<b>RNA</b> ribonucleic acid
<b>FIB</b> focussed ion beam	<b>SAM</b> self-assembled monolayer
<b>FOM</b> figure of merit	<b>SC-</b> suspended core
<b>FWHM</b> full width at half maximum	<b>SCF</b> suspended core fibre
<b>ID</b> internal diameter	<b>SEM</b> scanning electron microscopy
<b>LOD</b> limit of detection	<b>SP</b> surface plasmon
<b>LSPR</b> localised surface plasmon resonance	<b>SPP</b> surface plasmon polariton
<b>MCH</b> 6-mercapto-1-hexanol	<b>SPR</b> surface plasmon resonance
<b>MIR</b> mid infrared	<b>SSC</b> saline sodium citrate
<b>MG</b> Maxwell-Garnett	<b>ssDNA</b> single strand DNA
<b>MOF</b> microstructured optical fibre	<b>TEM</b> transmission electron microscopy
<b>M-TIR</b> modified total internal reflection	<b>TIR</b> total internal reflection
<b>MW</b> microwave	<b>TSC</b> trisodiumcitrate dihydrate
<b>NIR</b> near-infrared	<b>UV</b> ultraviolet
<b>NLD</b> nanoparticle layer deposition	<b>VIS</b> visible
<b>NP</b> nanoparticle	<b>WGM</b> whispering gallery mode
<b>NVOC</b> nitroveratryloxycarbonyl chloride	
<b>OFM</b> optofluidic mount	

## NOMENCLATURE

---

$\alpha$	polarisability
$A_{\text{eff}}$	modal scattering area
$\beta$	propagation constant
$C_{\text{ext}}$	extinction cross section
$C_{\text{sca}}$	scattering cross section
$C_{\text{abs}}$	absorption cross section
$d_{\text{NP}}$	nanoparticle diameter
$\varepsilon$	permittivity
$\gamma$	modal attenuation
$\lambda_{\text{peak}}$	resonance peak wavelength
$l_{\text{D}}$	penetration depth
$n$	refractive index
$n_{\text{eff}}$	effective refractive index
$N$	nanoparticle number density
$NA$	numerical aperture
$\omega$	angular frequency
$r_{\text{f}}$	fibre radius
$V$	(guidance) V-parameter

# CONTENTS

---

ACRONYMS	vi
NOMENCLATURE	vii
<b>1 INTRODUCTION</b>	<b>1</b>
1.1 Objectives . . . . .	8
1.2 Scope and structure of thesis . . . . .	10
<b>2 PRINCIPLES OF PLASMONIC FIBRE SENSING</b>	<b>12</b>
2.1 Biosensors – general introduction . . . . .	12
2.2 Transducer – plasmonic nanoparticle approach . . . . .	13
2.2.1 Localised surface plasmon resonance . . . . .	14
2.2.2 Noble metal nanoparticles in an electric field . . . . .	16
2.2.3 Mie theory . . . . .	18
2.2.4 Substrate effect . . . . .	21
2.2.5 Performance characteristics of LSPR transducers . . . . .	22
2.2.6 Influencing NP spectral properties . . . . .	25
2.3 Platform – microstructured optical fibre (MOF) . . . . .	27
2.3.1 Light propagation in optical fibres . . . . .	27
2.3.2 Introduction to microstructured fibres . . . . .	29
2.3.3 Suspended-core MOF for evanescent field sensing . . . . .	31
2.4 Biorecognition element – DNA detection . . . . .	32
2.4.1 Hybridisation based affinity detection . . . . .	33
2.4.2 DNA on gold surfaces – immobilisation and alignment . . . . .	34
2.4.3 Regeneration of sensor . . . . .	36
<b>3 STUDY OF SENSING PROPERTIES OF SMALL-CORE MICROSTRUCTURED FIBRES</b>	<b>37</b>
3.1 Study of geometry and composition effects for SC-fibre sensing . . . . .	38
3.2 Modal attenuation in plasmonic-photonic fibres . . . . .	41
3.3 Comparison to existing taper capabilities . . . . .	46
3.4 Additional approaches . . . . .	48
<b>4 IMPLEMENTATION OF A PLASMONIC SC-MOF</b>	<b>50</b>
4.1 MOF platform . . . . .	50
4.2 Fabrication and characterisation of nanoparticles . . . . .	53
4.2.1 Gold nanosphere synthesis . . . . .	53
4.2.2 Gold nanosphere characterisation – quality control . . . . .	54
4.3 Incorporation of gold nanospheres in-/on-fibre . . . . .	55
4.3.1 Aminosilane modification . . . . .	55
4.3.2 Layer-by-layer polyelectrolyte deposition . . . . .	59
4.4 Characterisation of nanoparticle layer depositions . . . . .	61
<b>5 OPTICAL INVESTIGATIONS OF LIGHT GUIDANCE IN PLASMONIC SC-MOF AND ECF</b>	<b>65</b>
5.1 Concept of LSPR characterisation using an “on-axis” measurement . . . . .	65
5.1.1 On-axis measurement setup and protocol . . . . .	65
5.1.2 Cutback measurement and analysis – SC-MOF . . . . .	67
5.1.3 Measurement and analysis – ECF . . . . .	70
5.2 Concept of LSPR characterisation using a “cross-axis” measurement setup	71
5.2.1 Cross-axis measurement setup and protocol . . . . .	71
5.2.2 Cross-axis sensitivity measurement . . . . .	73



5.3	Strategies for optofluidic measurement in SC-MOFs . . . . .	74
5.4	Strategies for optofluidic measurement in ECFs . . . . .	78
5.5	On-axis RI sensitivity measurements of plasmonic fibre systems . . . . .	80
<b>6</b>	<b>PATHOGEN DETECTION USING ENSEMBLE LSPR (ELSPR)</b>	<b>84</b>
6.1	Concept of “ensemble of nanoparticles” LSPR characterisation . . . . .	84
6.1.1	Setup configuration for eLSPR . . . . .	85
6.1.2	Chip design and integration with microfluidics . . . . .	85
6.2	LSPR planar biosensor preparation . . . . .	86
6.2.1	LSPR chip characterisation and bulk RI planar measurement . . . . .	87
6.3	DNA deposition and hybridisation detection on planar structure . . . . .	87
6.3.1	Biofunctionalisation of immobilised gold nanospheres . . . . .	89
6.3.2	Biodetection of target DNA samples and control . . . . .	89
6.3.3	Regeneration of sensor post-hybridisation . . . . .	90
6.4	DNA deposition and hybridisation detection on ECF structure . . . . .	90
<b>7</b>	<b>CONCLUSION AND FUTURE PROSPECTS</b>	<b>95</b>
	<b>BIBLIOGRAPHY</b>	<b>100</b>
<b>A</b>	<b>ACKNOWLEDGEMENTS</b>	<b>123</b>
<b>B</b>	<b>PUBLICATION LIST AND ATTACHMENTS</b>	<b>124</b>
	<b>EHRENWÖRTLICHE ERKLÄRUNG</b>	<b>125</b>



## INTRODUCTION

---

Photonic techniques offer a favourable approach to probing biological material systems for measurement and manipulation, due to their non-invasive, non-destructive, pervasive potential. When employed for disease detection and treatment, and pathology in general, photonic methods provide a means to study both molecular morphology and its physiological function.

The real-time detection of life-threatening disease is a major challenge in current biomedical advancement [1–3], as it requires both the identification of pathogens on the molecular level and the conversion of the corresponding information into macroscopic, measurable signals. The diverse approaches to tackling this detection issue in today's systems, for instance by utilising culture methods, are highly time-consuming [1, 4, 5]. Culturing involves enriching and growing a pathogenic organism in order to identify it. For slow growing organisms the delay to definitive diagnosis can stretch to weeks, while many organisms exist which cannot be cultured at all. Culturing organisms is also a resource intensive process, with other drawbacks including sensitivity problems (for instance with non-culturable pathogens), and the potential safety concerns accompanying growing certain pathogenic organisms.

Thus pathogen diagnosis based on nucleic acids (in particular DNA) has become particularly relevant [6–11]. In this approach the genetic materials of microorganisms are extracted, amplified, and identified. Such testing has significantly reduced turnaround times for routine diagnostics, in the case of gastrointestinal pathogens from days to hours [1], and enabled multiple pathogen identification within a single test [12, 13], many of which were previously difficult to diagnose. Diagnosis relies on the principle of complementary base pairing between strands of DNA/RNA molecules – a process referred to as hybridisation. This enables the design of specific probe sequences, targeting for instance antibiotic resistant strains and for bacterial sub-typing. Targeting nucleic acids however, means that the viability of the target pathogen is unknown – whether it is currently active or merely nucleic remnants from recent activity is not certain. In the case of detecting hibernating or unculturable cells [14–16], or determining antibiotic effectiveness [17, 18] this is a benefit.

Classically the subsequent diagnosis involves microscopic investigation of the pathogen using a range of staining methods or electron beam microscopy which is expensive and depends heavily on available, trained personnel. The general principle of optical detection relies on exploiting some intrinsic optical property of the test material. Detection is performed by investigating the interaction of an optical field with the sample. Properties like absorption, reflection, transmission, and scattering of the substance strongly affect the spectral distribution and transmission of the applied optical beam [19–21]. Optical biosensing can be broadly divided into two general types: label-free and label-based. In label-free sensing, the interaction of the analysed material with a transducer directly generates the detected signal [22, 23]. In contrast, label-based sensing involves the use

of a label and a fluorescent [24, 25], colorimetric [26, 27], or luminescent [28] method generates the optical signal.

The earliest molecular optical detection method was to interrogate small volumes [29], for instance in a cuvette. Detection was performed either by scanning the sample with a laser or by flowing a solution through the tight focused spot. A molecule transiting the laser spot's illumination volume could then be detected as a burst of fluorescence. In general analyte molecules do not fluoresce so a direct label-free measurement cannot be performed. Hence virtually all optical single molecule detection and analysis methods are indirect and detect a label associated with the molecule of interest [30, 31]. Fluorescence is the standard method for binding event detection in molecular biology, as a result of its intrinsic amplification, and a wide variety of fluorescence-conjugated biomolecules and highly sensitive markers are available for sensing. However, these markers are still limited in terms of photochemical instability, an environmentally sensitive quantum yield, and the high cost of the readers required [30, 32, 33]. In addition, the use of a label can affect the intrinsic properties of a species.

Label-free optical detection systems currently exist based on absorbance and refractive index, for instance in the form of fibre systems [34–36], cavities [37, 38], and planar substrates [39–41]. However absorbance based measurement is a far more challenging technique due to low absorption cross sections and path lengths. Similarly a high level of sensitivity would be required to detect the refractive index (RI) change induced on the molecular level. The critical issue posed is the low interaction of light with matter which needs to be enhanced for such sensing.

One promising diagnostic scheme enabling high field enhancement, sensitivity, cost efficiency, and short detection timescales, involves the attachment of specific molecular probes to plasmonically-active metallic nanoparticles (NPs) [11, 42–44]. The attachment process is referred to as functionalisation, changing the surface chemistry features of the NP. Plasmonic NPs exhibit a distinct optical spectrum response – termed the localised surface plasmon resonance (LSPR) – upon excitation at the resonance of the electron ensemble [45–48]. The spectral extinction signature of the NP consisting of absorption and scattering contributions, and the peak wavelength position  $\lambda_{\text{peak}}$ , depends on factors including: its size, shape, composition, and local RI environment [23, 39, 49–51]. Gold in particular represents a readily functionalisable, chemically-stable, biocompatible candidate with a strong plasmonic response [52, 53]. In this approach, the NPs interact directly with an incident light, requiring no dedicated technical equipment or arrangement, and enable device miniaturisation. Unlike fluorophores, plasmonic NPs do not suffer from blinking or photobleaching, enabling molecular binding observation over arbitrarily long time periods [54–56]. A particular advantage of LSPR is the strong electromagnetic (EM) field confinement to the NP – rendering it extremely sensitive to the NP's nanoscale RI surroundings. This forms the basis for NP-mediated molecular sensing [57–60].

If the DNA detection and plasmonic sensing approaches are coupled, and metallic NPs functionalised with single-strand *capture* DNA, the initial functionalisation and sub-

sequent binding events with complementary *target* DNA strands can be detected by the plasmonic NPs. The result is a macroscopic optical response without molecular labelling requirements. For practical reasons this sensing strategy is performed on a substrate since a colloidal detection would require a sophisticated tracking system [61, 62] and have the potential for particle aggregation and interaction [11]. Typically a low concentration of DNA-functionalised colloidal NP solution is used to immobilise [63, 64], anneal [65–68], or pattern nanostructures on a planar substrate for study [58, 69–71]. In fact, pathogen detection can be achieved in this manner solely through the scattering information of single NPs [42, 72, 73], yet this is more time consuming and involves cumbersome experimental equipment [74]. In most cases a dark-field microscope and spectrometer attachment are required, and single NP interrogation is conducted one-by-one (although this is improving with optical and imaging techniques [75–78]), it therefore becomes time intensive to gather sufficient data for statistical relevance in high-throughput.

In contrast, a NP-ensemble allows parallel signal readout from a high density of immobilised plasmon resonant nanostructures, possible using a spectrometer [71, 79]. The collective LSPR behaviour is obtained in a single optical extinction measurement (absorption and scattering induced light loss) using a collinear light path. The configuration is more convenient than the single NP LSPR counterpart but for the introduction of small analyte volumes it still requires integration into a chip setting.

Both of these LSPR systems rely on planar substrate or waveguide geometries, often entailing the need for sophisticated microscopic setups and cost intensive, complex excitation schemes for photonic mode launching. Many planar waveguides suffer high optical loss as a consequence of surface roughness or surface state absorption, and some require complex fabrication technologies. These systems also need additional integration for analyte based microfluidic detection. Although such plasmonic-DNA sensing systems have been realised [42, 79–81], their interaction length could be improved as could their excitation schemes to reduce cost, skill, and size requirements. The solution: waveguides that keep light confined over long lengths. The practical, low cost implementation of this is optical fibre.

Optical fibres are cylindrical dielectric waveguides able to transmit signal over considerable distances with attenuation loss as low as 0.2 dB/km [82, 83]. The total dimension of an optical fibre sensor is small; yet the active surface sensing area is greater than its planar counterpart due to the rod-like geometry and length. This solid rod-like structure further results in optical fibre sensors operating extrinsically, either coupling light directly to and from a sample or using an evanescent field for detection. Evanescent-field fibre sensing is a well-established technique that relies on light guidance within a higher refractive index core with an exponentially decaying evanescent tail penetrating the surrounding region. The penetration depth is limited (in the order of 10s to 100s of nm) such that only changes occurring in close proximity to the fibre interface can be sensed. The evanescent field component interacts through scattering and absorption in its overlap region and the presence of a test analyte is determined by studying the

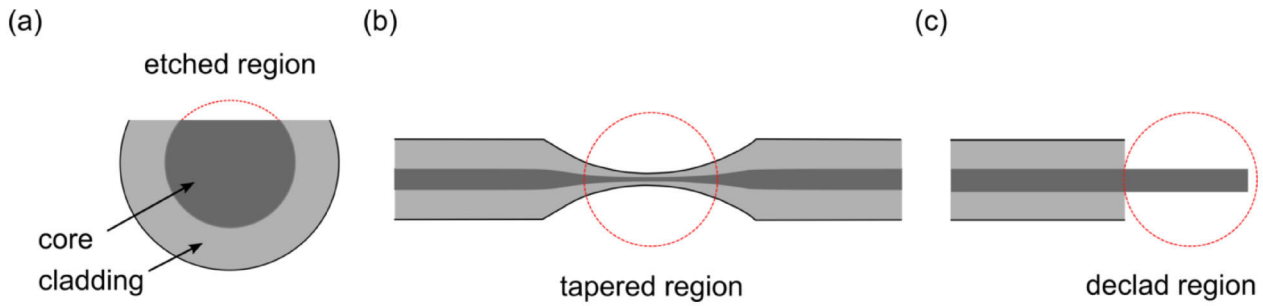


**Fig. 1.1:** Extrinsic fibre sensors modified for increased modal field interaction with an analyte. The sensing region is indicated with the red curve. Shown are (a) D-shape fibre, (b) taper, and (c) declad fibre.

induced attenuation in the transmitted, or reflected, fibre mode spectrum. The main challenge with this sensing approach is the low interaction between evanescent field and measurand. In order to increase the detected signal, the sensing region should be in close proximity to the guiding core. The fibre structure must therefore be modified in order to bring the test analyte closer to the evanescent field resulting in etched D-shape fibres [84], tapers [85,86], fibre end-face sensors [87] (Fig. 1.1). The resulting sensor systems, although sensitive, are mechanically compromised.

More recently, intrinsic fibre sensors have been explored that offer sensing within the fibre structure itself [88–91] (Fig. 1.2). This retains the chemical and mechanical advantages of the original fibre structure while allowing enhanced field overlap and containment of the test analyte along the entire length of the fibre sample. In the case of hollow-core fibres the field can overlap entirely with the analyte in the core region [34,92,93]. Optical fibre as a sensing platform is of particular interest from the medical and clinical points of view, as their intrinsic handling flexibility promotes *in vivo* application which cannot be attained using planar counterparts [61,88,94].

The approach of this thesis aims to bypass planar geometry restrictions and merge optical fibres with functionalised NPs – in theory enabling straightforward LSPR excitation, strong light-matter interaction over longer distances, fluidic exchange, and spectral multiplexing within one device. The LSPR excitation can be achieved simply by introducing plasmonic NPs into the evanescent fields of propagating modes of optical

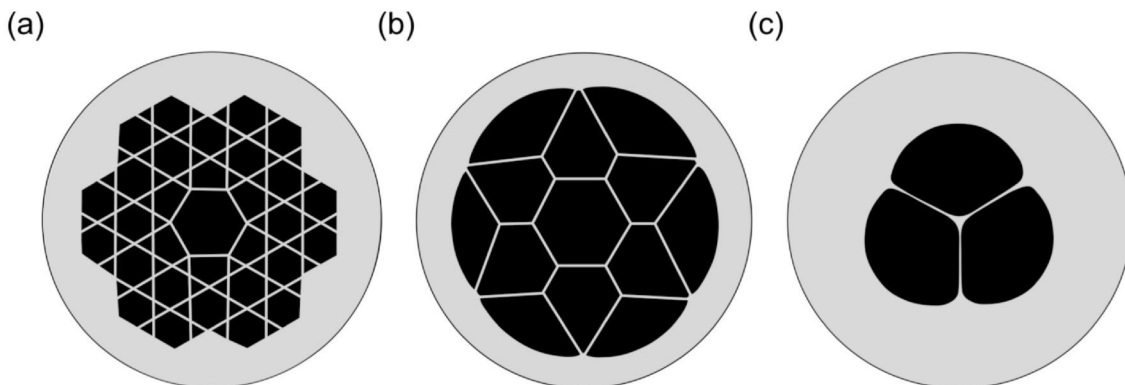


**Fig. 1.2:** Intrinsic fibre sensors enable modal field interaction with an analyte within the fibre without structural modification. Shown are (a) kagome fibre, (b) antiresonant hollow-core fibre, and (c) suspended-core microstructured fibre.

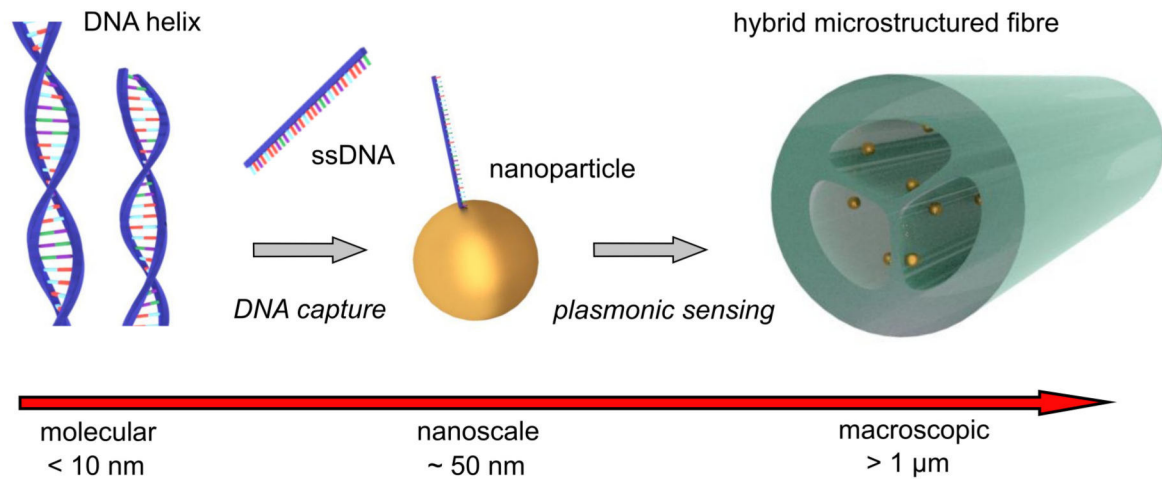


**Fig. 1.3:** Schematic combining the microscopic molecular level (DNA hybridisation), via LSPR mediated NP sensing, with the macroscopic world, using MOF platforms. ssDNA probes are attached to Au NPs immobilised within the microstructured channels of the fibre.

fibres [95,96]. Almost all plasmonic-fibre sensors demonstrated thus far consist of either multi- or single- mode tapers that have been coated with NPs [97–99] or continuous metallic nanofilms [85, 100]. Although these taper systems have exhibited RI sensing capacities, they remain extrinsic sensors with the NPs positioned on the outer surface of the fibre. This results in non-integrated, mechanically delicate devices requiring much higher analyte volumes than necessary for the sensing process. Pathogen detection by a plasmonic functionalised fibre approach has not been manifested as of yet, due to a want of innovative sensing strategies and adequately functionalised NPs. The sensors evidenced in literature use comparably simple fibre geometries [93, 101, 102], thereby limiting their application as refractive index sensors due to containment, low signal, handling, and reusability factors. This work aims to overcome such limits by implementing a more complex, intrinsic microstructured fibre design for plasmonic functionalisation, laying the foundation for the development of a plasmonic fibre sensor for future pathogen detection.

Microstructured optical fibres (MOFs) represent an important class of innovative fibre geometry, which may comprise of either a photonic crystal fibre (PCF) structure [89, 103, 104] incorporating longitudinally invariant microstructures, or a structure containing optically resonant elements at single or multiple locations along its length. The PCF structure that is implemented in this thesis [105, 106], can contain single air holes, or air hole arrays, of tailorable diameter (typically 30 nm to 100 nm) enabling a high degree of design flexibility of the optical properties [103, 107]. The aspect of utmost interest for this work is the integration of these microstructured regions as enclosed optofluidic channels in contact with a light guiding fibre core. Such geometry boosts the light-analyte interaction length by orders of magnitude. The objective then of this work is to combine two separate MOF geometries with label-free NP-based analyte molecular sensing, to develop a scheme towards future real-world pathogen detection.

The operational principle of the proposed NP-enhanced MOF sensors is based on the evanescent field interaction of their guided core modes with the LSPR of the core-immobilised NPs. The NP extinction behaviour is retrievable from the overall spectral distribution of the fibre's transmitted light. The NPs fixed on the core surface respond to a variation in the RI of the local medium, showing highest sensitivity at a distance of 5–10 nm from their surface as a consequence of short electromagnetic decay lengths [108]. This response is detected as a spectral shift of the LSPR, such that nanoscale environmental changes can be observed via analysis of the output signal's spectral distribution. Fig. 1.3. illustrates the envisioned concept in its entirety combining nucleic-acid detection, plasmonics, and MOFs. Implementing ssDNA to specifically bind with its complementary strand on the molecular level, and functionalising plasmonic Au NPs with this ssDNA nanoprobe, permits the field enhancement and sensitivity necessary to detect binding events. Immobilising such Au NPs homogeneously within the channels of a MOF allows their LSPR to be excited by the evanescent field from the small suspended core, and be detected as attenuation in the transmitted optical mode spectrum of the fibre.

The specific combination of MOFs and DNA-functionalised, immobilised metallic NPs is unique, effecting the evolution of a range of rapid, reusable, and inexpensive biosensors. The experiments outlined in this thesis are designed to overcome the limitations of low sample volumes, time consumption, sensitivity, and optical multiplexing by coupling plasmonic and optical fibre techniques in a monolithic bioanalytic sensor. The enclosed optofluidic channels of the fibre geometry reduce analyte volume requirements and exchange times, while the small, NP-functionalised, suspended-core provides an extended light-analyte interaction length. The plasmonic NPs provide enhanced field interaction and sensitivity at their surface enabling a variation of the nanoscale RI environment to be observed in real time in the output fibre spectrum. This work deals with developing these hybrid NP-immobilised fibre sensors; combining both plasmonic and fibre platform aspects for RI sensing. In the following section the current state of the art is briefly addressed for each concept part before expanding on the thesis aim in detail.

## **Current state-of-the-art**

### **State-of-the-art: DNA sensing via metallic nanoparticles**

A range of NP detection schemes have been presently realised for bioanalytical applications [55]. For instance, the first colorimetric DNA-assays have been established [109,110] by coupling plasmon resonances of two or more gold NPs during ssDNA hybridisation (when strands anneal together). Colorimetry is based on eliciting a visually detectable colour-change for detection. However, the method necessitated a complex conjugation (labelling) technique for the DNA-particle binding in solution.

Additionally, NP immobilisation for LSPR sensing has been conducted on planar surfaces [55,111,112] with a single NP sensor yielding superior signal to noise ratio than the



counterpart NP ensemble device [42]. Readout performance is primarily based on NP sensitivity, a key characteristic that is defined as the ratio of the spectral resonance shift,  $\Delta\lambda_{\text{peak}}$ , and the change in RI unit,  $\Delta n$ , in the NP's vicinity [113]. An example would be that of triangle-shape particles, which exhibit sufficient sensitivity to enable molecular diagnosis of lactose intolerance in clinical samples [80].

### **State-of-the-art: microstructured optical fibre sensing**

MOFs constitute a special category of optical fibre, possessing a degree of tailorability that far exceeds that of standard telecommunication fibres [114]. By incorporating longitudinal channel structures of supportable diameter into optical fibres, the corresponding optical properties of the propagating core modes can be uniquely engineered. Suspended-core MOFs have so far been demonstrated as sensing devices and for monitoring chemical reactions in-fibre [115–117]. Due to their internal containment of the analyte and high field overlap increasing signal strength for sensing, MOFs offer an exciting alternative to traditional extrinsic fibre sensors [103, 104, 114].

Alternatively, another form of MOF incorporates resonant elements in fibres at one or more locations along its length. Such in-fibre resonators considerably enhance the system's light-matter interaction and thus the RI sensitivity. Examples include Fibre Bragg Gratings (FBGs), [118, 119], and side drilled microslots penetrating the core structure [120]. The sensitivity offered by these devices is limited however by the quality of each individual resonator fabrication.

### **State-of-the-art: fibre-based surface plasmon resonance sensors**

Combining fibre sensing with NPs yields hybrid plasmonic-photonic fibre sensors offering enhanced interaction strength and area, high sensitivity, reusability, and ease-of-operation for mode excitation and handling. In addition, such hybrid fibre sensors could be applied in vivo for clinical application.

One existing fibre-based LSPR RI sensor, involves a large-core multimode fibre whose cladding is stripped at one end [98]. Gold nanorods are first established on the core walls, and the end facet is coated by metal mirror. In this approach LSPR is excited by the core mode's evanescent field and the device operated in reflection mode. LSPR spectral shift is observed if the RI in the end facet's surroundings is modified (in the vicinity of the nanorods). However this destructive technique leaves the core fully exposed for damage, which limits the NP immobilisation area.

A further highly sensitive fibre-based plasmonic sensing device is a fibre taper coated by gold NPs [97, 99]. LSPR is again excited via the core mode's evanescent field. This fibre device demonstrates significant change in resonance wavelength and transmission intensity when the NPs' RI surrounding changes. The extremely small taper waist diameters render this device mechanically delicate-to-handle and therefore unfeasible for real-world application.

Alternatively, a combination of intrinsic fibre sensors and plasmonics would bypass many of the challenges faced by current sensing systems [36]. Various plasmonic MOF systems have been suggested theoretically [121], yet very few have been realised experimentally [122]. Those that have include an exposed-core MOF coated with full metal layers [122], used to measure scattering at points on the layer, or non-immobilised plasmonic components [123]. The proposed cases include a tri-hole MOF with metallised film around the microstructures [121, 124], a polished D-shape hollow-core MOF [125], and a number of metal-filled PCF sensors [102]. Despite these examples, plasmonic MOF sensing remains predominantly theoretical due to the complexity posed by plasmonic deposition within the interior of the fibre microstructures. Recently, first attempts to incorporate small silver NPs into MOFs have been conducted [126–128], wherein the LSPRs were probed in the direction perpendicular to the fibre axis – not exploiting the advantages offered by fibre geometry.

The system developed in this thesis consists of a MOF with small suspended-core enabling intrinsic fibre sensing and long interaction lengths with analytes. Two particular types of MOF geometry constitute the focus of this study, namely tri-channel SC-MOFs and exposed core ECFs as introduced in the next section. Plasmonic Au NPs are chemically immobilised within the microstructures, enabling an enhanced field for RI index sensing at the NP surface and allowing future functionalisation and DNA binding event detection. This system provides the required NP fixation for reusability, homogeneous NP deposition, and mechanical stability compared to extrinsic sensors. Unlike their planar counterparts, such an optical fibre platform can potentially be applied *in vivo* and is therefore highly attractive from a medical viewpoint. The approach outlined in this thesis has not been encountered in literature, addresses fundamental aspects of nano-scale light-matter interaction, and targets a concrete medical diagnostic need: rapid, low volume, DNA-based pathogen detection, for instance for screening against pulmonary infectors such as *Aspergillus spp. (species pluralis)* or *Legionella spp.* bacteria.

### 1.1 Objectives

The overall goal of this thesis study is to establish a fundamentally new and label-free biosensor platform by implementing functionalised plasmonic nanoprobe within MOFs (Fig. 1.4). The principle hypothesis rests on probing the LSPRs of functionalised NPs by the propagating fundamental modes of MOFs, leading ultimately to hybrid plasmonic-photonic fibres for biosensing.

This concept stimulates the transduction of a molecular response, via plasmonic NPs, into macroscopic signals detectable by the MOF structures – culminating in an optical biosensing platform. Fig. 1.4 outlines the thesis aim once more, involving the combination of the two different MOFs exciting the LSPRs of Au NPs via the evanescent field of their fundamental propagating modes. The NP extinction behaviour is visible in the attenuated output spectrum of the MOFs and is dependent on the NPs used. This thesis implements Au nanospheres – which are chemically stable, biocompatible, and

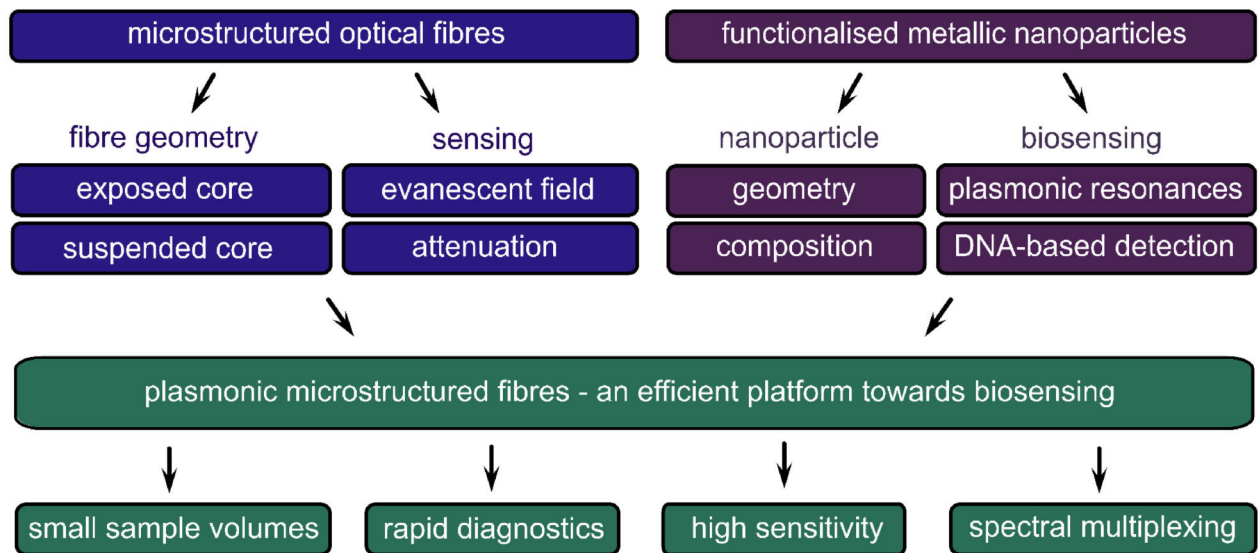


**Fig. 1.4:** Chart of the overall concept of this thesis illustrating the various scientific considerations involved.

could be readily functionalised in future with ssDNA for pathogen detection. The final plasmonic MOF sensor offers a range of advantages over planar plasmonic devices and conventional extrinsic fibre sensors. Distinct from their standard telecommunication counterparts, MOFs enable huge adjustment potential of light-matter interaction and present an optofluidic environment that is ideally suited for biochemical application. This scheme thus constitutes a multiscale approach, fundamentally linking the microscopic level through LSPR-mediated molecular sensing with the macroscopic world using MOFs – leading to the implementation and study of a novel and unexplored sensor platform.

In fact, this work represents part of a two-stage approach necessary for the development of a remarkably sensitive plasmonic fibre biosensor. The focus of the first stage, dealt with in this thesis, involves the enhancement of optical detection by implementing and immobilising metallic NPs within MOFs. The NP layers should be fixed, homogeneous, of adjustable density, and offer sufficient sensitivity. The second stage, not dealt with in this study, would involve the optimisation of the detection element sensitivity by means of other functional nucleic acid biomolecules, for instance DNAzyme for enhanced thermal stability and signal [129].

The work presented here targets the following objectives:

1. A fundamental investigation of light-matter interaction of immobilised metallic NPs i.e. LSPRs with the propagating fundamental modes of MOFs.
2. Sensing application with functionalised metallic NPs i.e. detecting RI induced LSPR shifts.
3. Developing the sensor concept towards a concrete real-world example of pathogen detection i.e. immobilising NPs capable of functionalisation with DNA-capture probes, and detecting binding events of DNA-sequences.

As mentioned, two types of MOF geometry comprise the focus of this study, namely a tri-channel SC-MOF and exposed core, ECF (see Fig. 1.5). Throughout this thesis the tri-channel fibre is referred to as SC-MOF, with the exposed-core fibre being referred to directly as ECF, both are technically MOFs however.

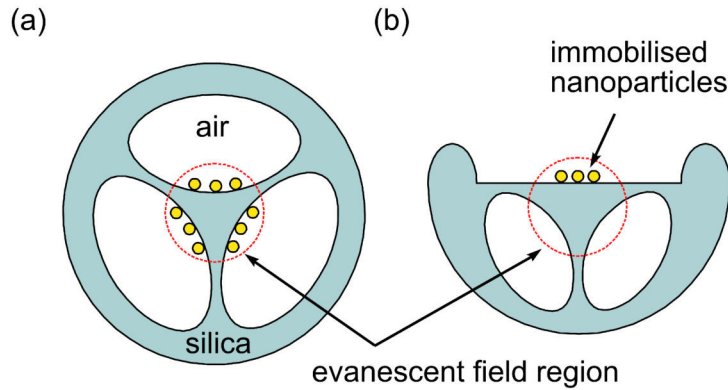


**Fig. 1.5:** The implemented MOF geometries (a) suspended-core MOF (b) exposed-core fibre. The NP-on-core sensing region is indicated by the red circle.

These MOF based sensors (Fig. 1.5a,b) operate by evanescently probing the LSPRs of the immobilised NPs via the fundamental core guided mode, thereby accessing extended interaction lengths of fibre mode and nanoparticle ensemble. In this thesis, both geometries of microstructured fibre-based sensors are studied in great detail with respect to NP based optical sensing with the view for molecular biosensing and potential implementation into a real-world device. A range of NP deposition techniques are implemented in order to experimentally optimise a uniform immobilisation within the microstructures. Specifically, the following scientific and technological questions are addressed:

- How can the interaction of NP and MOF modes be described analytically?
- How can the properties of MOFs enhance the functionality and performance of photonic-plasmonic biosensors?
- Which NPs are optimal, in terms of shape and composition, for providing RI sensitivity and functionalisation towards initial biosensing using MOFs?
- Can flexible fibre RI sensors be implemented with the potential for application in a clinical environment?
- Is the detection of a targeted DNA-sample species e.g., of *Legionella spp.* (pneumonia causing) or *Aspergillus spp.* (pulmonary infecting) pathogen feasible with such a sensor?

## 1.2 Scope and structure of thesis

This thesis begins with a theory and background section (sec.) in Chapter (Ch.) 2, outlining the principles involved in an optical fibre biosensor. The device is deconstructed

into a transducing, plasmonic nanoparticle background, including modelling and morphology considerations; a platform, microstructured optical fibre background, detailing the principles of light guidance within such a waveguide; and finally the detection, biosensing element aspect, which plays a smaller exploratory role within this work.

Following this, Chapter 3 presents a numerical study of the guidance and sensing properties of the chosen fibre geometry. The detection sensitivity possible with different MOF core sizes and materials is calculated and a comparison made to simulated state of the art taper systems.

With the optimal choice of geometry acquired, in Chapter 4, procedures for gold nanoparticle deposition and density tailoring of the NP layers are demonstrated. The resulting deposition quality is investigated with respect to layer homogeneity and density along the fibre and around the channel curvature. The immobilisation techniques are fibre dependent and this chapter offers an experimental study of a number of deposition strategies and their effectiveness in combination with the chosen MOF structures.

The optical characteristics of the resulting deposited plasmonic MOFs are investigated experimentally in Chapter 5. The resulting modal attenuation from various ensemble densities is quantified and compared to calculation. Strategies to optofluidically measure both fibre types are investigated. These measurements aim to in-couple light while changing the RI of the microchannels simultaneously. Finally the sensitivity of the ECF and SC-MOF NP-functionalised RI sensors is individually verified and compared to theory.

An additional final results section, Chapter 6, presents an approach for DNA functionalisation and detection on Au NPs attached to planar surfaces, and outlines preliminary strategies to implement this on an ECF platform.

The concluding Chapter 7, summarises and discusses the thesis work as a whole. An outlook is provided, highlighting a number of additional deposition and application techniques that could in future prove extremely interesting for MOF application and the final implementation of a real world MOF plasmonic biosensor. The primary findings of this thesis have been partly published in two journal articles [105, 106].

This chapter lays out the fundamentals required to understand the proposed optical biosensor. Biosensors are introduced in general and the main components involved for the concept of this thesis are discussed in individual sections. These include the theory behind plasmonic nanoparticles and optical fibre platforms, as well as further DNA considerations. The section on plasmonic nanoparticles discusses how NPs can be used as sensing elements, delves into the theoretical aspects necessary to understand optical phenomena such as LSPR, and further compares the effects of using a substrate or changing the intrinsic morphology of the NPs on their optical behaviour. The section on optical fibres offers an overview of light guidance in conventional optical fibres and microstructured fibres, and how the latter can be used for sensing. Finally, the section on DNA as a detection element provides insight on the detection mechanism and how it could be implemented in future into a plasmonic MOF biosensing system.

### 2.1 Biosensors – general introduction

In order to diagnose the presence of a pathogen or contaminant, a sensor system must be able to first identify the pathogen at the molecular level and subsequently convert this identification to a macroscopic measurable signal. As such, a biosensor is essentially comprised of a detection (biorecognition) element designed for specific interaction with an analyte (incorporating nucleic acids for instance), and transducer (sensing element) to convert the detected event signal to a measurable macroscopic property, as in Fig. 2.1. The biorecognition element is typically implemented in the form of a layer enabling direct spatial contact with the transducer and maximising the proximity and stability of the active recognition area.

The biorecognition element has the primary function of providing selectivity for the target, or analyte of interest, but should also offer properties such as stability, functionality and reversibility to ensure high performance. Various classes of molecules can be

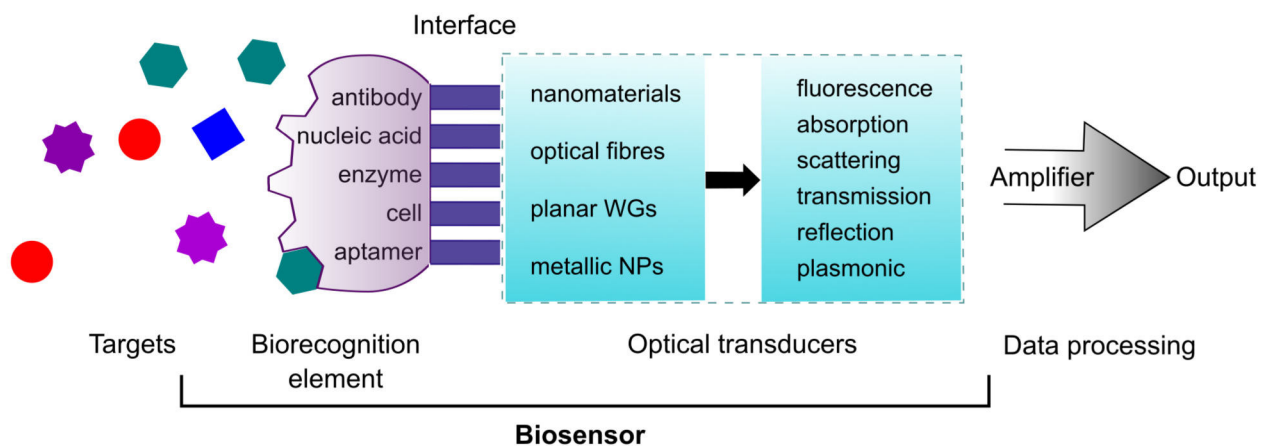


**Fig. 2.1:** Schematic of a biosensor comprised of biorecognition and transduction elements. Detection element examples as well as optical means of transduction are listed, for instance, metallic NPs offering plasmonic response.

incorporated as a biorecognition layer to achieve this, such as enzymes, antibodies, receptors, or nucleic acids.

The transducer should transform binding events at the biorecognition layer into a measurable signal. This transduction can occur by a variety of mechanisms e.g., optical, electrochemical, thermal, or mechanical depending on the signal generated between analyte and sensing element. The output transduced signal should be correlated to the number of binding events with the target analyte to enable quantification. Additional information involving kinetics and binding affinity can be retrieved.

The focus of this thesis will be confined to optical transduction and surface plasmon (SP) based sensors. The core functioning principle involves the detection of refractive index (RI) changes in the vicinity of the surface of metal nanostructures, induced by chemical reaction or recognition events. Plasmonic biosensors present a class of optical label-free sensors possessing metal or metal-dielectric nanostructures supporting surface plasmons as the transducing element. Proper light illumination of the plasmonic sensing component excites SPs on those structures and further results in an electromagnetic (EM) field highly concentrated at each structure's surface [113]. When a test analyte is introduced to the biosensor, binding or capture of the analyte by the biorecognition element (immobilised on the transducer) results in RI variation in the local proximity of the transducer. The associated SP's characteristics are extremely sensitive to RI changes in its immediate surroundings, and so the analyte-binding induced RI change may be determined by monitoring changes in the SP optical spectrum such as a change in resonant wavelength position, intensity, or phase.

## 2.2 Transducer – plasmonic nanoparticle approach

One transduction strategy yielding high sensitivity involves functionalising specific molecular probes to metal nanoparticles (NPs) that support plasmonic resonance. Plasmon resonance is the optical phenomenon that arises in a metal from the collective oscillation of its conduction electrons when disturbed from their equilibrium position [46, 47, 130, 131]. This disturbance may be induced by an electromagnetic (EM) wave, wherein the alternating electric field drives the metal's free electrons to oscillate coherently at a resonant frequency. An EM wave incident on a metal interface possesses only a limited penetration depth, and thus only surface-electron induced plasmons are of significance. These are termed surface plasmons (SPs).

Surface Plasmon Resonance (SPR) can occur in two distinct forms: that of propagating surface plasmon polaritons (SPPs) and localised SPRs (LSPRs). SPPs consist of bound EM waves that propagate along a dielectric-metal interface with an exponential field decay normal to the interface [46]. This phenomena cannot be excited directly by free-space radiation but rather requires phase matching of the momentum of the incident light and SPP – such as through periodicity in a nanostructure. Should the collective free-electron oscillation be further confined to some finite volume, as with a metal NP, the associated non-propagating plasmon resonance is referred to as a localised surface

plasmon resonance (LSPR). LSPR can be excited directly by propagating light incident on a NP and is the focus of this work. The physical background and implementation of this phenomenon are further detailed in this section.

If excited at the electron ensemble resonance, noble metal NPs produce a specific LSPR optical response that is precisely tailorable by synthesis strategy, entailing tuning the NP's material properties or morphology, or even by varying the surrounding dielectric environment. As discussed in this chapter, an induced change in spectral resonance peak position ( $\Delta\lambda_{\text{peak}}$ ) can be used to detect binding events. Furthermore, whether in the form of complex nanostructures, monolayers, single nanoparticles, or solutions, plasmonic NPs can function as transducer structures. In fact, several distinct approaches can be adopted to exploit metallic NPs and their LSPR sensing characteristics in optical transducing [132]:

1. Detecting  $\Delta\lambda_{\text{peak}}$  induced by bulk refractive index variation,  $\Delta n_{\text{bulk}}$ , of the surrounding media.
2. Detecting  $\Delta\lambda_{\text{peak}}$  induced by local analyte binding at the NP surface,  $\Delta n_{\text{surface}}$ .
3. Incorporating NPs as labels and monitoring absorption or scattering variations,  $\Delta C_{\text{abs}}$  or  $\Delta C_{\text{sca}}$ .
4. Detecting  $\Delta\lambda_{\text{peak}}$  resulting from induced metallic NP aggregation via analyte binding.
5. Monitoring linked metallic NPs for analyte induced distance changes,  $\Delta d$  (plasmonic rulers).

Of these, the first three instances are relevant and discussed within this study. As will become evident, the advantages of LSPR in this work include reduced coupling considerations, relaxed geometric and polarisation requirements, and lower production costs. Furthermore an extremely large EM field enhancement in the NP's vicinity results in enhanced sensitivity to nanoscale RI changes in close proximity to the NP – critical for molecular sensing.

### 2.2.1 Localised surface plasmon resonance

In this work, a plasmonic-fibre optical sensing system is realised based on the excitation of LSPR in metallic gold nanospheres, immobilised within the channels of microstructured optical fibre. Nanospheres present the most stable NP geometry with the lowest surface-to-volume ratio. Unlike more exotic geometries they can retain their shape over time without additional capping agents. The uniform spherical geometry also enables a straightforward homogeneous deposition orientation. The NPs applied in this investigation are mainly spherical gold particles of diameter around  $d_{\text{NP}} = 30\text{--}45$  nm. When one such sub-wavelength ( $d_{\text{NP}} \ll \lambda$ ) conductive nanosphere is positioned in an oscillating EM field, the particle's curved surface exhibits an effective restoring force on the driven



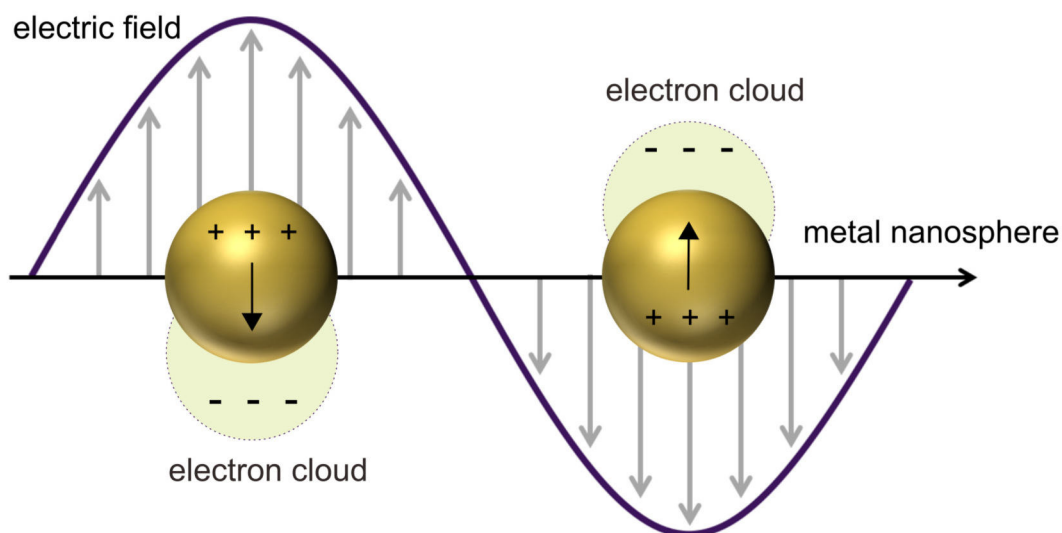


**Fig. 2.2:** Schematic of the localised, non-propagating excitations of an Au NP coupled to an EM field.

conduction electrons such that resonance occurs (causing internal and external amplification, in the nanoparticle near-field zone, Fig. 2.2). This is referred to as the localised surface plasmon resonance.

Furthermore, apart from strong light scattering and absorbance, greatly enhanced local EM fields can be achieved by plasmonic nanostructures. Very intense local electric fields can be induced within just a few nanometres of the nanostructure's surface providing increased sensitivity to RI changes in this region [46, 55]. In addition, the curved particle surface enables plasmon resonance excitation by direct light illumination. This avoids the necessity for additional phase-matching techniques and polarisation considerations, which must be accounted for when exciting a propagating SP [46]. In this manner both geometric and polarisation requirements are less stringent for a NP-functionalised SCF.

The metallic nanostructure's plasmonic properties can be understood by solving Maxwell's equations for the light-matter interaction over the nanostructure's volume. For the case of a homogeneous gold nanosphere and an incident plane wave of light a quasi-static approximation or Mie theory approach is applied.

When the nanoparticles are much smaller than the wavelength of light, the distribution of surface charge can be calculated simply using the quasi-static approximation [46, 133, 134]. In this description, the phase of the harmonic oscillating EM field is essentially constant over the volume of the NP, so that the simplified case of a NP in an electrostatic field can be assumed and the spatial field distribution calculated. Once the field distributions are available, the harmonic time dependence can be included. This yields the lowest order approximation for the full scattering problem and offers a reasonable description of the optical properties of many NPs with diameters below 100 nm.

NPs of larger diameters (exceeding 30 nm) can experience significant phase changes of the applied field over the NP volume and so the quasi-static approximation is no longer applicable, instead a rigorous electrodynamic approach, Mie theory [135], is required. Mie theory offers an effective analytical solution for the space inside and outside the

nanosphere and can be applied to determine its scattering and absorption cross sections. The results of the quasi-static approach can be retrieved by retaining only the first term of a power series expansion of the absorption and scattering coefficients. However, by implementing Mie theory it is possible to deliver exact solutions [134] in only a number of specific cases: those of a solid sphere, a spheroid, concentric spherical shells, and an infinite cylinder.

For determining the plasmonic properties of nanoparticles of arbitrary shape or lower symmetry [134], other numerical methods must be implemented, for instance: discrete dipole approximation (DDA) [136], finite time domain (FDTD) method, or finite element method (FEM) [137]. For qualitatively analysing the scattering properties of our spherical gold nanoparticles however, a quasi-static or Mie approach is sufficient.

### 2.2.2 Noble metal nanoparticles in an electric field

A common starting nanostructure implemented in plasmonic biosensing comprises of an LSP-supporting metallic nanoparticle sitting on a dielectric surface. The LSP extinction wavelength is dependent on the NP's size, shape, and composition, and for most noble metals it lays within the visible or near infrared (NIR) spectral region. Spherical metal NPs possess LSP at shorter wavelengths, whereas core-shell NPs or nanorings express resonance at longer wavelengths along with higher aspect ratio and sharper nanostructures such as nanorods or nanostars [53].

In this study, the nanostructures of interest are spherical gold particles of 34–45 nm diameter, expressing dipolar LSPR mode [138] in water around the optical frequency of 528–532 nm [105, 106]. As mentioned when ( $d \ll \lambda$ ) for the NP, the system can be treated as an electrostatic problem since with the optical frequencies used, the incident field wavelength is considerably larger than the nanoparticle dimensions. Thus the EM field's phase is considered constant over the particle volume.

In the quasi-static limit, the electric field can be expressed as a potential,  $\mathcal{E} = -\nabla\varphi$ , which must satisfy the Laplace equation,  $\nabla^2\varphi = 0$ , and material boundary conditions. Consequently, the static field polarisation induced in the metallic sphere and spatial field distributions can be determined [46, 134]. The potentials inside,  $\varphi_{\text{in}}$ , and outside,  $\varphi_{\text{out}}$ , the sphere can be found as [139]

$$\varphi_{\text{in}} = -\frac{3\varepsilon_{\text{m}}}{\varepsilon_{\text{NP}} + 2\varepsilon_{\text{m}}}\mathcal{E}_0r_{\text{mod}}\cos\theta, \quad (1)$$

$$\varphi_{\text{out}} = -\mathcal{E}_0r_{\text{mod}}\cos\theta + \frac{\varepsilon_{\text{NP}} - \varepsilon_{\text{m}}}{\varepsilon_{\text{NP}} + 2\varepsilon_{\text{m}}}\mathcal{E}_0r_{\text{NP}}^3\frac{\cos\theta}{r_{\text{mod}}^2}, \quad (2)$$

where  $\mathcal{E}_0$  denotes the field amplitude;  $\varepsilon_{\text{NP}}$  and  $\varepsilon_{\text{m}}$  (both functions of excitation frequency  $\omega$ ) the dielectric permittivities of NP and surrounding medium respectively;  $r_{\text{mod}}$  the modulus of the position vector;  $\theta$  the angle between the position vector and the z-axis; and  $r_{\text{NP}}$  the NP radius. Physically  $\varphi_{\text{out}}$  describes the superposition of a dipole located

at the centre of the NP and the applied field. From this, a key equation can be realised for the complex polarisability,  $\alpha$ , of a sub-wavelength diameter nanosphere in the electrostatic approximation:

$$\alpha = 4\pi r_{\text{NP}}^3 \frac{\epsilon_{\text{NP}} - \epsilon_{\text{m}}}{\epsilon_{\text{NP}} + 2\epsilon_{\text{m}}}. \quad (3)$$

Once the denominator  $\epsilon_{\text{NP}} + 2\epsilon_{\text{m}}$  is at a minimum, the polarisability undergoes resonant enhancement, which is expressed (for small or slowly varying  $\Im[\epsilon]$ ) as the Fröhlich condition:

$$\Re[\epsilon_{\text{NP}}] = -2\epsilon_{\text{m}}. \quad (4)$$

Therefore, to achieve resonance, the real part of the NP's permittivity should be negative, which is the case for metals at optical frequencies, and double that of the surrounding permittivity. The corresponding mode (in an oscillating field) is the dipole SP of the NP. The resonance frequency dependence on dielectric surroundings (crucial for RI sensing) can be clearly seen – the resonance red-shifts with increasing values of  $\epsilon_{\text{m}}$ . This makes metal NPs ideal candidates for optical sensing of RI variation. For the case of a metal nanosphere in air, and applying the Drude model for dielectric function [46, 140], the Fröhlich condition is met at

$$\omega_0 = \frac{\omega_{\text{p}}}{\sqrt{3}}, \quad (5)$$

where  $\omega_{\text{p}}$  is the metal's plasma frequency. The electric field distribution inside and outside the nanosphere can be written as

$$\mathcal{E}_{\text{in}} = \frac{3\epsilon_{\text{m}}}{\epsilon_{\text{NP}} + 2\epsilon_{\text{m}}} \mathcal{E}_0, \quad (6)$$

$$\mathcal{E}_{\text{out}} = \mathcal{E}_0 + \frac{3\mathbf{n}(\mathbf{n}\cdot\mathbf{p}) - \mathbf{p}}{4\pi\epsilon_0\epsilon_{\text{m}}r^3}, \quad (7)$$

with  $\mathbf{p} = \epsilon_0\epsilon_{\text{m}}\alpha\mathcal{E}_0$  being the dipole moment, and  $\mathbf{n}$  the unit vector normal to the surface. Hence, resonance in the complex polarisability indicates resonant enhancement of internal and dipole fields [45, 141], as anticipated, providing the basis of application in many optical devices. A further consequence of the resonantly enhanced polarisability is the associated enhancement in scattering and absorption efficiencies. A NP sitting in the path of a beam of light reduces the beam's power by absorption and scattering, together constituting the total extinction power. These values are expressed in terms of

cross sections, which for a particle of spherical shape and volume  $V$  are given in terms of  $\alpha$  by [142, 143]

$$C_{\text{sca}} = \frac{k^4}{6\pi} |\alpha|^2, \quad (8)$$

$$C_{\text{abs}} = k\Im[\alpha]. \quad (9)$$

$C_{\text{sca}}$  and  $C_{\text{abs}}$  stand for the scattering and absorption cross sections respectively. The extinction cross section for this specific case is given by

$$C_{\text{ext}} = \frac{9\omega}{c} V \epsilon_m^{\frac{3}{2}} \frac{\epsilon''_{\text{NP}}}{(\epsilon'_{\text{NP}} + 2\epsilon_m)^2 + (\epsilon''_{\text{NP}})^2}. \quad (10)$$

The width and strength of resonance is determined by the imaginary part of the metal's permittivity, which should be close to zero in order to support a strong resonance; otherwise a weaker or lossy plasmon is observed. A quality factor,  $Q_{\text{LSPR}}$ , which has a strong dependence on NP geometry, can be used to describe a plasmon's strength [52, 144]. In the spherical case,  $Q_{\text{LSPR}}$  is evaluated from

$$Q_{\text{LSPR}} = \frac{-\epsilon'_{\text{NP}}}{\epsilon''_{\text{NP}}}. \quad (11)$$

A larger  $Q_{\text{LSPR}}$  indicates stronger resonance; smaller  $Q_{\text{LSPR}}$  indicates a lossier plasmon with a smaller extinction cross section. Typically a  $Q_{\text{LSPR}}$  value higher than 10 is applicable for LSPR-based devices. In a wavelength range 400–1200 nm, silver yields the highest  $Q_{\text{LSPR}}$ , followed by gold (at 650 nm,  $|\frac{-\epsilon'}{\epsilon''}| \approx 42.21$  and 11.56 respectively). Due to its superior chemical stability, biocompatibility, and longer wavelength resonance gold was selected as the material of interest for our application.

### 2.2.3 Mie theory

The previously discussed method, of applying a quasi-static approach and the NP acting as an electric dipole, is valid only for vanishingly small particles. Practically, however, it actually allows a reasonable qualitative description for spherical or ellipsoidal particles smaller than 100 nm. In practice, for NP sizes of diameter,  $d > 30$  nm and those in the order of the wavelength of the incident light, the quasi-static approximation is less reliable due to the NP experiencing phase changes of the applied field over its volume [134]. In general, when the NPs exceed this size a broadening of the dipolar resonance spectrum and redshift occur [46]. In the case of these larger NPs, a more rigorous electro-dynamical approach is necessary, as set forth by Gustav Mie [135, 143, 145].

Mie theory is based on expanding the internal and external fields into vector spherical harmonics and determining their expansion coefficients using boundary conditions. The results of the electrostatic approach can be recovered by power series expansion of the scattering and absorption coefficients taking only the lowest order terms into account.

The resulting total scattering, absorption and extinction cross sections can be computed more thoroughly from these coefficients as follows:

$$C_{\text{ext}} = \frac{\lambda^2}{2\pi} \sum_{n=1}^{\infty} (2n+1) \Re[a_n + b_n], \quad (12)$$

$$C_{\text{sca}} = \frac{\lambda^2}{2\pi} \sum_{n=1}^{\infty} (2n+1) (|a_n|^2 + |b_n|^2), \quad (13)$$

$$C_{\text{abs}} = C_{\text{ext}} - C_{\text{sca}}, \quad (14)$$

where  $a_n$  and  $b_n$  indicate the expansion coefficients of the scattered wave and are composed of Riccati-Bessel functions, and  $n$  represents integers indicating dipole, quadrupole and higher multipoles. These coefficients, whose form is the primary result of Mie theory, are given as

$$a_n = \frac{m\Psi_n(mx)\Psi'_n(x) - \Psi_n(x)\Psi'_n(mx)}{m\Psi_n(mx)\xi'_n(x) - \xi_n(x)\Psi'_n(mx)}, \quad (15)$$

$$b_n = \frac{\Psi_n(mx)\Psi'_n(x) - m\Psi_n(x)\Psi'_n(mx)}{\Psi_n(mx)\xi'_n(x) - m\xi_n(x)\Psi'_n(mx)}. \quad (16)$$

In the equations:  $\Psi_n(\rho) = \rho j_n(\rho)$  and  $\xi_n(\rho) = \rho h_n^{(1)}(\rho)$ , with  $j_n(\rho)$  and  $h_n^{(1)}(\rho)$  being spherical Bessel functions of the first kind;  $m$  denotes the relative refractive index  $m = \frac{n_{\text{NP}}}{n_{\text{medium}}}$ ;  $x$  is the size factor  $x = kr_{\text{NP}}$  with  $k$  being the wavenumber and  $r_{\text{NP}}$  the NP radius; prime indicates the first derivative with respect to the argument. Both expansion coefficients contain contributions from the real refractive index of the surrounding medium indicating a change of surrounding RI directly influences the NP's extinction. For this reason, NPs can be implemented as transducers. A number of Mie calculators and codes are available, to calculate sample response from Mie theory. In this work Mie Plot [146] is primarily used to calculate NP extinction values. One should keep in mind that the solutions considered from Mie theory are for single, isolated NPs, and in the event of interacting NPs this interaction should be taken into account – generally resulting experimentally in an induced shift and resonance splitting [138]. Once the Mie coefficients have been determined, the EM fields inside and outside of the nanosphere or the extinction, scattering, and absorption cross sections can be calculated. The varying cross section contributions with increasing gold sphere diameters of 40, 80, and 120 nm in water are calculated in this manner and presented in Fig. 2.3.

Indeed one of the most accessible strategies to engineer the plasmonic properties of a nanostructure is to manipulate its dimensions. The absorption and scattering intensities, resonance positions, and number of modes, are all affected by particle size. The calculation results presented in Fig. 2.3. clearly indicate the influence of NP size on relative magnitude of scattering and absorption cross sections and their tunability potential.

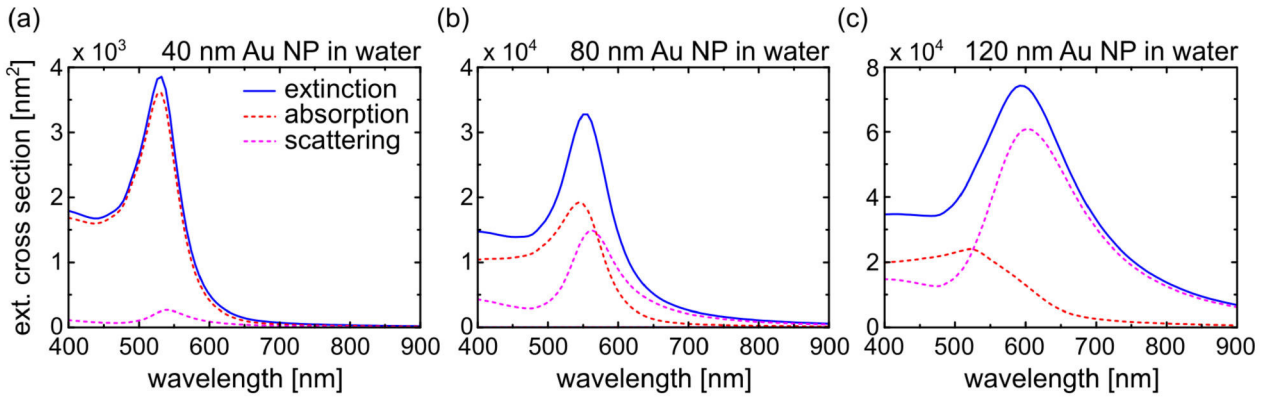


**Fig. 2.3:** Calculated extinction cross section for a gold sphere of diameter (a) 40 nm, (b) 80 nm, and (c) 120 nm. Also shown are the varying contributions from absorption and scattering with increasing sphere diameter. Values of  $\epsilon_\omega$  are taken from [147].

The absorption cross section mainly dominates at smaller nanoparticle sizes. An increasing sphere diameter shows a strongly increasing scattering contribution (scaling with  $C_{\text{sca}} \propto r^6$  [143]) compared to that of absorption ( $C_{\text{abs}} \propto r^3$ ). Also observed in Fig. 2.3a-c is the dipole resonance red-shift and broadening with increasing NP diameter, due to increasing charge separation on the sphere. Increasing only the size of the nanosphere incrementally, results in a redshift and broadening of the LSPR peak position, as well as a steady increase in the extinction cross section. In smaller diameter NPs primarily only dipole excitation exists, however in larger particles dipole and multipole excitation is possible [131,134]. Multiple resonance behaviour is also characteristic of non-spherical NPs with transverse and longitudinal plasmon mode excitation occurring. These cross sections also allow further understanding of the influence of local surroundings and composition material on the resonance of a solid nanosphere. As explained in Sec. 2.2.2 and Eq. 4, varying the RI of a metallic nanosphere's surroundings induces a shift in resonance peak position. As shown in Fig. 2.4a, changing the NP's surroundings from an air to water environment generates a red shift of the LSPR peak.

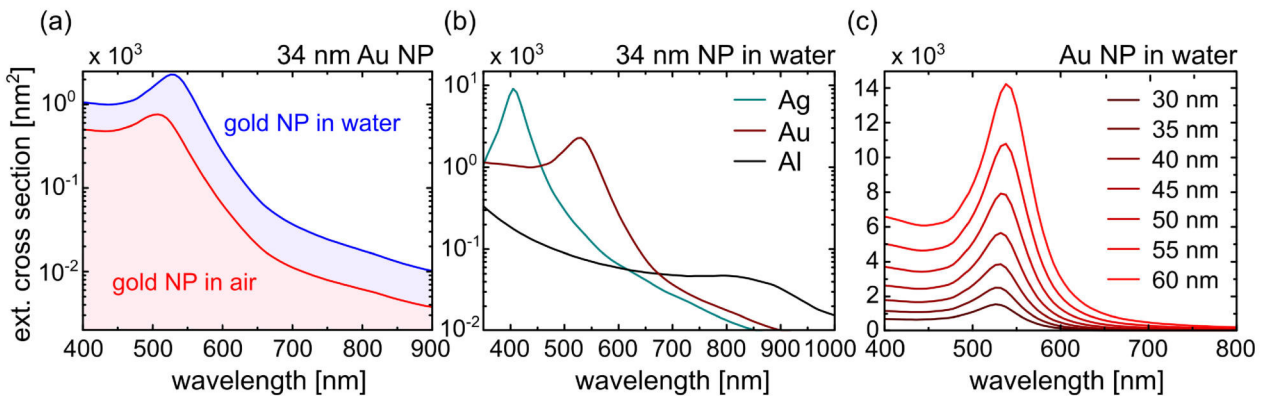


**Fig. 2.4:** Calculated extinction cross section for (a) a gold sphere of diameter 34 nm in an air and in a water environment. (b) 34 nm diameter spheres made of Ag, Au, and Al (values of  $\epsilon_\omega$  from [147]), in water. (c) Au nanospheres in water with diameters 30–60 nm.

Further varying the material of the sphere itself affects the resonance position and strength. Noble metal NPs are resonant in the visible (VIS) and NIR spectral regions

rendering them attractive for use in plasmonic devices. A comparison of this spectral behaviour is shown in Fig. 2.4b for three different metals. Of the noble metals silver yields the largest ratio of modulus of real ( $\epsilon'$ ) and imaginary parts ( $\epsilon''$ ) of its dielectric constant (at 650 nm,  $|\frac{-\epsilon'}{\epsilon''}| \approx 42.21$ ) giving a silver nanosphere a greater LSPR field enhancement compared to a corresponding gold ( $|\frac{-\epsilon'}{\epsilon''}| \approx 11.56$ ) or aluminium ( $|\frac{-\epsilon'}{\epsilon''}| \approx 2.37$ ) counterpart. This marks silver as a material of choice for plasmonics, but unfortunately it also has a tendency to oxidise requiring protective coatings to prevent this. The second highest enhancement arises with gold, whose nanoparticles are chemically stable and biologically compatible allowing them to be implemented for in vivo application. Increasing the NP's diameter by 5 nm increments, as in Fig. 2.4c, demonstrates in detail the red shift in LSPR peak position along with the increase in extinction cross section values. It is evident (even by visual inspection of the colloidal suspension) that by altering one of these parameters, NPs possessing entirely different optical properties are generated for which Mie theory offers a precise prediction.

#### 2.2.4 Substrate effect

The calculations performed above involve the case of a NP sitting in a homogeneous background permittivity, yet in this system the NPs are immobilised directly on a fibre platform, which needs to be accounted for. A significant limitation of Mie theory is that it does not allow scattering calculations of NPs on substrates. In order to include the effect of the fibre core an alternative approach is required to determine an effective refractive index,  $n_{\text{eff}}$ , accounting for the RI of both surrounding medium,  $n_{\text{medium}}$ , and substrate,  $n_{\text{substrate}}$ , before proceeding to use standard Mie calculations. Thus the silica fibre core can be treated as a planar substrate medium contributing to the permittivity in the vicinity of the NP. The NPs can be considered sufficiently small to effectively experience a flat substrate environment instead of the actual curved core, and an effective permittivity or refractive index can be assigned for the entire NP environment. The effective RI can be ascertained by incorporating an appropriate weighting factor,  $\eta_{\text{shell}}$ , for the surrounding indices [148]:

$$n_{\text{eff}} = \eta_{\text{shell}} n_{\text{medium}} + (1 - \eta_{\text{shell}}) n_{\text{substrate}}. \quad (17)$$

Here, an analytical approach to determining the weighting factor is implemented, which is based on the form of the NP environmental sensitivity. The NP's sensing volume is defined as a shell extending a radius distance from the NP surface (see Fig. 2.5). This radial dependence implies two routes to determining a reasonable weighting factor for the sensing volume [148]. One approach involves modelling a shell of uniform sensitivity around the NP surface that extends from the NP by the radius value. The second approach assumes an exponential sensitivity ( $1/e$ ) dependent on the radial distance from the NP. This is a more physically relevant route and is implemented in this work.

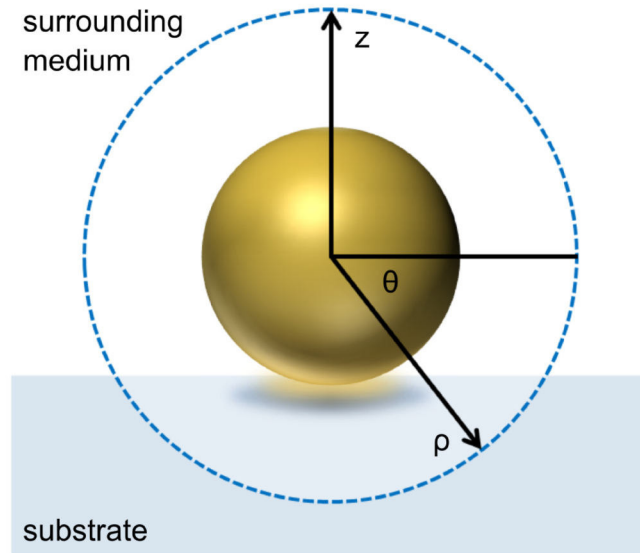


**Fig. 2.5:** Au NP on silica-core substrate with a sensing shell extending by the radius distance. The non-homogeneous NP background can be accounted for by implementing a weighting factor approach – lending closer comparison to real experimental conditions.

When the  $1/e$  sensing distance is equal to the NP radius [149–152] this approach yields a weighting factor,  $\eta_{\text{shell}} = 0.7$ , for the NP surroundings [148].

### 2.2.5 Performance characteristics of LSPR transducers

The extremely high surface-to-volume ratio offered by plasmonic NPs and the direct influence of the dielectric environment on their plasmonic characteristics lends these particles high potential in sensing minute variations in their local environments [153]. This section highlights the parameters important in quantifying the plasmonic sensor's performance based on RI changes. A number of these parameters are inherent to the plasmonic structure, with others displaying strong dependence on their surface functionalisation and the reactions occurring during sensing experiments. LSPR transducers present a relatively sharp resonant wavelength with a highly localised sensing zone. Changes in the surroundings, e.g. biomolecule adsorption, induce a variation in the LSPR extinction wavelength maximum, which may be calculated as for a SPR sensor [58] via

$$\Delta\lambda_{\text{peak}} = S_{\text{B}}\Delta n \left[ 1 - \exp\left(\frac{-2d_{\text{analyte}}}{l_{\text{d}}}\right) \right], \quad (18)$$

where  $S_{\text{B}}$  stands for the bulk RI response of the transducer,  $\Delta n$  the refractive index change,  $d_{\text{analyte}}$  the effective thickness of the adsorbate layer, and  $l_{\text{d}}$  is the EM field penetration depth [47]. The tunability of the plasmonic resonance and inherent NPs properties play a key role in optimising sensor performance. For instance, the geometric nanostructure design determines accessibility of analytes and position of hot spots (intense areas of field enhancement). A proper plasmonic nanostructure design results in high values



of transducer sensitivity,  $S$ , which is defined as the observed wavelength change of the plasmon resonance ( $\Delta\lambda_{\text{peak}}$ ) per refractive index unit (RIU), given in units of nm/RIU:

$$S = \frac{\Delta\lambda_{\text{peak}}}{\Delta n}. \quad (19)$$

Ultimately it is the sensitivity of the NPs that establishes the sensitivity of the system making the determination of  $S$  highly important. The bulk,  $S_B$ , and surface,  $S_S$ , RI sensitivities represent two important characteristics of LSPR sensors [113].  $S_B$  takes into account the changes occurring in the entire medium,  $\Delta n_{\text{medium}}$ , whereas  $S_S$  deals with those changes occurring within a layer around the particle,  $\Delta n_{\text{layer}}$ . The resonance wavelength sensitivity to a bulk change in RI of the medium can be determined by differentiating the resonance condition itself (Eq. 19), leading to  $S_B$  of the peak wavelength of

$$S_B = \Re \left[ \frac{d\lambda_{\text{peak}}}{dn_{\text{medium}}} \right] = \frac{-4n_{\text{medium}}}{\frac{d\varepsilon'_{\text{NP}}}{d\lambda}}. \quad (20)$$

In the same manner, for a spherical overlay layer at the NP surface the surface sensitivity can be determined (assuming small permittivity increase across the layer):

$$S_S = \Re \left[ \frac{d\lambda_{\text{peak}}}{dn_{\text{layer}}} \right] = \frac{-4n_{\text{layer}}}{\frac{d\varepsilon'_{\text{NP}}}{d\lambda}} \Delta. \quad (21)$$

$S_S$  additionally depends on  $\Delta$ , the volume fraction of the layer, given by

$$\Delta = 1 - \frac{r_{\text{NP}}^3}{(r_{\text{NP}} + d_{\text{analyte}})^3}, \quad (22)$$

where  $d_{\text{analyte}}$  indicates the layer thickness, and  $r_{\text{NP}}$  is the nanosphere radius. It follows that in the sparse layer approximation (layer RI not significantly greater than bulk RI),  $S_S$  is equivalent to the bulk RI sensitivity times the factor corresponding to the portion of the total “field volume” the layer possesses. Considering an analyte layer thickness equivalent to the NP radius, this factor is 0.875. The bulk and surface sensitivities are then related by  $S_S = S_B \Delta$ . Hence, by maintaining a fixed layer thickness, an increasing particle size exhibits lower surface RI sensitivity. For instance a layer thickness of 5 nm around a gold nanosphere of diameter 34 nm results in an  $S_S$  of 46.20 nm/RIU compared to the same layer on an 80 nm diameter NP yielding  $S_S$  of 45.67 nm/RIU. This example is calculated from the theoretical values of  $S_B$  determined in Tab. 1 for a NP suspended in solution. This effect of reduced surface sensitivity is however partly compensated by the general sensitivity increase with increasing particle size presented by bulk RI sensitivity. Theoretical analysis in literature shows that  $S_B$  increases with the resonance wavelength, regardless of the NP’s shape [113, 154, 155].

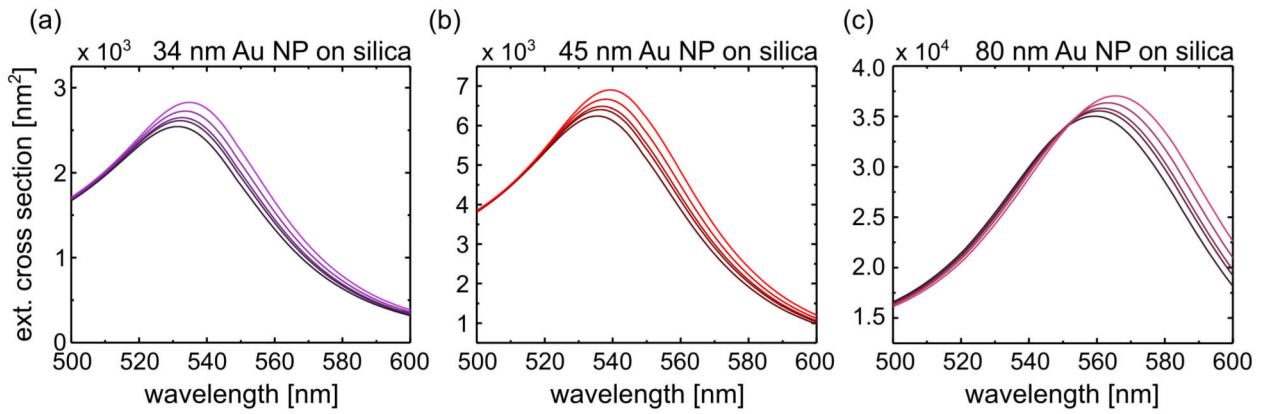


**Fig. 2.6:**  $C_{\text{ext}}$  spectra calculated for changing RI analyte around a gold nanosphere on a silica substrate. The implemented NP diameters are (a) 34 nm, (b) 45 nm, and (c) 80 nm. The lighter colour indicates a higher RI analyte ranging from 1.368 to 1.410 RIU.

Implementing Mie theory, the change of resonance peak position with bulk RI variation for a particular NP size can be tracked (Fig. 2.6). Plotting this behaviour for the NPs used in this work enables a comparison of their sensitivity both in solution and using an effective refractive index to account for the substrate effect. Determination of the latter can be seen in Fig. 2.7, with further details in Tab. 1. The sensitivity values of NPs on a silica substrate can be seen to be reduced as less particle surface is available for detection. An advantage of implementing LSPR for plasmonic sensing is the compact sensing volume it offers. This leads it to being more sensitive to molecular binding events and less sensitive to bulk effects, resulting in reduced bulk signal interference. It should be noted that this sensitivity is also nanostructure dependent and yields different values for different plasmonic modes.

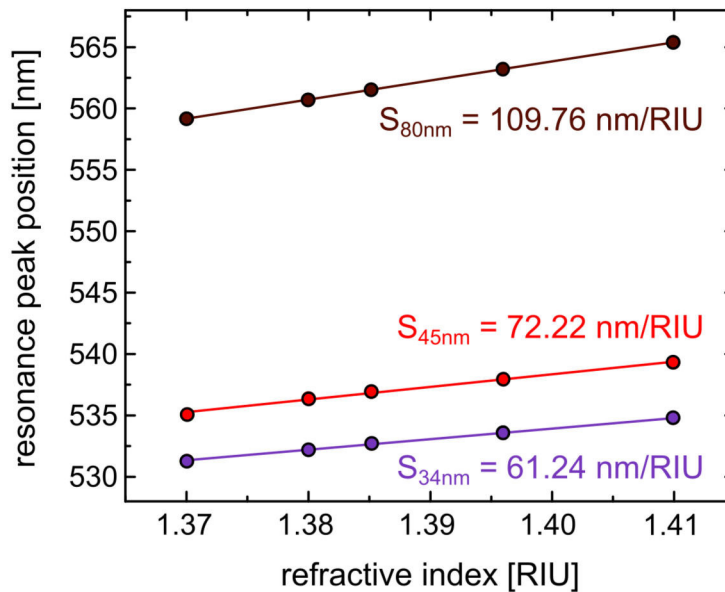


**Fig. 2.7:**  $\lambda_{\text{peak}}$  calculated for a range of effective RI surroundings for Au NPs on silica substrate. The purple line indicates a 34 nm NP diameter, the red line a 45 nm NP diameter, and the darker burgundy line an 80 nm NP diameter. The slope of each data set multiplied by the weighting factor, here 0.7, yields the NP bulk sensitivity.

Further important parameters in LSPR sensing include the resonance peak width and correlated figure of merit (FoM) [154, 156], which provides a reliable unit-less expression of sensor performance, relating the resonance peak FWHM (full width at half maximum,  $\Gamma$ ) to the sensor's sensitivity:

$$FOM = \frac{\Delta\lambda_{\text{peak}}}{\Delta n} \frac{1}{\Gamma}. \quad (23)$$

Larger FoM values allow more accurate resonance position determination enabling smaller spectral shifts (lower detection limit) to be observed – crucial for low concentration analyte sensing. An overview of the sensing characteristics of the implemented NPs is provided in Tab. 1. In the case of a NP fixed on a silica substrate the approach from Sec. 2.2.4 is implemented. The NP experiences a higher effective refractive surrounding than that of the colloidal suspension, increased  $\lambda_{\text{peak}}$ , and thus higher  $S_B$  – which is then multiplied in Tab. 1 by a weighting factor of 0.7 from Eq. 17. The resulting sensitivity values for the NP-on-substrate case are then reduced as expected since there is less NP surface available for sensing. The corresponding FOM values are closely comparable to other NP LSPR sensors in literature [113, 154].

Table 1: **Overview** Sensing characteristics of the implemented NPs in solution and on silica substrate as calculated from Mie theory.  $S_S$  is calculated for a layer thickness corresponding to the radius of each NP size. NP dia. indicates the NP diameter.

	NP dia. [nm]	$\lambda_{\text{peak}}$ in water [nm]	$S_B$ [nm/RIU]	$S_S$ [nm/RIU]	$FOM_B$ [1/RIU]	$FOM_S$ [1/RIU]
solution	34	528.18	85.78	75.06	1.05	0.92
	45	531.94	95.05	83.17	1.15	1.00
	80	553.54	153.43	134.25	1.64	1.44
substrate	34	531.35	61.24	53.59	0.77	0.67
	45	535.09	72.22	63.19	0.90	0.78
	80	559.18	109.76	96.04	1.20	1.05

### 2.2.6 Influencing NP spectral properties

Aside from material and size considerations other factors can contribute strongly to a NP's spectral behaviour. Here three highly relevant considerations are included for completeness.

#### Shape

Increasing the edges or sharpness of a particle results in an extinction spectrum red shift due to an increase in charge separation [46]. On the other hand, increasing the particle symmetry increases the intensity of the LSPR. The number of resonances a NP exhibits depends on the number of modes in which it can be polarised [131, 157]. Shape-anisotropic NPs are sensitive to incident light polarisation with nanorods showing longitudinal and transverse resonance states [158] and a spectral maximum further

depending on the incoming polarisation. The RI sensitivity is also influenced by shape. Literature [53,159] cites Ag nanorods as exhibiting higher sensitivities than Ag triangles, with spherical geometry yielding some of the lowest sensitivities. High aspect ratio or sharp edged NPs usually yield LSPR spectra containing several modes and high sensitivity.

### Composition

A hollow-core NP produces a dramatic spectral red shift without changing the NP size, enabling Ag nanoshells to have LSPR in the NIR yet remain below 100 nm in size. Such a structure can additionally play vessel to analytes, drugs, or contrast agents for imaging [160].

Conversely, a nanoshell could be developed over the surface of a dielectric core – as its thickness increases, the resonance position would blueshift [161]. As core-shell and anisotropic NP geometries offer higher sensitivity, the efficiencies of many ex vivo, homometallic, or spherical NPs, could be enhanced by adding a defined silver shell [162, 163]. One further option for plasmonic tailoring involves metal alloys [145], providing optical properties and application distinct from their pure nanostructure counterparts [160, 164, 165].

### Interparticle coupling

In an ensemble of NPs, electromagnetic interaction (dipole interaction) between localised modes [166] can induce spectral resonance shift. In a dipole approximation with the NPs acting as point dipoles, two separate regimes can be remarked on. In the first, with distance  $D \ll \lambda$ , near-field coupling dominates (distance dependence of  $D^{-3}$ ). The ensemble acts as a point dipole array coupling via their near-field. This array can produce “hot spots” for field enhancement. In the other case involving large NP separations, far-field dipolar coupling dominates [108] (distance dependence of  $D^{-1}$ ). In brief, the highest field enhancements are achieved with shorter separation between particles of equal potential. The charge distribution of neighbouring NPs can further affect the strength of the restoring force on a NP’s oscillating electrons. This depends on the incident polarisation; transverse mode excitation incurs a resonance blueshift, whereas longitudinal mode excitation induces a redshift [167]. A number of theoretical studies aim to predict this interaction [168, 169]. At extremely small distances, as the NP separation enters the nanometre and subnanometre scale, quantum effects need to be considered [170–172].

The final noteworthy consideration is the case of NP aggregation. It has been shown that individual gold NPs coupling electronically in an aggregate result in a second plasmon absorption resonance at longer wavelengths [133, 173]. The oscillating conduction electrons in one NP experience the electric field from those of neighbouring NPs, leading to a collective plasmon oscillation of the total aggregated system. The frequency and intensity of oscillation is influenced by the aggregation degree as well as on the individual NP orientations in the aggregate [133, 173, 174].

### 2.3 Platform – microstructured optical fibre (MOF)

As introduced, optical fibres offer an attractive platform for exploiting nanoparticle functionality. They offer plasmonic sensing platforms superior to their planar contemporaries in that they are cheap, flexible, compact, and robust. Fibres composed of large interior microstructured channels, as in this work, may be flushed with fluidics both directly and without compromising structural stability. A long interaction length can then be accessed even with a very low sample volume. A myriad of optical fibre configurations and materials exist, in this chapter the basic principles and ideas behind applying optical fibres for sensing are highlighted. When selecting optical fibres as the plasmonic sensing platform the optimal fibre configuration must be further taken into account with respect to:

1. Light guidance – how efficient are the plasmonic excitation and experimental launching conditions?
2. Available mode overlap – is the interaction with NPs and analytes sufficiently high?
3. Accessibility for deposition and sensing – can the plasmonic NPs be readily immobilised using this geometry and can the same region be accessed for sensing afterwards?
4. Robustness of sensing region – is the target sensing region suitable for measurement and reuse?

#### 2.3.1 Light propagation in optical fibres

In order to understand the propagation of light through an optical fibre the general concept of a fibre mode and guidance needs to be introduced. To arrive at such a description a wave equation describing the propagation of electromagnetic (EM) waves is required.

For the case of dielectric optical media (devoid of free charges or magnetic polarisation) the guided wave can be described by a set of optical eigenmodes. These eigenmodes may be calculated in cylindrical coordinates by solving Maxwell's equations in the fibre's core and cladding regions and applying appropriate boundary conditions. Since the comprehensive analytic derivation of such waveguide eigenmode solutions is extensively available in literature [175, 176], here the key wave equation, the Helmholtz equation, for the electric field in the frequency domain is directly presented as

$$\nabla^2 \mathcal{E}(\mathbf{r}, \omega) + k_0^2 \epsilon \omega \mathcal{E}(\mathbf{r}, \omega) = 0, \quad (24)$$

with  $k_0 = \frac{\omega}{c}$  being the vacuum wave number, and  $\mathcal{E}(\mathbf{r}, \omega) = \mathcal{E}(x, y, \omega)$  describing the fibre transverse geometry. The corresponding eigenmode solutions are the fibre modes of the form

$$\mathcal{E}(\mathbf{r}, \omega) = \mathcal{E}(x, y, \omega)e^{ik(\omega)z}. \quad (25)$$

Thus information on both the mode profile shape and phase are included in these solutions. Additionally, a complex value of  $k$  from the eigenmode solutions indicates mode decay. For the case of monochromatic plane waves, the Helmholtz equation yields trivial solutions that follow the linear dispersion relation

$$|k| = \sqrt{\varepsilon(\omega)} \frac{\omega}{c_0}. \quad (26)$$

with  $c_0$  being the speed of light. The dispersion relation is furthermore proportional to what is known as the complex refractive index

$$\bar{n}(\omega) = \sqrt{\varepsilon(\omega)} = n(\omega) + i\kappa(\omega). \quad (27)$$

This term is an important fundamental property of optical materials that contains full information on optical diffraction and refraction (from the real part,  $n$ ), and optical loss or gain (from the extinction coefficient,  $\kappa$ ), for that particular medium. It is also related to the material absorption at a wavelength  $\lambda$ , through:  $\alpha = \frac{4\pi\kappa}{\lambda}$ .

Analytical solutions to the wave equation can be obtained directly only for a few simple optical systems. One system allowing rigorous analytic treatment is the step-index fibre waveguide. The step-index fibre is a more “conventional” optical fibre geometry, comprised of a longitudinal invariant core region of higher refractive index material,  $n_{co}$ , surrounded by a cladding region of lower refractive index,  $n_{cl}$ , as illustrated in Fig. 2.8. An example would be a silica cladding and a uniform germanium-doped core whereby  $n_{cl} < n_{co}$ . The cladding is encased in a further lower RI coating. Light launched into the fibre below a certain critical angle (termed the Numerical Aperture, NA) is guided by total internal reflection (TIR) at the core-cladding (high-low RI) interface and confined to the core region.

The precise analytic solution for cylindrically symmetric fibres is given in literature [175] and can be solved numerically. For a specific fibre’s mode, the corresponding eigenvalue of the propagating mode can be found. Depending on parameters such as core diameter and numerical aperture, a fibre can support various numbers and types of modes. Modes can be differentiated by field distribution, polarisation, and propagation constant,  $\beta$ . Particularly important for this study is the fundamental mode, which provides the highest field overlap with the core region (with Gaussian like intensity distribution), and thus the largest effective mode index  $n_{eff} = \beta/k_0$ . It additionally exhibits two degenerate polarisation states with the same propagation constant. In contrast to higher-order modes, the fundamental mode can be readily excited in a consistent and

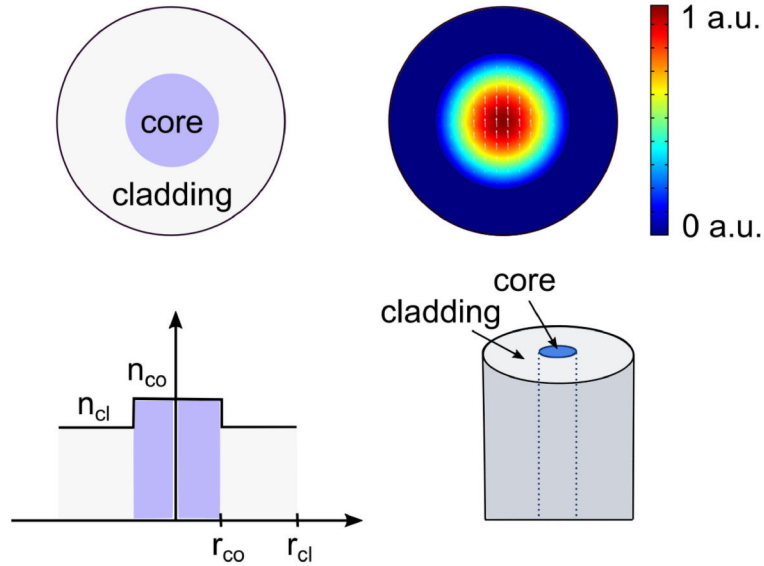


**Fig. 2.8:** Step-index fibre with RI profile in core and cladding as indicated. The calculated intensity and polarisation profile of the degenerate fundamental optical mode is shown for an RI contrast of  $\Delta n = 0.01$  and  $r_f = 50 \mu\text{m}$  at  $650 \text{ nm}$ . The inner black circle in the mode image indicates the fibre core.

isolated manner. Certain fibre designs can support single mode propagation where below a certain cut-off frequency, determined by the fibre, higher-order modes are no longer bound and single mode propagation prevails. Single or multimode guidance can be characterised using the frequency normalised V-parameter [175]:

$$V = 2\pi \frac{r_f}{\lambda_0} \sqrt{n_{\text{co}}^2 - n_{\text{cl}}^2}. \quad (28)$$

Where  $r_f$  is the fibre radius. If  $V < 2.405$ , the fibre operates in the single mode regime. Additionally, the V-parameter can be used to approximate the number of modes,  $M$ , through:  $M \approx \frac{V^2}{2}$ .

### 2.3.2 Introduction to microstructured fibres

This work deals with a more structurally involved fibre type: Photonic Crystal Fibres (PCFs), otherwise referred to as Microstructured Optical Fibres (MOFs), (Fig. 2.9). These fibres possess geometries incorporating longitudinally invariant arrays of air-filled structures running along their entire length, encased by a dielectric medium. MOFs can also refer to fibres containing optically resonant elements at single or multiple locations along their length.

Microstructured fibres are widely implemented as they enable a broad tailoring scope of light-guiding parameters, such as dispersion or nonlinearity, by adjusting the design of their microstructures (shape, size, or position relative to one another). Depending on their light guiding mechanism, MOFs may be differentiated into two distinct categories: hollow or solid core. The hollow core class possesses a low refractive index core and employs methods such as photonic bandgap guidance (a result of the periodic hole lattice throughout the cladding, Fig. 2.9a) or antiresonance guidance (a result of strand

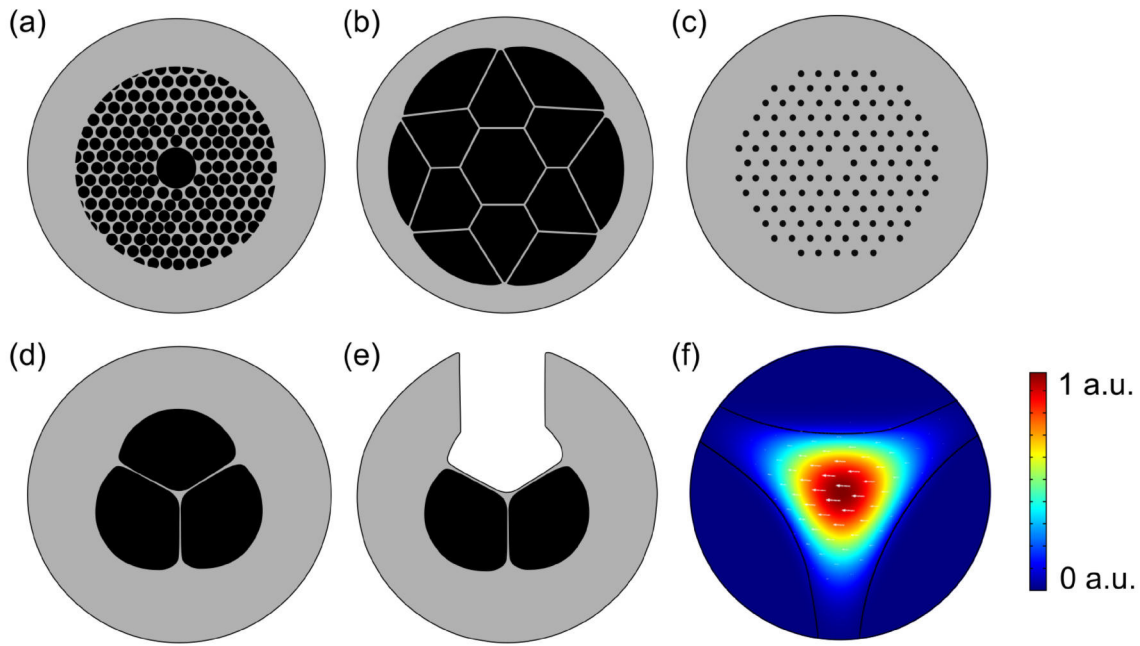


**Fig. 2.9:** Assortment of existing MOF designs with light-grey regions representing silica and black regions air-filled microstructure. (a) Hollow-core photonic bandgap fibre, (b) hollow-core antiresonant fibre, (c) endlessly single mode PCF, (d) SC-MOF, (e) ECF, and (f) electric field intensity distribution of the horizontally polarised SC-MOF fundamental mode.

reflection antiresonant to the guided mode, Fig. 2.9b). This hollow core MOF geometry enables fully filled core sensors [177, 178], presenting transmission windows in the UV and MIR, and multifold advantages for working in the high power regime.

Guidance in solid-core MOFs (as in Fig. 2.9c-e) can be accomplished through a high refractive index core, by way of Modified Total Internal Reflection (M-TIR) principle (analogous to TIR in step-index fibre guiding). The contrast between high index (pure silica) core and low index microstructured (air-filled) region enable this. Sensing is then possible through the evanescent tail overlap of the guided mode field with some portion of the surrounding microstructured channels. The solid core allows NP immobilisation directly on the core walls, enhancing overlap with the sensing region. This MOF class presents a powerful method for controlling the optical mode dispersion landscape, adjusting modal confinement, and tuning the field profile for interaction in the sensing regions.

The fibre of choice in this work is of the solid-core MOF class: a suspended-core fibre (SCF). The first SC-MOF cross section implemented consists of a solid silica rod (core) suspended by thin silica struts separating three enclosed “pie-slice shaped” microstructured channels, as in Fig. 2.9d. The SC-MOF contains in total three suspension struts, or bridges, and three holes and is also referred to as a Mercedes’s fibre due to the logo resemblance.

A second fibre type is also implemented, closely resembling the SC-MOF but with one open channel exposing the fibre core and two of the suspending struts, as in Fig. 2.9e. This is termed an exposed-core fibre (ECF). These solid, suspended-core geometries facilitate NP functionalisation on the core walls and offer higher proximity for evanescent field overlap than non-suspended extrinsic sensor geometries.



SCFs are often initially modelled as a cylinder (core) of silica in air (cladding), acting as a step-index fibre. SCFs, being comprised of a virtually suspended core and system of thin suspending struts, have an effective core-cladding RI contrast very close to the contrast of silica-air – thus presenting some of the highest numerical aperture, NA, fibres. The NA (which may numerically exceed 1) is determined by:  $NA = \sqrt{n_{co}^2 - n_{cl}^2}$ , which for a silica core suspended in air with  $n_{co} = 1.45$  and  $n_{cl} = 1.00$ , gives an NA of 1.05. The NA can also be measured experimentally to account for other influences such as the struts, by in-coupling a white light source and analysing the far-field pattern of the output spot.

For the real MOF geometry, in contrast to the step-index fibre, no analytical solutions exist for the guided mode. Yet the effective mode index of guided modes of the SCF can be calculated. The highest mode index is held by the fundamental mode, which exhibits two degenerate polarisation states one of which is shown in Fig. 2.9f. Typically a finite element simulation (COMSOL) is run on imported scanning electron microscopy, SEM, images to model the SC fibre geometries and determine their mode information (Ch. 3).

### 2.3.3 Suspended-core MOF for evanescent field sensing

The suspended core of this MOF can carry the wavelength mode over an extremely long fibre length, providing an extended interaction distance of the electromagnetic probe and the microstructure filled sample. The mechanism behind SCF evanescent field sensing is as follows: the core waveguide mode is not entirely confined within the core, but rather possesses evanescent tails that can overlap with some portion of the outer microstructured regions. This is a purely wave optics phenomenon, which arises from the requirement of having continuity conditions of the EM fields at the boundary. Evanescent fields are characterised as possessing at least one imaginary component of the wavevector,  $k$ , describing the direction of propagation. In the spatial direction defined by that imaginary component, the wave decays exponentially. This evanescent tail can interact with and experience changes in the sample (RI change for instance).

As will be shown in Ch. 3, the MOF designs implemented in this work allow the possibility of high evanescent field overlap with the microstructured channels for enhanced sensing applications. The large microstructure sizes facilitate analyte filling and the NP immobilisation process.

During the NP immobilisation process, gold NPs are deposited around the channel curvature within the fibre. These fixed NPs exhibit highest loss at a particular resonance frequency that depends on the surrounding medium's RI (amongst other factors). When the RI of the immediate NP environment is varied (by analyte exchange or a binding event), the NP's loss spectrum also shifts in frequency. The evanescent tail of the guided mode of the suspended core interacts with the NPs fixed on the exterior of the core wall and experiences loss through absorption and scattering. If the LSPR mode undergoes a change in its own loss (extinction) spectrum, a response in the spectrum of the guided core mode ensues (Fig. 2.10). By monitoring the transmitted power of the fibre's guided

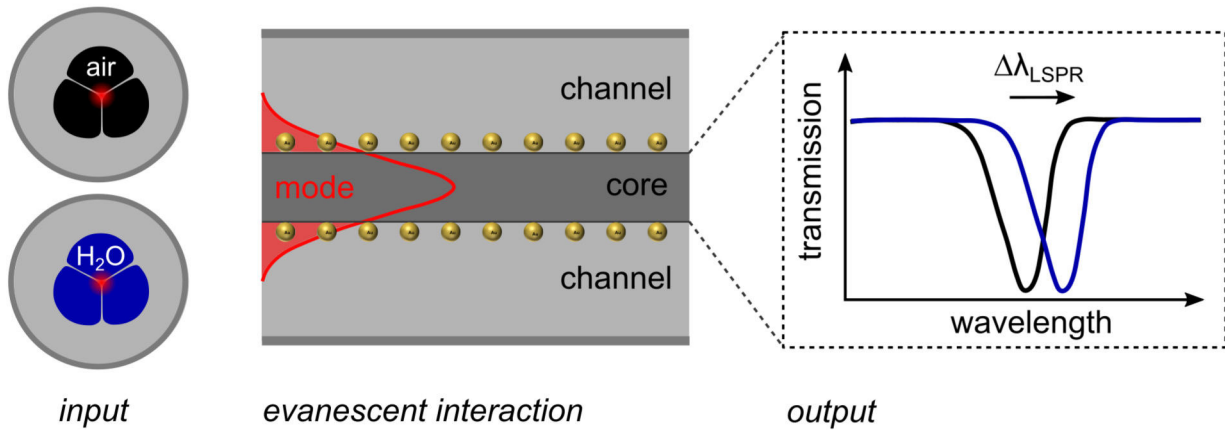


**Fig. 2.10:** Evanescent-field MOF sensing. A propagating fibre mode (red profile) has evanescent tail overlap (light red area) with NPs fixed on core walls. Changing the microstructure environment from air (black) to water (blue) induces a shift in the NPs resonance position,  $\Delta\lambda_{\text{LSPR}}$ , that is felt by the evanescent mode field and appears in the output fibre transmission spectrum.

core mode at the output facet, this response can be detected and traced back to the initial change that originally occurred within the microstructured region. In this way, SCFs can be used as self-contained, real time sensors. In Ch. 3.1 an in-depth analysis is conducted into the relation between SCF geometry and interaction overlap for particle detection. The power attenuated by the NPs and the loss imposed by various NP densities is investigated both theoretically (Ch. 3.2) and by experiment (Ch. 5).

#### 2.4 Biorecognition element – DNA detection

A biosensing system, as discussed, provides both detection and sensing transduction, and must therefore incorporate a biological sensing or “biorecognition” element. The selection of biorecognition element is based on the target of interest and is crucial to providing specific binding. Various recognition elements can be incorporated as a biorecognition layer to accomplish this, including enzymes, antibodies, antigens, receptors, nucleic acids, lipid membranes, viruses, etc. [179–181]. Ideally the biorecognition element should possess further properties such as stability, functionality and reversibility to ensure high performance. Two classes of biosensors can be distinguished, according to the nature of the recognition event [182]:

1. Bioaffinity sensors: based on the selective binding of a target analyte to a surface-confined ligand partner, e.g. an antibody or an oligonucleotide as used in this work.
2. Biocatalytic sensors: based on target recognition by an immobilised enzyme, e.g. biosensors with immobilised glucose oxidase sensor strips used for monitoring diabetes.

The focus of the plasmonic MOF sensor is on nucleic acids, specifically DNA as a biorecognition element. For nucleic acid based biosensors, the biorecognition elements are oligonucleotides, possessing known base sequence, or a DNA/RNA fragment. The

recognition process takes advantage of the highly specific hybridisation of complementary strands of DNA/RNA molecules, i.e. the principle of complementary base pairing, which for DNA involves adenine-thymine and cytosine-guanine pairs. If the target nucleic acid sequence is available, the complementary sequence can be synthesised and immobilised as the biosensing layer. The immobilised probe or capture ssDNA hybridises, forming a base pair with its complementary target DNA, completing a binding event whose transduction is measured depending on the chosen transducer (Sec. 2.1, [6]), for instance an optical signal in the case of an optical biosensor. The biorecognition layer is typically integrated with the transducer surface via: adsorption, cross-linking, or covalent binding. The latter, as discussed later, being the most prevalent in the case of ssDNA immobilisation on gold.

DNA based biosensors are of great developmental interest for rapid, inexpensive, and simple gathering of sequence-specific information, outperforming other traditional hybridisation assays [183]. Target applications include testing of infectious and genetic diseases, detection of DNA damage, and interaction studies. Currently, nucleic acid biosensors can be rendered even more specific and sensitive by a combination with polymerase chain reaction (PCR) methods, which exponentially amplify (replicate) sequences [184,185]. A further advantage of this element selection is that unlike antibodies or enzymes, nucleic acid sensing layers are readily synthesised and regenerable – promoting multiple use sensors.

When considering DNA inclusion as a biorecognition element certain factors need to be addressed such as the attachment dynamics between DNA and transducer, optimising the capture DNA attachment, and ruling out unspecific binding events. Other details including working DNA spacer lengths, concentrations, and dehybridisation strategies should also be studied. In the following sections these concepts are discussed in brief.

#### 2.4.1 Hybridisation based affinity detection

Hybridisation is based on the principle of complementary base pairing of sequences, for DNA these pairs are adenine-thymine and cytosine-guanine. When brought together the bases bond to complementary bases via hydrogen bonding as shown in Fig. 2.11. The final hybridised structure is the wound helical DNA structure composed of two antiparallel ssDNA strands. Hybridisation can be achieved in solution phase between randomly distributed capture and target DNA, or be performed with the capture DNA tethered to a surface in a solid-phase hybridisation [186]. In an LSPR scheme, the capture DNA is immobilised on the transducing NP surface and is thereafter available for hybridisation with target DNA from introduced solutions. This strategy enables non-specific binding sequences to be rinsed away from surfaces, isolating the remaining strongly bonded capture-target pairs – creating what is referred to as a heterogeneous assay. It also allows for sensor regeneration (see Sec. 2.4.3).

The resulting hybridisation efficiency is affected by the density of surface capture DNA, its conformation, and the surface curvature on which it is tethered [187,188]. Nat-

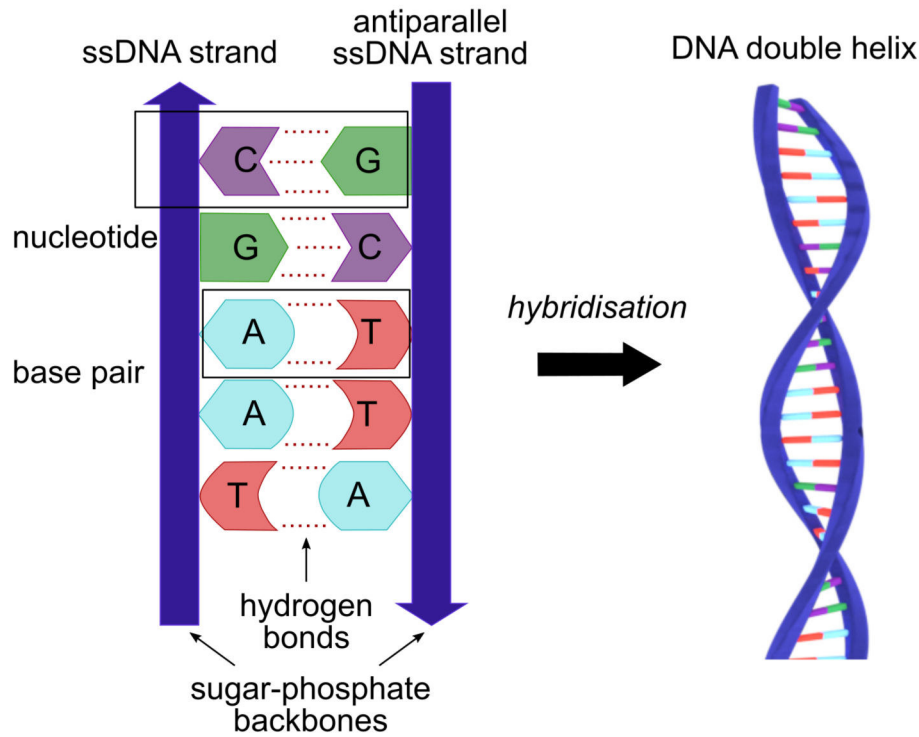


**Fig. 2.11:** ssDNA strand composition containing sugar-phosphate backbone and base pairs (C denoting cytosine, G guanine, A adenine, and T thymine). When two identical ssDNA strands are brought together, in an antiparallel configuration, the bases bond to complementary bases via hydrogen bonding in a hybridisation process. This results in a wound helical DNA structure as outlined; precise renderings of the double helix structure can be found in literature [189, 190].

usually the binding affinity between capture and target DNA also affects this. In general a higher accessibility promotes more efficient hybridisation, yielding stronger signals.

#### 2.4.2 DNA on gold surfaces – immobilisation and alignment

As the transducing gold nanospheres are highly sensitive to changes in their immediate vicinity, in order to achieve highest sensitivity the capture ssDNA should be immobilised directly on the NP surface. This surface immobilisation can be achieved by direct or covalent adsorption approaches (involving electrostatic interaction or thiol/amino/silane groups, with click or NHS/EDC chemistry [53]).

For the ssDNA fixation to gold the functionalised probe targeted for this work consists of a thiol head group ( $-SH$ ), an alkyl backbone chain, and a functional tail group in the form of the ssDNA strand [6, 191–193]. The thiol group possesses a strong affinity to metal surfaces with a bond strength surpassing that of amines ( $-NH_2$ ) in the order:  $Au-SH > Au-NH_2 > Ag-SH > Ag-NH_2$ . This is an example of covalent immobilisation involving the spontaneous organisation of thiolated ssDNA, from solution, into a self-assembled monolayer (SAM) on the NP surface as shown in Fig. 2.12. The SAM process of thiol groups on gold surfaces is not fully elucidated but it is thought that the adsorption process consists of two or three kinetic steps, which are proposed in literature [194, 195].

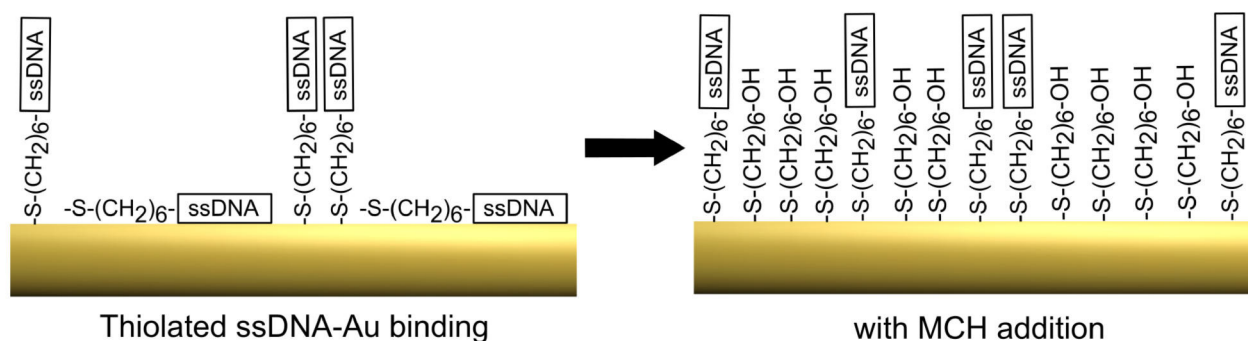


**Fig. 2.12:** Thiolated DNA binding on planar gold surface showing strand alignment and accessibility with ssDNA alone, and after addition of blocking agent MCH.

A further option for DNA adsorption to positively charged NPs is direct adsorption, which forgoes the need for nucleic acid modification. Since DNA is negatively charged at neutral pH [187], it can be directly adsorbed on a positive surface. However, the NPs implemented in this thesis are fabricated by a citrate reduction technique (see Ch. 4.2) and are stabilised by weakly adsorbed citrate ions. In total the nanoparticles possess a slight negative charge on their surface that would require an additional positively charged layer in order to directly immobilise DNA in this manner. Furthermore, the DNA would tend to align horizontally (bind to the surface along its chain rather than at one end), occupying binding space at the surface and decreasing available hybridisation sites for target DNA. In implementing a thiolated covalent-adsorption approach, the DNA being negatively charged leads to a certain repulsion between the strands and the gold nanoparticles that reduces this aforementioned strand-particle binding.

Two critical points to consider throughout are the accessibility of the capture DNA and the affinity of the target DNA to the sensor adsorbed ssDNA. As such, blocking agents including short alkanethiols, e.g., 6-mercapto-1-hexanol (MCH), are coadsorbed to bind, also by a thiol terminal group, and block the remaining NP surfaces (as proposed in [196–198]), thereby reducing binding along the DNA strand and maximising accessibility for target DNA hybridisation. The remaining surfaces can be protected from unspecific DNA binding by pacifying with herring sperm DNA [79]. The contrast between thiolated ssDNA binding to a gold substrate in the absence and presence of MCH is shown in Fig. 2.12.

Accessibility is also affected by the curvature of the NP surface. Closest to the NP surface, the packing density is highest, with disorder increasing with distance. Fig. 2.13 shows a deflection angle for each bound thiol group that is induced by the NP curvature and enables higher density near the NP surface. Moreover, studies have shown that increasing the surface curvature enables higher adsorption of ssDNA strands [199], thus smaller NPs allow for higher numbers of adsorbed capture probes.

The capture probe density should not hinder hybridisation accessibility for the target DNA. Typical density values in the order of  $1 \cdot 10^{13}$  probes/cm<sup>2</sup> suffice [200]. A higher density of capture DNA is introduced than of target species; enabling detection of low target concentrations. Typically 20–24 synthetic base pair lengths are used with 0.34 nm

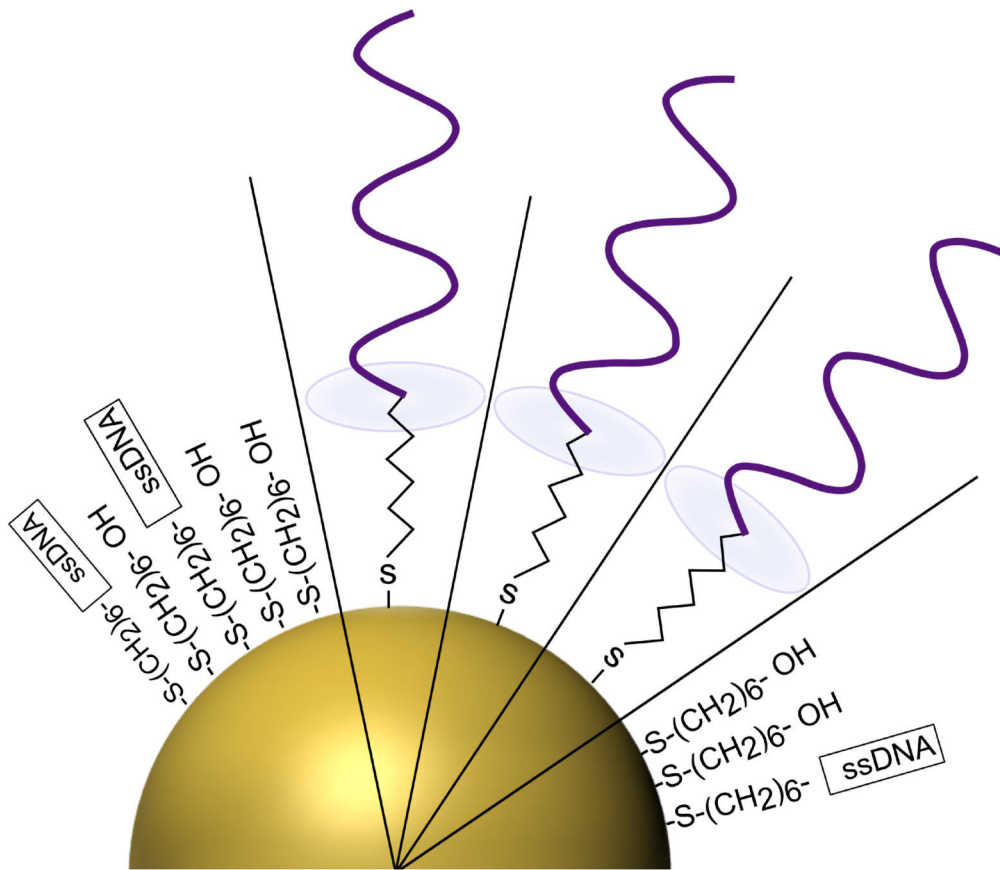


**Fig. 2.13:** Thiolated DNA and blocking agent MCH binding on curved gold surface showing strand alignment and enhanced density due to deflection angle for binding.

length per base pair (in double-stranded physiological conformation B). This provides sufficient sequence specificity without hindering target DNA attachment.

#### 2.4.3 Regeneration of sensor

The regeneration of the surface immobilised capture probe lends a strong advantage to DNA biosensors: surface tethered capture DNA is reusable without affecting hybridisation efficiency.

Denaturation can be induced by thermal or chemical means. The thermal approach involves heating to  $90^{\circ}\text{C}$ , which may induce bubbles in fibre channels or microfluidic chips. Hence a chemical approach to regeneration is attractive. A number of possibilities for chemical denaturation exist, for instance, exposure to 1 or 10 mM hydrochloric acid (HCl) [201, 202], or to 10 mM sodium hydroxide (NaOH) solution for 1 minute [203]. Overall, regeneration by chemical means permits a faster execution, and can be implemented at room temperature.

## STUDY OF SENSING PROPERTIES OF SMALL-CORE MICROSTRUCTURED FIBRES

---

The fundamental operating principle of this NP-functionalised MOF sensor is based on interaction of the propagating guided mode with the NPs' LSPR, where the characteristics of the latter are impressed on the transmitted light spectrum. As the guided mode's evanescent field penetrates the microstructured channels and excites the gold NPs' LSPR, a corresponding portion of EM energy is redacted (via scattering and absorption) from the transmitted optical spectrum. Hence if the fibre system is to possess sufficient sensitivity, the modal attenuation spectrum must reflect any spectral shift of the LSPR imposed by change of nanoscale RI. This system sensitivity is derived from the NP sensitivity itself, which determines the spectral shift with such nanoscale RI variation, and the degree of evanescent field overlap with the NPs contributes to the detectable signal intensity.

In Ch. 2.2 the effect of refractive index variation of the surrounding medium on the loss spectrum of a metal NP was discussed. Here the method adapted by this study to quantify the loss experienced by the MOF mode due to the presence of these NPs is outlined. The starting point involves an investigation of the guided mode of the bare fibre, determining an effective modal scattering area of the non-plasmonic system and, by extension, the fraction of the field available for potential NP interaction at the core walls. This modal scattering area parameter is essential for calculating NP scattering on a waveguide. The NP contribution through extinction cross section and particle number is introduced in a final analytical formula for the NP-functionalised fibre's modal attenuation, culminating in a theoretical sensitivity of the entire deposited system. The results of this analytical approach are partly published in [105, 106].

Since this concept is predominantly based on the portion of evanescent field probing the microstructured region and exciting the LSPR, this chapter provides a study of a number of bare MOF samples, of various core sizes and refractive indices, simulated by finite element method in COMSOL to determine their modal attenuation and by extension applicability to NP based fibre sensing. A comparison of the effect of modal attenuation in the case of air or analyte filled microchannels is studied, as well as an investigation between small-core suspended MOFs and correspondingly sized fibre tapers – renown for offering high levels of detection sensitivity [97, 204]. The critical questions answered in this chapter include:

1. Can an ECF or SC-MOF geometry offer adequate evanescent field overlap for plasmonic sensing?
2. How can the NP induced modal loss be estimated?
3. How does the chosen ECF or SC-MOF compare with taper systems in terms of sensing?

### 3.1 Study of geometry and composition effects for SC-fibre sensing

With regard to the fibre platform, higher NP interaction and enhanced attenuation should be achieved by increasing the portion of the propagating mode's power contained in its evanescent region. The evanescent field fraction supported by a particular fibre is the direct result of the suspended core diameter, its dielectric refractive index, and also the width of the suspending struts. This chapter investigates numerically whether a small silica core can offer significantly higher evanescent field fraction than a larger silica core where the field may not penetrate the channels as strongly. Further calculation determines whether a similarly sized, higher refractive index fibre core offering stronger field confinement could also be a viable option for sensing or if the anticipated lower channel overlap and interaction would hinder modal attenuation values significantly. The higher RI cores modelled correspond to a tellurite,  $\text{TeO}_2$  containing [205], and a chalcogenide,  $\text{As}_2\text{S}_3$ , glass composition. It is necessary to determine this geometry effect in advance, instead of aiming for an overly reduced core size where confinement loss may start to dominate as the evanescent field reaches further into the cladding and escapes. The resulting decay length would limit sample interaction length [114]. Thus a trade-off between NP interaction, through modal overlap, and decay length exists and should be kept in mind.

The suspending strut width can also affect higher order modal loss and chromatic dispersion [206] especially at high thicknesses. However, since only the fundamental guided mode is of interest in this study, and extremely low strut widths are more challenging to fabricate due to strand breakage, only available thin strut samples (100–500 nm thickness) were implemented. Ultimately, with a specific sensing architecture in mind, a core size for optimal overlap should be chosen and other design parameters tailored accordingly.

To determine the detection potential of the SC-MOF structures, the starting point is to investigate the guided mode of the bare fibre and determine the evanescent field overlap available for sensing. Ideally this value is high since it is this contribution that enables LSPR excitation and is responsible for the resulting signal intensity during detection. However it should not be so high as to attenuate the signal completely or limit the sample to a reduced, unmanageable length. Ch. 2.3 introduced the steps to finding the waveguide mode profile of the SC-fibres and to determining the mode's effective refractive index, a number that could be complex if the mode is lossy. Ch. 5 further demonstrates how to experimentally realise optical mode guidance and how to determine the modal attenuation of a bare SC-fibre and its NP-functionalised counterpart. In this section, finite element simulation (via COMSOL) is implemented to model a range of SC-fibre structures, determine their mode profiles and apply these to compare sensing capacity. The geometric core sizes can be defined as in Fig. 3.1a, either by the diameter of the largest inscribable circle within the core, or as in this work, by the circle equivalent of the area of the largest inscribable equilateral triangle within the core [207, 208].



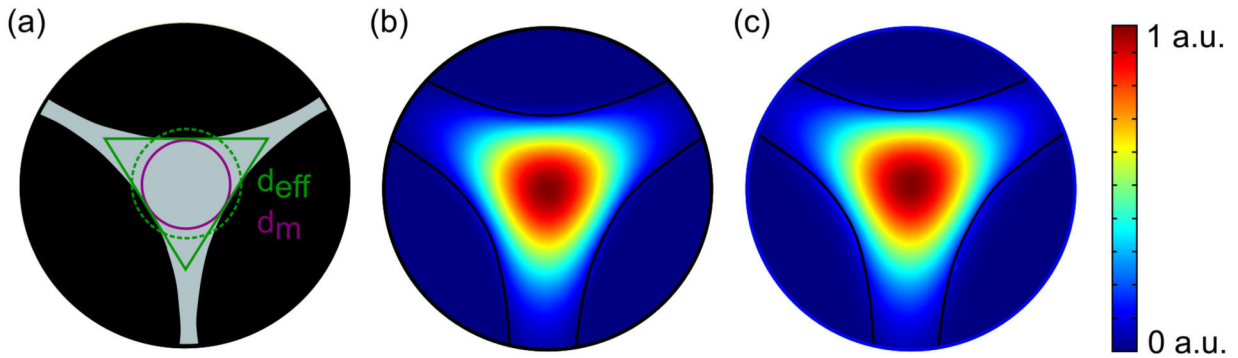


**Fig. 3.1:** (a) Measuring the MOF's core, either by the diameter of the largest inscribable circle ( $d_m$  in purple) and the circle equivalent of the area of the largest inscribable equilateral triangle ( $d_{eff}$  in green). The grey area indicates silica material with the microstructure coloured in black. (b) Electric field intensity distributions of the fundamental mode (vertically polarised case) of a 2.8  $\mu\text{m}$  diameter SC-MOF with air-filled microstructures  $n_{eff} = 1.4498$ , and (c) water-filled microstructures  $n_{eff} = 1.4556$ , calculated at 650 nm.

The precise MOF geometry can be modelled by importing scanning electron microscopy, SEM, images for the simulation. Further applying Sellmeier equation [209] and corresponding material coefficients [205,210] to the model accounts for the material dispersion, i.e. wavelength dependence of the refractive index. Fig. 3.1b,c show a select cut of the solved model area for the fundamental mode of an SEM imported COMSOL geometry in the case of air and water filled microstructures respectively.

A key parameter describing the field overlap available for sensing for a particular fibre geometry is the effective modal scattering area,  $A_{eff}$ . It is essentially defined using the power inside the guided mode, divided by its intensity at a point on the core where a nanoparticle could be immobilised, i.e.

$$A_{eff}(\vec{r}_0) = \frac{\int_{A_\infty} S_z(\vec{r}) dA}{S_z(\vec{r}_0)}, \quad (29)$$

with  $S_z(\vec{r})$  being the axial Poynting vector of the guided mode, and the NP position on the core surface ( $\vec{r}_0$ ). As such,  $A_{eff}$  is normalised in a manner not dependent on absolute modal power but is instead a specific character of the guided mode referring to its effective area at the location of the NP. It can be assumed that the modal field is not affected strongly by the NPs, which is a good approximation at low NP densities. In other words, the NP presence induces only a perturbation on the modal properties, which does not affect the field profile instead it merely adds an imaginary part to  $n_{eff}$ . Thus the bare fibre geometry without the NPs can be solved and  $A_{eff}$  calculated. This would not be the case at high NP densities since the extinction behaviour of the NPs would impact the mode profile.

The value of  $A_{eff}$  for individual fibre cores of similar geometry changes with size and material variations. A geometry suitable for sensing in this work should offer a low modal scattering area in order to sufficiently interact with the NPs on the core walls. The fundamental mode should be contained within the core with no mode leakage into

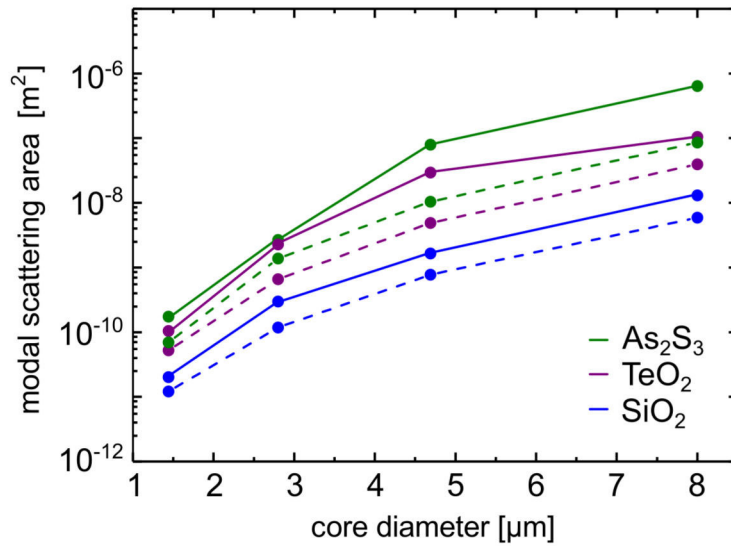


**Fig. 3.2:**  $A_{\text{eff}}$  calculated for a number of SC-MOF core sizes for the case of silica (blue), and higher RI  $\text{TeO}_2$  (purple) and  $\text{As}_2\text{S}_3$  (green) cores; surrounded by air (solid line) and water (dashed line), at a wavelength of 650 nm.

the strand regions for instance. A low  $A_{\text{eff}}$  means that a higher fraction of the fibre mode power is felt in the vicinity of the microstructure regions and is available for sensing. The value of  $A_{\text{eff}}$  for a number of SC-fibre core sizes calculated at 650 nm is shown in Fig. 3.2. The calculation shows higher  $A_{\text{eff}}$  evident at larger core diameters – a result of lower modal field penetration outside of the growing core area. This result is not conducive to a high detection signal for sensing. In contrast, the smaller core geometries investigated offer lower modal scattering area and greater channel penetration, thereby yielding a better SC-fibre sensing device. However for very small cores, the mode is less confined, the evanescent field penetrates further into the microstructures and may escape. Additionally investigated was the comparison between  $A_{\text{eff}}$  for the case of a silica core versus a higher refractive index  $\text{TeO}_2$ , and even higher,  $\text{As}_2\text{S}_3$  core. The results are again contained in Fig. 3.2. Comparing the core-cladding RI contrast between cores of the same size and different material shows the higher RI contrasts yield a higher  $A_{\text{eff}}$  – an implication of stronger field confinement in the core, and reduced microchannel interaction. Further infiltrating the microstructures with water and reducing this RI contrast means the mode is once more less confined and sees higher field penetration within the microstructures for all calculated core sizes, Fig. 3.2.

This investigation prompts the experimental implementation of a lower RI contrast core such as  $\text{SiO}_2$  and a small core diameter of 2.5–3  $\mu\text{m}$ . This selection provides the low modal scattering area required to sense in the microstructured region with sufficiently high signal intensity. Smaller core sizes than this are difficult to fabricate and either the strut thickness would become too thin and break or the strut thickness relative to core size would become similar resulting in light escaping through the struts. Even at these small core sizes the MOFs are multimode and care must be taken to excite the fundamental mode. Thus a core diameter of 2.5–3  $\mu\text{m}$  represents the optimal compromise between modal scattering area availability, structural stability, and experimental hand-

ling. A comparison of the available field intensity fractions for a range of small-core silica SC-MOFs is provided in Tab. 2 further indicating enhanced availability for sensing at lower fibre core diameters.

Table 2: **Overview** Fractions of field intensities offered by a range of small-core SiO<sub>2</sub> SC-MOFs at 650 nm with water filled microstructures. The fraction of the field intensity in water,  $f_{\text{H}_2\text{O}}$ , and SiO<sub>2</sub>,  $f_{\text{SiO}_2}$ , is given compared to the overall intensity. The intensity fraction in a 5 nm layer on the fibre core is given,  $f_l$ , as is the range for a point for horizontal and vertical polarisation at the core-water boundary relative to the centre point,  $f_b$ .

core dia.	$f_{\text{H}_2\text{O}}$	$f_{\text{SiO}_2}$	$f_l$	$f_b$
1.44 $\mu\text{m}$	$2.22 \cdot 10^{-2}$	$9.82 \cdot 10^{-1}$	$3.73 \cdot 10^{-4}$	$6.01 - 8.68 \cdot 10^{-2}$
2.80 $\mu\text{m}$	$3.68 \cdot 10^{-3}$	$9.96 \cdot 10^{-1}$	$1.28 \cdot 10^{-4}$	$1.72 - 2.73 \cdot 10^{-2}$
4.69 $\mu\text{m}$	$8.81 \cdot 10^{-4}$	$9.99 \cdot 10^{-1}$	$5.13 \cdot 10^{-5}$	$6.40 - 10.57 \cdot 10^{-3}$

### 3.2 Modal attenuation in plasmonic-photonic fibres

In order to determine the modal attenuation induced by the interaction with immobilised core wall NPs, a calculation of the fraction of power removed by a single NP (through a scattering and/or absorption event, i.e. the extincted power) from the propagating mode is required. A single NP immobilised at a position  $(x_0, y_0)$  on the core channel surface, at a propagation distance  $z$ , exacts a power change through interaction with the evanescent tail of the guided mode of

$$\frac{\Delta P(\lambda, z)}{P(\lambda, z)} = -\frac{C_{\text{ext}}}{A_{\text{eff}}(\lambda, x_0, y_0)}, \quad (30)$$

where  $C_{\text{ext}}$  is calculable through Mie theory, and  $A_{\text{eff}}$  is defined as before: essentially the fraction of the propagating guided mode power at the propagation length  $z$ , and the guided mode intensity at the nanoparticle position. Recall that this formula offers a valid approximation only when  $C_{\text{ext}} \ll A_{\text{eff}}$ . This single particle induced attenuation can then be further extended to include a number of NPs with number density,  $N$ , over a small area  $dl \times dz$  along the fibre core wall (Fig. 3.3). The power lost over this small area is then

$$\frac{\Delta P}{P} = -\frac{C_{\text{ext}}}{A_{\text{eff}}(\lambda, x_0, y_0)} dl dz N. \quad (31)$$

To further determine the attenuation over the entire transverse area of the fibre, an integral over the path  $l$  is determined for each core wall surface as

$$\frac{\Delta P}{P} = -C_{\text{ext}} N dz \int \frac{dl}{A_{\text{eff}}}, \quad (32)$$

which yields

$$\frac{\Delta P}{dz} = -P C_{\text{ext}} N \int \frac{dl}{A_{\text{eff}}}. \quad (33)$$

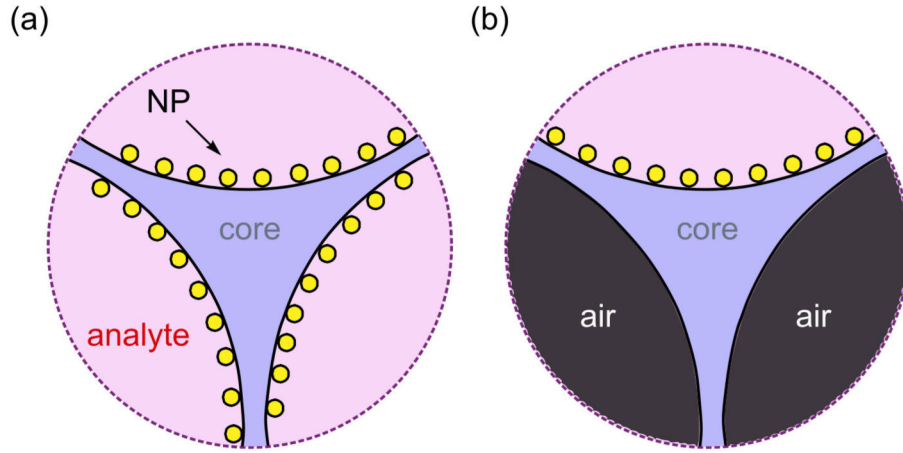


**Fig. 3.3:** Relevant NP-immobilised regions in the case of (a) SC-MOF geometry, and (b) ECF geometry, which has analyte only in the exposed channel.

From this, the attenuation,  $\gamma$ , of the guided propagating mode can be defined as [97,105, 211]

$$\gamma = NC_{\text{ext}} \int A_{\text{eff}}^{-1} dl, \quad (34)$$

which returns an expression for the output power:

$$P(z) = P(z_0)e^{-\gamma z}. \quad (35)$$

This expression is key to understanding the effect of immobilised NPs on the fibre's transmission properties, as it relates properties of the NP ( $C_{\text{ext}}$ ) to those of the fibre mode ( $A_{\text{eff}}$ ) via the capability of the measurement system  $\frac{\Delta P}{P}$ , i.e. the power detection resolution. Thus for any particular system length,  $z$ , a suitable  $\gamma$  can be targeted by the extent of the evanescent field overlap and immobilised NP density. The  $\gamma$  value should provide sufficient spectral attenuation to be readily detected but not lay below the spectrometer's detection range.

For a radially symmetric tapered fibre system (as in Sec. 3.3, [97,204]), the NP ensemble encounters the same evanescent field strength of the fundamental guided mode hence the same effective modal scattering area over the fibre surface implying:  $\int \frac{dl}{A_{\text{eff}}} = \frac{2\pi r_f}{A_{\text{eff}}(r_f)}$  where  $r_f$  is the fibre radius, yielding for radially symmetric fibres:

$$P(\lambda, z) = P_0(\lambda) \exp\left(-\frac{C_{\text{ext}}(\lambda)}{A_{\text{eff}}(\lambda, r_f)} 2\pi r_f N z\right). \quad (36)$$

To more accurately quantify the fabricated SC-fibre geometry in this study, the real fibre structure solutions are obtained from COMSOL. As mentioned the parameter  $A_{\text{eff}}$  is of particular importance for analysing NP-on-waveguide platforms, since from Eq.34 it is immediately observable that the detection of objects with small extinction cross section, or particle density, would typically also require small core sizes in order to provide sufficiently low  $A_{\text{eff}}$  values for a measurable signal. Of the studied geometries and compositions in the previous section, a small-core silica candidate that exhibited

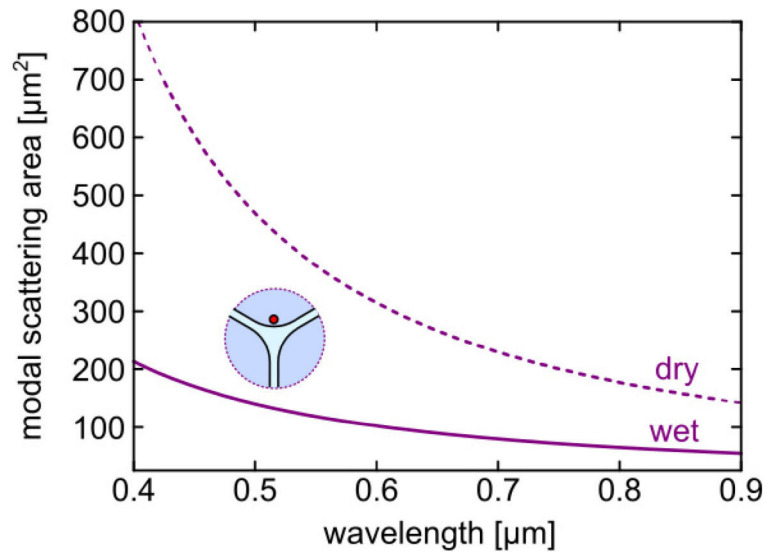


**Fig. 3.4:** Spectral behaviour of the modal scattering area,  $A_{\text{eff}}$ , for a single NP on the specified red point on the core of a 2.8  $\mu\text{m}$  diameter silica SC-MOF with air- (dashed purple line), and water-filled (solid purple line) microstructures.

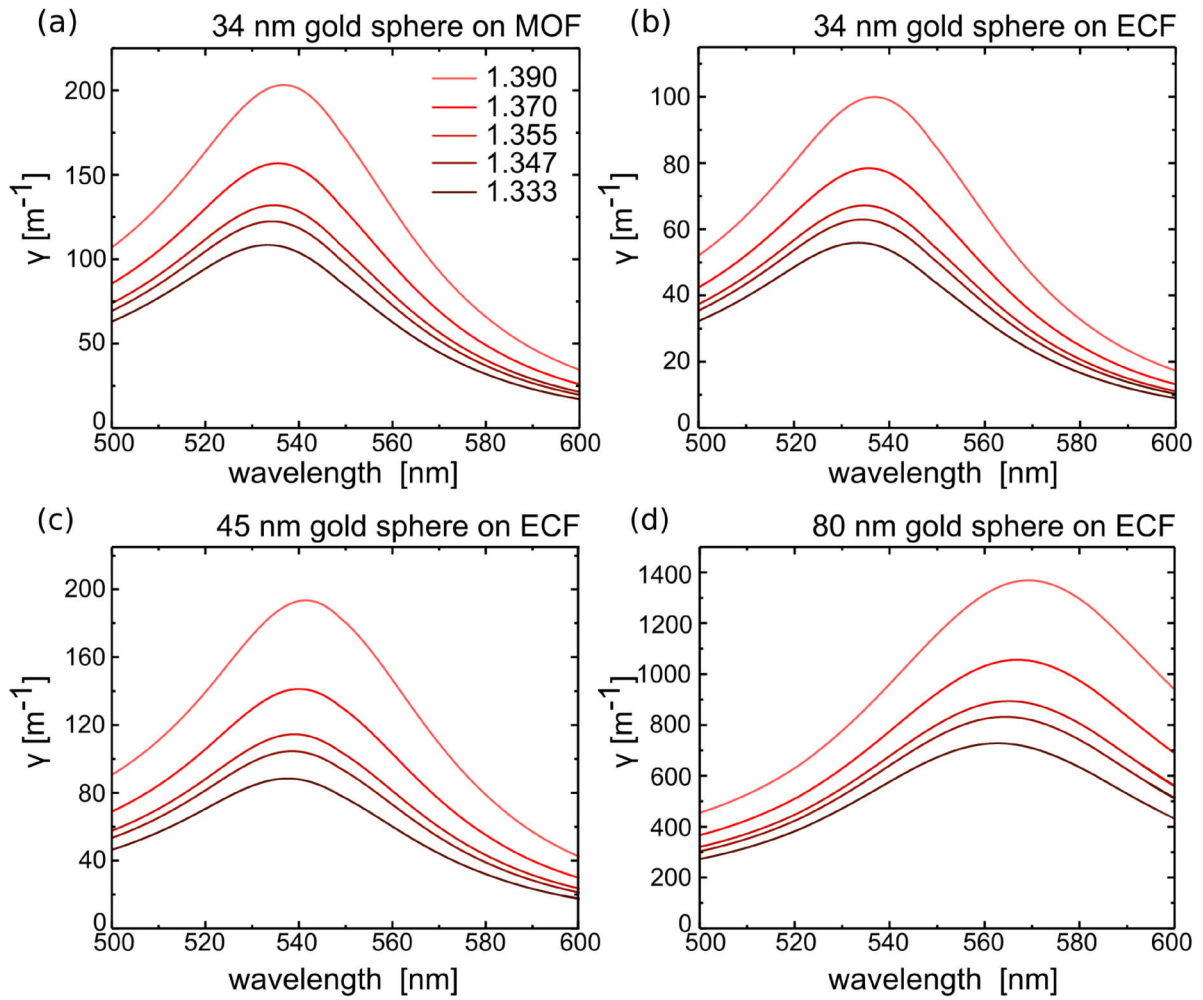
low  $A_{\text{eff}}$  was chosen as meriting investigation for further sensing investigation. A plot of the spectral wavelength dependence of  $A_{\text{eff}}$  for this 2.8  $\mu\text{m}$  diameter core SC-MOF (Fig. 3.4 dashed line) demonstrates lower  $A_{\text{eff}}$  (thereby offering higher modal attenuation) at higher wavelengths – a result of greater modal field penetration into the microchannels and analyte. This indicates longer wavelengths present an optimal operating regime for an SC-fibre sensing device. An estimation of the relative change in modal scattering area when the microstructures are infiltrated with an analyte such as water (Fig. 3.4 solid line) can be made. Since the RI contrast between core and cladding (now water – 1.333 at 575 nm, 25°C) is reduced, the mode is less confined and sees higher field penetration within the microstructures. Hence  $A_{\text{eff}}$  decreases further, while modal attenuation is increased, a variation that is more pronounced at lower wavelengths. As an example to quantify this observance, taking an off-resonance wavelength of 700 nm, a 34 nm diameter gold nanosphere on a silica MOF core (indicated by the red point in the sketch in Fig.3.4), and the parameters that accompany this:  $C_{\text{ext}}^{\text{air}} = 1.2 \cdot 10^{-5} \mu\text{m}^2$ ,  $C_{\text{ext}}^{\text{water}} = 3.8 \cdot 10^{-5} \mu\text{m}^2$ ,  $A_{\text{eff}}^{\text{water}} = 80 \mu\text{m}^2$ ,  $A_{\text{eff}}^{\text{air}} = 230 \mu\text{m}^2$ , a ratio in the modal attenuation of  $\frac{\gamma_{\text{air}}}{\gamma_{\text{water}}} \approx 0.11$  is evident. This indicates that the modal attenuation is higher for sensing in the case of an aqueous analyte by a factor of 9 compared to the case where the microstructures are filled with air ( $\gamma_{\text{water}} > \gamma_{\text{air}}$ ). NP extinction cross section increases upon introduction to a higher RI analyte (as anticipated from Mie theory in Ch. 2.2.3), whereas an increase in RI imposes a reduction in  $A_{\text{eff}}$  for the MOF. Thus an increased RI environment is beneficial from both NP and fibre perspectives; prompting larger LSPR shift from NPs, and higher evanescent field overlap in the fibre for better signal intensity.

Following the calculation of modal scattering area, the overall induced modal attenuation (Eq. 34) for the system could be predicted with the NP contribution included. For instance, a single 34 nm diameter gold nanosphere immobilised on a 2.8  $\mu\text{m}$  core diameter water filled MOF (resonant at 530 nm with an extinction cross section of:

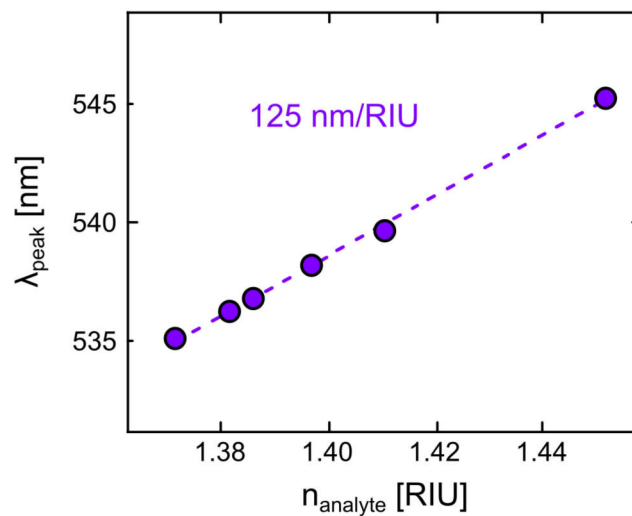
$2.54 \cdot 10^{-3} \mu\text{m}^2$ ) would extract a relatively low power fraction of  $\frac{\Delta P}{P} = 2.12 \cdot 10^{-5}$  ( $A_{\text{eff}} = 120 \mu\text{m}^2$ ). However, a considerable benefit of using a fibre optics platform comes from the collective interaction with multiple NPs all along the fibre length. The extended interaction length over an ensemble of immobilised NPs permits tailorable attenuation, thus enabling these small-core SC-fibre systems to be used as sensing platforms. To predict the sensitivity of the plasmonic fibre systems, which is essentially the NP sensitivity as discussed in Ch. 2.2.5, modal attenuation could be calculated for a particular deposition density or single NP (Fig. 3.5). A plot of such resonance wavelength positions (i.e., transmission dip or attenuation peak) versus analyte RI, yields a slope value providing sensitivity for the system (as Fig. 3.6). The sensitivities calculated directly for the systems in Fig. 3.5 are given in Tab. 3, along with those including a substrate weighting factor ( $\eta_{\text{shell}} = 0.7$ ), both of which match closely with the predicted NP sensitivities from Mie theory (as in Tab. 1). This weighting factor is calculated for a sensing distance equal to the NP radius; in reality this distance can be shorter in which case the weighting factor is reduced [148]. As an example, the sensitivity using a lower weighting factor ( $\eta_{\text{shell}} = 0.58$ ) was similarly calculated. For the case of a  $2.8 \mu\text{m}$  diameter MOF with  $34 \text{ nm}$  diameter Au NPs a sensitivity value of  $118 \text{ nm/RIU}$  was determined, for a  $2.5 \mu\text{m}$  core ECF (Fig. 3.6) with  $45 \text{ nm}$  diameter Au NPs a value of  $125 \text{ nm/RIU}$  was obtained. Taking the substrate effect and weighting factor into account yields values of  $68.44$  and  $72.27 \text{ nm/RIU}$  respectively, closely matching the theoretical NP predictions presented in Ch. 2.2.5, Tab. 1. The slightly higher sensitivity arising from a marginally larger particle size is to be expected from Mie theory. Clearly the sensitivity of the systems rests on the NP sensitivity, indicating that by later incorporating a more sensitive NP species [53] the system sensitivity can be dramatically enhanced.

Table 3: **Overview** Theoretical sensitivity of fibre systems, of core diameter  $2.8 \mu\text{m}$  and NP diameters relevant for this work, calculated based on Eq. 34.

fibre	NP dia. [nm]	theory [nm/RIU]	theory ( $\times 0.7$ ) [nm/RIU]
SC-MOF	34	84.56	59.25
ECF	34	85.62	59.99
ECF	45	96.14	66.70
ECF	80	164.83	115.34



**Fig. 3.5:** Modal attenuation change with wavelength. The microstructure RI is varied for the case of a 2.8  $\mu\text{m}$  core SC-MOF with (a) 34 nm diameter Au nanosphere, and the case of a 2.5  $\mu\text{m}$  core ECF with (b) 34 nm, (c) 45 nm, and (d) 80 nm diameter Au nanospheres.



**Fig. 3.6:** Resonance wavelength variation with RI environment for a 2.5  $\mu\text{m}$  core ECF with 45 nm Au nanospheres, yielding an RI sensitivity of 125 nm/RIU; weighting factor not included.

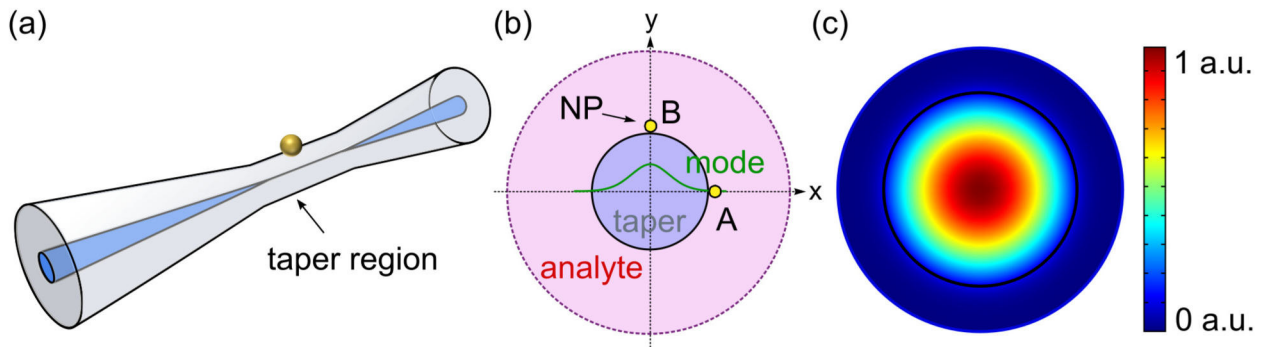


**Fig. 3.7:** (a) Schematic and (b) cross section of a fibre taper structure. (c) Enlarged simulation region showing the electric field intensity distribution of the fundamental mode in a 3.6  $\mu\text{m}$  diameter taper waist.

### 3.3 Comparison to existing taper capabilities

A suspended-core fibre closely resembles a suspended rod (or nanowire), quite similar to the waist of a fibre taper structure. At the taper waist the core size is reduced dramatically as indicated in Fig. 3.7a, and the field is guided in the cladding. Hence a silica rod is used for simulation as in Fig. 3.7b,c. Tapers are well known in the sensing community as possessing high sensitivity but are fragile to handle. The implications are that the SC-microstructured fibres can offer all the benefits of a taper but with additional mechanical stability and enabling self-contained sample flow. Finite element simulations were implemented to compare the theoretical spectral distributions of the effective modal scattering areas for the SC-fibre geometries and their corresponding taper core sizes in order to investigate this (Fig. 3.8).

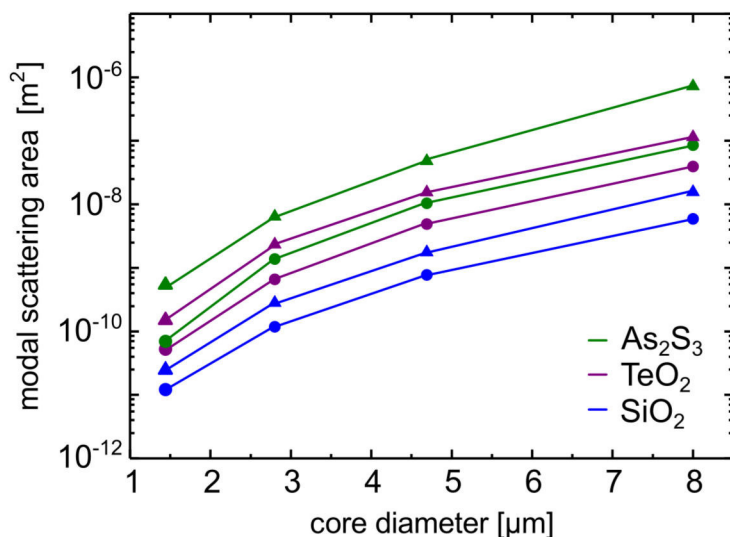


**Fig. 3.8:** Calculated values of  $A_{\text{eff}}$  for a number of taper (triangle symbols) waist and SC-MOF (circle symbols) core diameters for the case of an  $\text{SiO}_2$  (blue), and higher RI  $\text{TeO}_2$  (purple) and  $\text{As}_2\text{S}_3$  (green) cores in water.

As seen in Sec. 3.1, the suspended core shape is somewhat triangular and thus comparison of the fibre properties with a free-standing nanowire (circular) is not immediate. A straightforward solution is to determine a core diameter definition for which the fundamental mode's effective modal area best matches between both suspended and



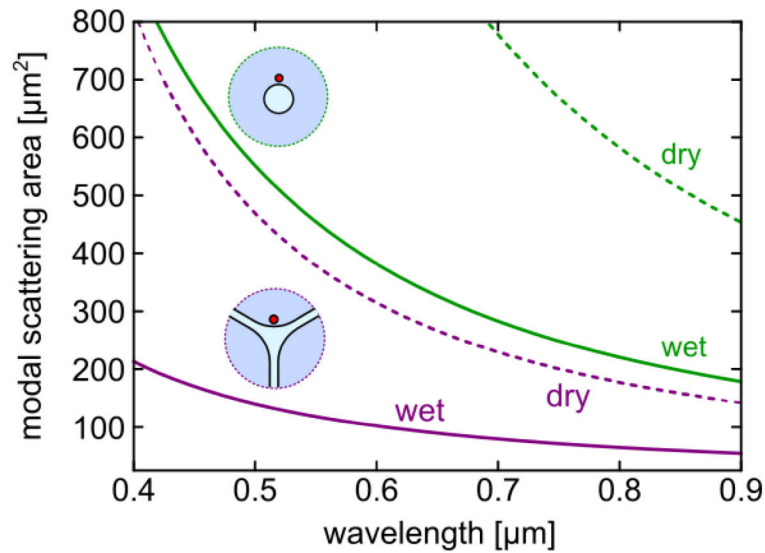


**Fig. 3.9:** Comparison of modal scattering area for the case of a 2.8  $\mu\text{m}$  silica SC-MOF (purple) and corresponding taper (green), in air (dashed lines) and water (solid lines) surroundings.

freestanding rod geometries [208]. The effective core diameter, as shown in Fig. 3.1a, is sufficient for comparison of both geometries.

The comparison of modal scattering area between the two fibre types in water shows the SC-MOF geometry consistently yielding higher values for a range of core sizes between 1.5–8  $\mu\text{m}$  in diameter (Fig. 3.8). This is due to the SC-MOF core shape enabling greater mode-channel overlap for the same modal area. Again comparing  $\text{SiO}_2$  with different higher index core materials for the taper case shows the higher RI contrasts yielding higher  $A_{\text{eff}}$ , resulting from greater modal confinement, and thereby lower modal attenuation.

A graph comparing the spectral  $A_{\text{eff}}$  behaviour of the 2.8  $\mu\text{m}$  diameter SC-MOF, which is implemented experimentally in this study, and a circular silica taper of corresponding diameter further highlights the enhanced performance of the SC-MOF (Fig. 3.9). Noteworthy is that this SC-fibre core diameter is comparatively small for typically used NP-fibre systems including tapers. The modal scattering areas for both systems in air and embedded in a water analyte medium are presented.

In order to compare quantitatively, the case of a 34 nm diameter gold NP particle located 1 nm above the silica core wall (indicated by the red dots in the sketches, Fig. 3.9) is considered at an off-resonance wavelength of 700 nm. This example was discussed previously for the SC-fibre system where the NP extinction cross section was seen to increase upon introduction to higher refractive index analyte, and the value of  $A_{\text{eff}}$  decreased – dramatically at shorter wavelengths. The taper diameter shows similar behaviour upon analyte change to water with a 2.75 times decrease in  $A_{\text{eff}}$ . Comparing the values obtained from both analyte infiltrated systems, an effective modal scattering area is observed that is lower by a factor of 3.5 for the SC-MOF case. This greatly emphasises the excellent sensing potential performance of SC-fibres and incites their use as a platform towards detecting very small metallic nanoparticles.

### 3.4 Additional approaches

While the highlighted analytical approach is considered to give a solid impression of what to expect from NP-immobilised SCF sensing capabilities, some other factors can be considered in the simulation:

1. A Maxwell-Garnett (MG) Effective Media Approximation (EMA) for a NP inclusion layer on the core wall can be implemented during simulation or to replace the COMSOL simulation. Such a model provides an effective permittivity layer with spherical inclusions for calculating the attenuation from different NP inclusion densities [212,213]. It assumes negligible interaction between NPs and is valid at lower volume fractions of NPs. The Maxwell-Garnett theory starts from the macroscopic Maxwell's equations, (assumed valid on a fine scale within the composite) and from the weighted sum of polarisabilities of all components calculated via the Clausius-Mossotti expression derives an expression containing the effective permittivity,  $\epsilon_{MG}$ :

$$\frac{\epsilon_{MG} - \epsilon_h}{\epsilon_{MG} + 2\epsilon_h} = f \frac{\epsilon_{NP} - \epsilon_h}{\epsilon_{NP} + 2\epsilon_h} . \quad (37)$$

$\epsilon_h$  represents the permittivity of the host matrix,  $\epsilon_{NP}$  that of the NP inclusions, and  $f$  the volume fraction of inclusions. Implementing the Maxwell-Garnett approximation with different NP densities allows a fast indication of the attenuation absorption spectrum. This can also be applied in COMSOL on the ECF in conjunction with Eq. 34 and using  $C_{sca}$  to yield a system attenuation.

2. While an effective substrate surrounding (as outlined in Ch. 2.2.4), was considered in calculations, the effect of the chemical deposition modifications (aminosilane or polyelectrolyte surface modification) and distance to the NP ( $\sim 0.154$  nm) was not. This was considered to play a negligible role and be unnecessary in the theoretical modal attenuation determination.
3. The exposed channel of the ECF during fabrication induces an asymmetry in the fibre core, which in turn creates a birefringence. This effect becomes more pronounced when an analyte is introduced to the open channel since the refractive index profile becomes particularly asymmetric. The fibre structure and resulting birefringence can be investigated using finite-element method (COMSOL) with the exposed channel filled with water (biologically relevant sensing analyte) and the closed channels with air (as in Fig. 3.10a). Electric field intensity distributions for the horizontal (x) and vertical (y) polarised fundamental modes are output (Fig. 3.10b,c respectively showing a select area of the simulation geometry). By comparing the resulting effective refractive indices of these modes the birefringence for a  $2.8 \mu\text{m}$  diameter ECF at  $650 \text{ nm}$  can be determined:  $B = |n_x - n_y| = 6.867 \cdot 10^{-5}$ , where  $n_x$  and  $n_y$  are the effective refractive indices of the x- and y-polarised modes

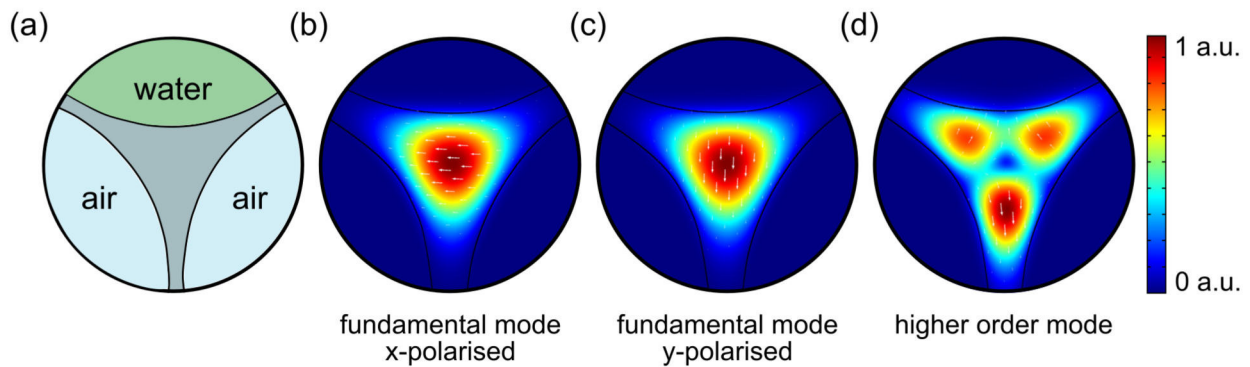


**Fig. 3.10:** (a) Schematic of an ECF of core diameter 2.8 μm with two air-filled and a water-filled channel. Finite element simulations (COMSOL) were conducted to calculate intensity and polarisation profiles for (b) the fundamental optical mode with horizontal polarisation,  $n_{\text{eff}} = 1.4497$ , (c) with vertical polarisation,  $n_{\text{eff}} = 1.4498$ , and (d) the first higher order mode,  $n_{\text{eff}} = 1.4421$ . Black lines indicate the core structure. The simulation sections shown have been cut to display the area of interest.

respectively. Both polarisation modes will therefore have different propagating mode field overlap in the open core channel and thus offer different relative sensitivities to changing external RI environment; although this was found to be negligible in this system. The birefringence itself should increase with bulk RI of the exposed channel, as the rate of increase of  $n_{\text{eff}}$  of the x-polarisation mode exceeds that of the y-polarisation mode. For local thin film deposition in air this behaviour can vary [214].

### Chapter summary

- An analytical model is introduced and combined with simulation to determine the NP induced modal loss.
- An important parameter for sensing is the modal attenuation,  $A_{\text{eff}}$ , describing the amount of the total field experienced by a NP immobilised on the core wall. A range of core sizes and materials were explored to obtain a structure presenting a low value of  $A_{\text{eff}}$ .
- The detection of objects with small  $C_{\text{ext}}$ , or low particle density, requires small core sizes in order to provide sufficiently low  $A_{\text{eff}}$  values for a measurable signal.
- Calculations indicate that a small-core ECF or SC-MOF geometry can offer adequate modal attenuation, based on an array of NPs, for plasmonic sensing.
- These small-core MOF systems can outperform a correspondingly sized taper waist in terms of lower modal scattering efficiency, for instance by a factor of 3.5 at 700 nm.

Whilst non-bonded nanoparticle filling of microstructured fibres can be as simple as utilising capillary force, the focus of this work was to physically attach the NPs along the walls of the microstructured channels. This immobilisation would render the system reusable, prevent later agglomeration, and allow for the highest possible overlap between the evanescent field from the guided mode and the plasmonic region.

A prevalent challenge with incorporating metallic thin films or NPs within MOFs is avoiding damage to the thin struts and core structure along the fibre length. The non-perfect circular microstructures and the channel curvature itself can also prove problematic for homogeneous coverage. In recent years the trend has been towards high-pressure chemical deposition techniques, for instance, chemical vapour deposition, CVD [215]. Along with a high pressure, heat treatments are also required which can damage the fibre coating and mechanical stability. Layer lengths are limited, as is the homogeneity, due to coverage gradients induced by particle depletion. Static deposition procedures have also been attempted [216, 217], for example the in situ synthesis of silver nanoparticles. Such procedures however result in relatively rough surface layers of non-adjustable thickness.

In general, the deposition of long MOF lengths must necessarily be performed at room temperature with homogeneous, adjustable, NP coverage density. This work incorporates a dynamic low-pressure, chemical deposition of the metallic nanoparticles, which are immobilised in a self-assembled monolayer (SAM) within the inner channel surfaces of the SC-MOF. The Nanoparticle Layer Deposition (NLD) technique implemented in this chapter is based on oxide surface SAM techniques [218, 219], using silane chemistry and controlled microfluidics, and can be employed for a variety of metal nanoparticle types. In such a manner, an even NP deposition is feasible without the threat of damaging the thin struts or core of the SC-MOF. For the ECF counterpart the microstructure area is open and an alternative deposition strategy is required in the form of electrostatic polyelectrolyte layers.

This chapter presents the creation of a plasmonic SC-MOF and ECF, combining fibre and NP fabrication and deposition elements. Each of the steps undertaken for the creation of homogeneous layers of immobilised NPs of controllable density is demonstrated. In particular, the NLD approach yields layer homogeneity over metres of length, which are also invariant on channel curvature. The findings of this chapter have been partly published in the scope of this thesis.

#### 4.1 MOF platform

The fibre candidates presented in this thesis were chosen for availability and their small core, thin strut geometry leading to favourable sensing capabilities as outlined in Ch. 3. Both fibres offer straightforward microfluidic access for deposition and analyte sensing application through their large or exposed microstructures. This investigation was fo-

cussed on the initial longitudinal optical characterisation of plasmonic MOF fibre sensors and the fibre channels were functionalised homogeneously with the same particle types. Following the success of this work, both fibres appear highly promising for subsequent studies. For instance the strut separated channels offered by the SC-MOF geometry have the potential for multiplexed biosensing, by immobilising each channel with a different nanoparticle species or functionalisation. Furthermore, the exposed-core channel of the ECF geometry would allow for distributed sensing and functionalisation at different sections along the fibre length.

### SC-MOF fabrication

The small-core SC-MOF geometries implemented in this study (Fig. 4.1) were fabricated in-house by the “stack and draw” method, from high purity silica preforms. The use of silica material, yields a fibre possessing higher thermal resistance and lower material losses than, for instance, that of a polymer fibre. This is a commonly implemented concept which is generally used for MOF fabrication [220, 221]. The method involves stacking individual, macroscopic, high purity silica glass capillary tubes together inside a glass casing pipe to form a preform (which possesses approximately the resulting fibre geometry), and then to “draw” or pull this preform (under temperatures near the softening point of the glass preform), on a drawing tower, into a fibre possessing micron scale structure. By applying a high over-pressure, the initial capillary tubes are prevented from collapsing. Subsequently, the drawn fibre can be treated with a polymer coating to add resistance to fracturing for instance.

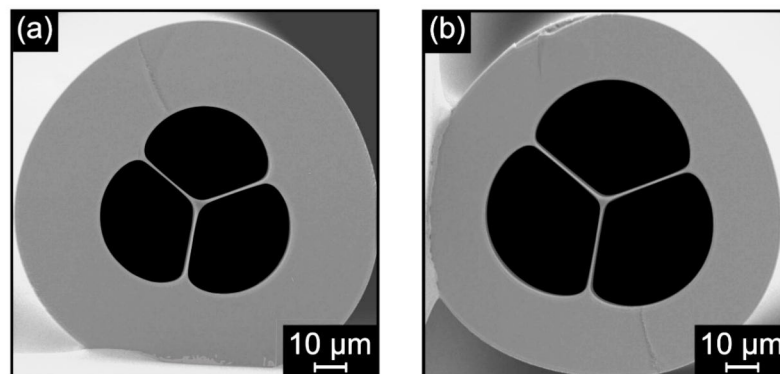


**Fig. 4.1:** SEM imaging showing two end facets of the implemented tri-channel SC-MOF geometry. (a) SC-MOF with small core ( $4.25\ \mu\text{m}$  diameter) and microstructures, and thicker cladding. (b) A similar SC-MOF ( $2.80\ \mu\text{m}$  core diameter) with larger microstructures and thinner cladding.

### SC-MOF characterisation

For the tri-hole SC-MOF (Fig. 4.1), the channel diameters are measured by that of the largest inscribable circle or by measuring the width and height individually. The core diameter can be evaluated either by the largest inscribable circle within the core, or as in Ch. 3 by taking the diameter of the circle whose area corresponds to that of the largest equilateral triangle which fits entirely within the core region [97, 106, 107]. The

SC-MOF presented here for deposition possesses a core diameter of  $2.8\ \mu\text{m}$ , channel dimensions of  $30 \times 40\ \mu\text{m}$ , strut thickness of  $500\ \text{nm}$ , and an outer fibre diameter of  $125\ \mu\text{m}$  (all discernible by means of SEM imaging). The large, microstructured inner channel diameters enable both ease of access for microfluidic filling, and the deposition of longer fibre lengths (over metres) [127].

### ECF fabrication

The second microstructured fibre geometry applied in this work was the exposed-core fibre, ECF. This fabrication was undertaken by collaborators (E. Schartner, Institute for Photonics and Advanced Sensing and School of Physical Sciences, University of Adelaide, Australia) specialising in ultrasonic fibre drilling and ECF fabrication. The ECF lengths involved in this work were fabricated by means of a two-step process which involved caning the preform, and then inserting that cane into a drilled slotted silica rod. Initially an ultrasonic mill is used to drill the three microstructured channels into fused silica rods and again to cut open one of those channels to form the exposed channel (Fig. 4.2a,b). The preform undergoes cleaning steps to reduce drilling contaminants before being caned down to a smaller diameter. The cane is then inserted into a slotted jacket and drawn into fibre. Specific details of the fabrication steps have been reported previously [207, 222].

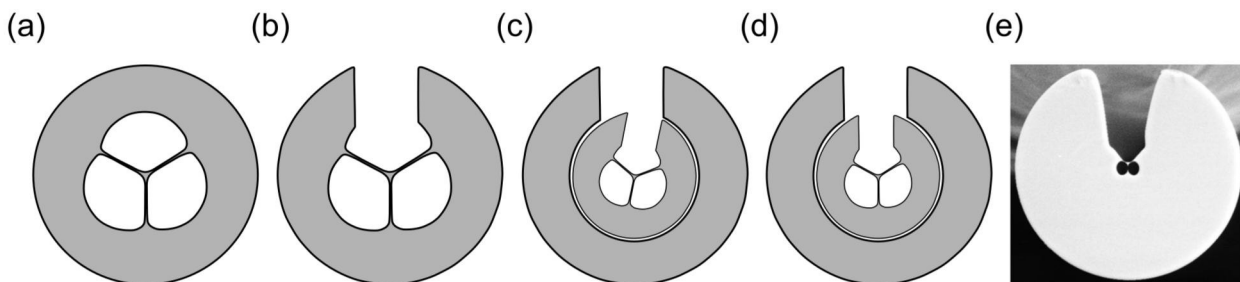


**Fig. 4.2:** The ECF fabrication process involving (a) a typical SC-MOF geometry, (b) an ultrasonically drilled open channel, and (c) alignment within a larger open cladding, either tilted to retain some protection or entirely exposed as in (d). The fibres are then drawn into the final structures (e).

### ECF characterisation

ECFs retain the geometry of the previously described tri-channel SC-MOF but with one channel open or “exposed” to the environment. The ECF presented for deposition here, is essentially comprised of two enclosed “pie-slice shape” inner channels (diameters of approximately  $15\ \mu\text{m}$  and  $17\ \mu\text{m}$ ) separated by struts of thickness  $100\text{--}200\ \text{nm}$ , and one open exposed channel. The silica core is again triangular type and of diameter  $2.5\ \mu\text{m}$ , measured as for the SC-MOF, the resulting exposed strut–core–strut “valley” width is  $30\ \mu\text{m}$ . The valley depth,  $80\ \mu\text{m}$ , offers some protection from environmental contamination in comparison to the core being closer to the outer cladding extremities. This depth also acts to contain the analytes. Additionally, the direct orientation of the core offers better deposition access than for the case of a rotated orientation (Fig. 4.2c-e).

## 4.2 Fabrication and characterisation of nanoparticles

As a consequence of the morphological effect of NPs on light interaction and LSPR, substantial work has been undertaken to develop fabrication methods for the high-quality production of various plasmonic NP geometries. In this investigation, 34–45 nm gold spheres exhibiting LSPR at 528–534 nm in solution were targeted for synthesis, more exotic NPs require more involved fabrication and can be done in-house (Nanobiophotonics group, IPHT) or ordered from specialist companies (Nanocomposix, BBI solutions, etc). In the instances where Au nanospheres were not available in-house they were fabricated in the course of this study.

One of the most reliable, straightforward, NP synthesis techniques is the wet chemical process created in 1951 by Turkevich [223] and further refined in the 1970s by Frens [224]. It is widely implemented for synthesising monodisperse gold nanospheres with diameters in the range of 5–120 nm. As NP sizes increase further however, there is a tendency for elliptical shape formation, yielding polydisperse particles [225].

### 4.2.1 Gold nanosphere synthesis

Particle batches were synthesised by the citrate reduction of gold chloride  $\text{HAuCl}_4$  in water, i.e., the Turkevich-Frens method, yielding charge stabilised Au nanospheres whose size is tunable by adjustment of the molar (citrate ion ( $\text{C}_6\text{H}_5\text{O}_7^{3-}$ ) to gold chloride ( $\text{HAuCl}_4$ )) ratio, here: 0.55. To achieve this, an Au III chloride salt seed solution (56.39 mg in 6.53 ml three-times-distilled, 3d,  $\text{H}_2\text{O}$ ; light and air sensitive), and a reducing agent solution, here trisodiumcitrate dihydrate (TSC, from Sigma Aldrich, 8.24 mg in 49.68 ml 3d  $\text{H}_2\text{O}$ ), were both prepared. As TSC is a relatively weak reducing agent the solution was boiled to achieve the kinetic energy necessary for the reaction. Thus a solution of 24.75 ml of the TSC (0.564 mM) with 74.25 ml 3d  $\text{H}_2\text{O}$  (99 ml solution in total) was heated, with stirring, in a three-neck distilling flask for 20 minutes before the addition of 1 ml of the Au seed solution. This was further boiled for an hour (dependent on the molar ratio implemented). Typically, a lower reductant to metal salt ratio yields the slow formation of a small quantity of larger NPs, of greater size heterogeneity, compared to the higher ratio case which incites the rapid formation of a higher number of smaller, monodisperse particles. Studies have demonstrated that the addition of the Au seed to the citrate (rather than the reverse case) results in smaller NPs of narrower size distribution [226]. Therefore the temperature (reaction kinetics) and concentration of precursors should be precisely regulated to achieve fabrication of a specific NP size. The occurrence of nucleation was observable through colour change of the solution to faint blue. As spherical particles were formed, the colour further developed into a dark purple-black and then to dark red. A full colour transition from purple-black to light red indicated the completion of the reduction process – the metal ions were consumed. Studies on the shape-evolution of spherical gold NPs synthesised by this technique note that the colour transition (purple-black) can be explained by a gold nanowire intermediate phase [227].

This solution was then cooled, filtered (eradicating particulates  $> 0.22 \mu\text{m}$  in size), and stored in the fridge with refiltering before use.

The resulting NPs are charge stabilised due to citrate residues from the synthesis, they thereby repel one another and remain stable in colloidal form which removes any capping agent requirements. These electrostatic surface charges ( $-30 \text{ mV}$ ) have further benefit, for instance, as a medium of attraction during deposition as outlined in Sec. 4.3.2, or for conjugation to antibodies [228]. Proceeding from synthesis, each batch of NPs must be initially characterised before immobilisation within the MOF microstructures.

#### 4.2.2 Gold nanosphere characterisation – quality control

Post-synthesis several characterisation methods may be employed including: Transmission Electron Microscopy (TEM), Atomic Force Microscopy (AFM), Scanning Electron Microscopy (SEM), and X-Ray Diffraction to image size, shape, and structure of the synthesised particles.

UV-VIS spectrophotometry was employed to evaluate the light intensity ratio through a NP solution sample compared to unobstructed incident light (Fig. 4.3). UV-VIS spectrophotometry enables optical property (absorption, scattering, extinction) analysis of the NP solution and combined with Beer-Lambert's law can determine the concentration,  $c$ , of a sample (where  $L$  is the propagation distance through a sample):  $A = \log_{10}(I_0/I)\epsilon cL$ . Particle size distribution is also mirrored in the spectrum and can be estimated by determining the spectral resonance peak position from UV-VIS measurement, and comparing this to calibration fits or to Mie theory. Thus an initial insight into size quality of the synthesised solution can be achieved before further analysis such as TEM (Fig. 4.3 inset), where the NPs can be individually measured.

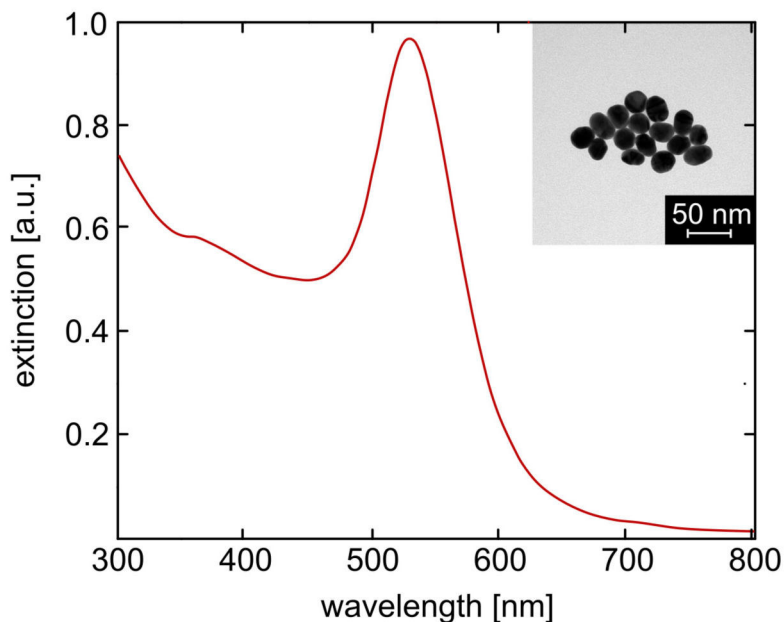


**Fig. 4.3:** UV-VIS spectrum of colloidal NPs with  $\lambda_{\text{peak}}$  at 528 nm indicating a diameter size of 34 nm. TEM imaging of the NPs, as inset, enables measurement of the size distribution, e.g. via Image J. Individual NP sizing (ideally for a set  $N > 200$ ) allows a precise statistical measure of size distribution; for this particle batch:  $34.4 \pm 3.6 \text{ nm}$ .



### 4.3 Incorporation of gold nanospheres in-/on-fibre

A number of deposition techniques were investigated in this work. Among the most successful was a wet chemical aminosilane-instigated nanoparticle layer deposition (NLD) method (designed by [126]) and a polyelectrolyte layer-by-layer technique. Both of these deposition methods yielded homogeneous NP-immobilised surfaces.

#### 4.3.1 Aminosilane modification

The first SC-MOF functionalisation approach consisted of a dynamic low pressure ‘nanoparticle layer deposition’ (NLD) method (designed by [126]), whereby nanoparticles are chemically immobilised to the interior silica channel walls of a MOF in a self-assembled monolayer (SAM) (Fig. 4.4). The deposition is carried out microfluidically (Fig. 4.5) and a microfluidic chip can be implemented for depositions greater than 6 m. This technique yielded well-defined nanoparticle layers, homogeneous over meters of length, without strut damage. Simply by altering the density of amino-binding sites within each MOF sample, various coverage densities of NPs can be immobilised – allowing tailoring of NP density within a sample.

In preparation for the analyte infiltration of the fibre, a cleaved SC-MOF was threaded through a conventional fluidic adapter and graphite ferrule. The fibre facets were dipped in isopropanol to avoid any remaining cleave residue, residual static charge, or air bubbles during the deposition process. The end facet quality was checked under microscope after insertion through the adapter and ferrule, as good starting conditions prevent later coverage problems. The SC-MOF adapter was then connected to tygon feeding tubes (of internal diameter 1.52 mm, and wall thickness 0.86 mm) and to a peristaltic pump (Ismatec) for analyte delivery. The delivery flow rate, depending on fibre length, was in the range of 1  $\mu\text{l}/\text{min}$ .

The NLD process consists of an initial silica surface activation (creating  $-\text{OH}$  hydroxyl group sites at the silica surface for silane bonding) followed by incubation with a ratio

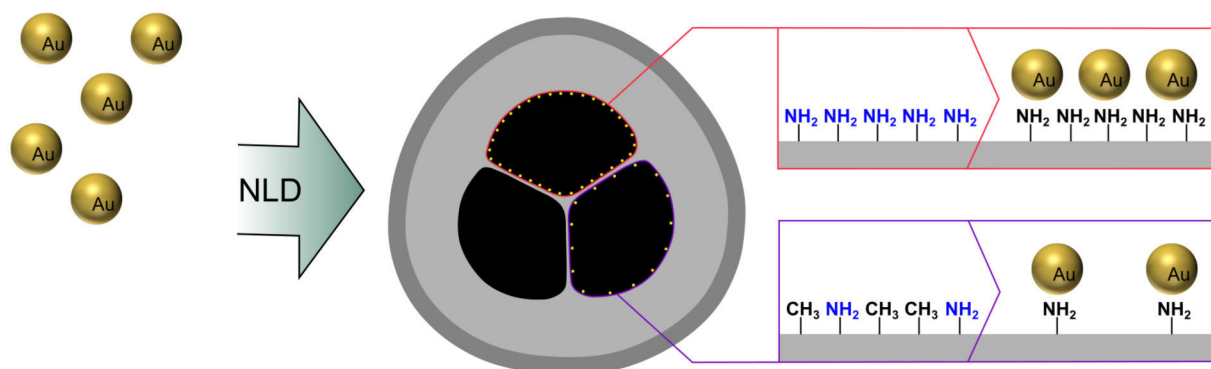


**Fig. 4.4:** NLD approach applied to SC-MOFs. NPs are immobilised wet chemically within the microstructures with a tailorable deposition density; determined by the ratio of incorporated binding silanes on the silica surface. The red lined microstructure indicates a purely bonding silane layer and full NP coverage. The purple lined microstructure additionally contains non-bonding silane and thus shows reduced deposition density.

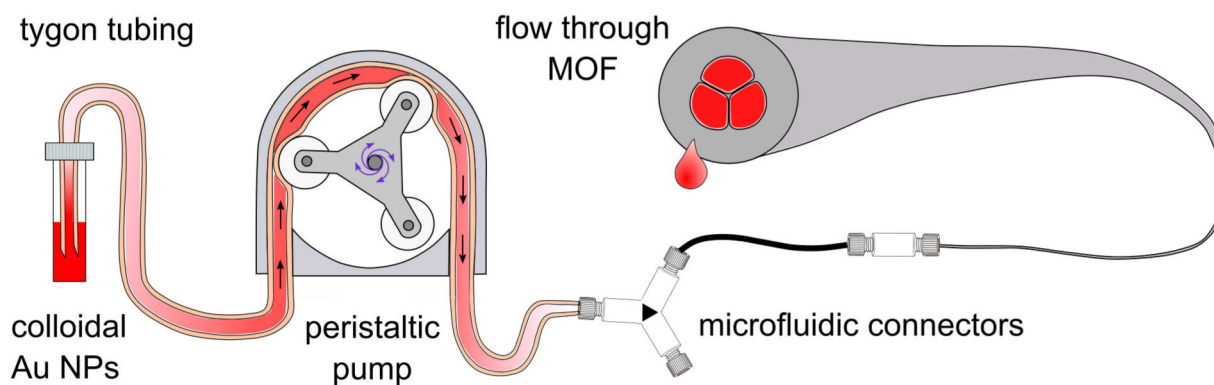


**Fig. 4.5:** NLD fabrication setup. The SC-MOF is infiltrated using a peristaltic pump and suitable microfluidic tubing and connections. The progress of NP immobilisation can be visually monitored – when all binding sites within the SC-MOF have been consumed, the output analyte will turn the same shade of red typical to the input solution (colloidal Au).

of aminosilanes that provide binding sites, in the form of free amine groups, for gold nanoparticle attachment. Unless otherwise stated, three-times-distilled (3d)  $\text{H}_2\text{O}$  is used throughout this work.

The deposition protocol is summarised in the following steps:

1. Washing the fibre with water to clean any fabrication residuals: 20 min
2. Activating the silica surface with  $\text{H}_2\text{O} + \text{ccH}_2\text{O}_2 + \text{ccHCl}$  (1 : 1 : 1 ratio), cc indicates highly concentrated. This creates an  $-\text{OH}$  group at the Si surface: > 20 min after chlorine odour occurs at fibre output
3. Washing with water: 10 min
4. Silanisation – preparation of a solution of 80 ml EtOH (Merck pure EtOH for molecular biology – less cationic interference) + 80  $\mu\text{l}$  1M (glacial) acetic acid ( $\text{CH}_3\text{-COOH}$ ) + 800  $\mu\text{l}$  silane solution (under argon environment as reactive in oxygen). The “bonding” silane ((3-aminopropyl)triethoxysilane, APTES,  $\geq 98\%$  pure, Sigma-Aldrich GmbH) for gold nanoparticle immobilisation is amphiphilic and possesses an amine functional group that the “non-bonding” silane (n-propyltriethoxysilane, PROSI,  $\geq 98\%$  pure, Sigma-Aldrich GmbH) lacks (Fig. 4.6). Gold has a particularly strong affinity for this amino group as discussed in Ch. 2.4. Thus altering the ratio of APTES/PROSI used, in turn provides access to tailorable nanoparticle coverage densities. For a mixed ratio silane deposition EtOH is used during the silanisation step due to the hydrophobicity of the PROSI silane; for a pure APTES deposition this is replaced with  $\text{H}_2\text{O}$ .
5. Hydrolysis of the silane solution (prior to fibre filling) by mixing whilst ensuring no turbidity: 10 min
6. Incubation with silane mixture, enabling covalent bond formation to the interior fibre surface by condensation reaction, and with neighbouring silanes via Van der Waals forces: approx. 1 h

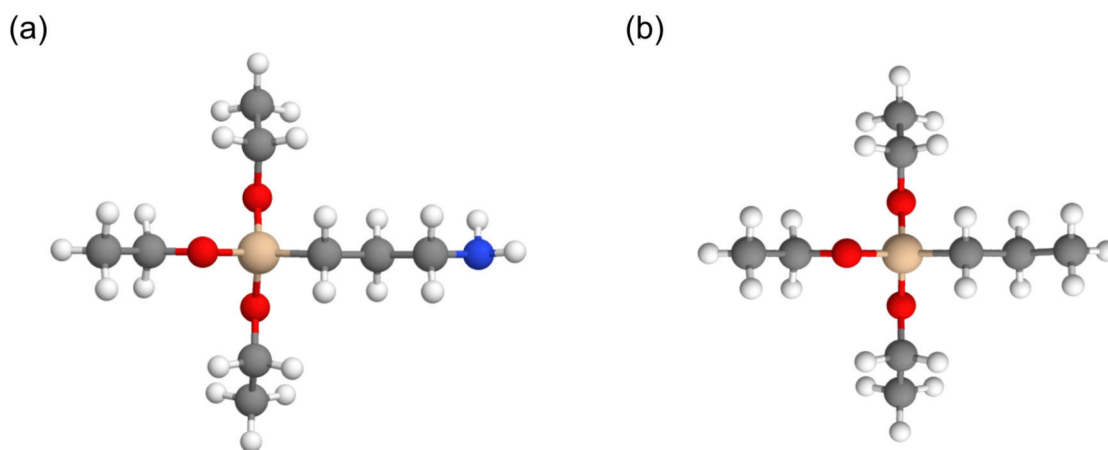


**Fig. 4.6:** Silane ball-and-stick models with light brown colour indicating an atom of Si, red-O, grey-C, and white-H, for (a) binding (3-aminopropyl)triethoxysilane, APTES, with amino functional tail group (N in blue) promoting binding to Au NPs, and (b) nonbinding n-propyltriethoxysilane, PROSI, lacking a gold affinity tail group. The effect of this functional group is shown in Fig. 4.4.

7. Washing with water: 10 min
8. Exchanging microfluidic tubing; repeated washing : 10 min
9. Nanoparticle immobilisation – NP solution is introduced into the fibre. The time duration is dependent on particle species, flow rate, fibre channel dimensions, and the silane ratio used. Generally 1.5 m of fibre was deposited, requiring 3–6 hours.

Since colloidal NP suspension possesses a particular colour depending on size, shape, material, and other properties of the NPs, the NP immobilisation step can be monitored by visual observation. In the case of 34 nm Au nanospheres the suspension exhibits a light red colour. A NP solution flowing out of the fibre end facet that is depleted of NPs appears colourless.

Once all of the aminosilane binding sites within the fibre are occupied (recall this is not a one to one ratio), the expelled solution regains colour, indicating the presence of NPs passing through the fibre (see Fig. 4.5). Throughout the immobilisation process, the microfluidic tubes are monitored for colour changes indicating agglomeration of particles, which could infiltrate the fibre and negatively impact the deposition. After deposition, both ends of the fibre should appear (under visual or microscopic inspection) coloured with the same intensity (indicating a uniform coverage density of particles). Finally, the plasmonic SC-MOF is flushed with water and dried. The targeted and resulting system, along with an example of the homogeneous NP-immobilised layer, is shown in Fig. 4.7. The fibre is stored for 24 hours in a climate chamber at 0% humidity and normal room temperature before characterisation (Fig. 4.7b,c and Sec. 4.4).

#### 4.3.1.1 Aminosilane vapour phase deposition

The ECF offers the ability to perform vapour phase silanisation deposition in the exposed channel using the same aminosilane layer as in the NLD technique. This same approach can be used to uniformly deposit taper exteriors [97].

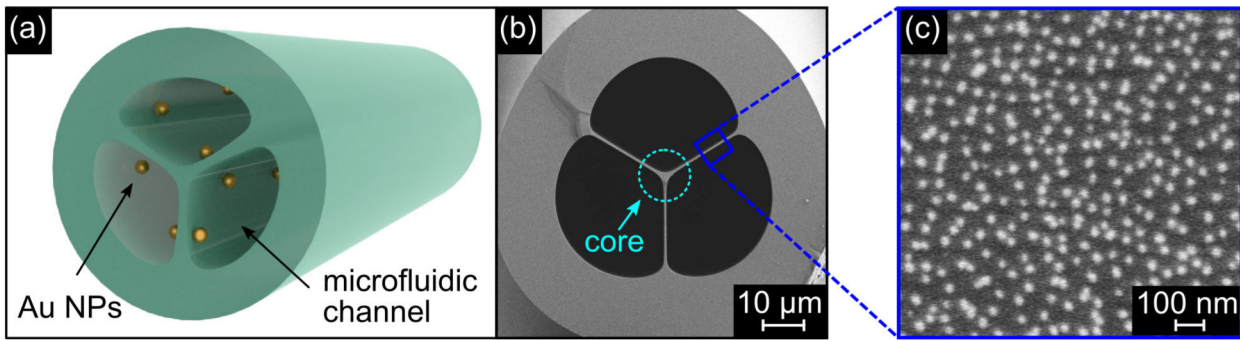


**Fig. 4.7:** (a) Rendered image of Au NPs in SC-MOF channels. (b) SEM of post-deposition SC-MOF structure. The blue box region is enlarged in (c) showing the realised NP deposition.

The deposition area of interest was submerged in a solution of  $\text{H}_2\text{O} + \text{ccH}_2\text{O}_2 + \text{ccHCl}$  (1:1:1 ratio) for a minimum of 20 minutes after the chlorine odour, to again create hydroxyl groups on the silica surface for binding the silanes. Alternatively a piranha solution can be used (e.g. 4:1 mixture of 96% concentrated sulfuric acid and 30% hydrogen peroxide as in [97]) for 30 minutes. This approach involves more physical handling than NLD, as at this point the ECF is rinsed and stored under 3d  $\text{H}_2\text{O}$  until silanisation is conducted.

For vapour phase silanisation the binding silane, APTES, can be used to provide the amine groups for nanoparticle immobilisation. This is undertaken within a sealable aluminium reaction chamber (3.6 l volume), in a  $90^\circ\text{C}$  furnace. The chamber is preheated to  $120^\circ\text{C}$ , before addition of fibre samples, to remove any adsorbed water from the inner chamber walls. The ECF samples are then mounted exposed side up in a holder inside the chamber. The chamber size automatically limited the deposition lengths for this process. The chamber is flooded with argon and 500  $\mu\text{l}$  of APTES injected onto a petri dish within the chamber through a screw cap port on the chamber. This provides a saturated APTES atmosphere in the chamber of approximately 8 mbar vapour pressure.

The ECF samples are incubated for 2 hours, after which the chamber is removed from the furnace, argon-purged, and the fibres can be removed and immediately submerged in nanoparticle solution using a polytetrafluoroethylene (PTFE) liquid cell (400  $\mu\text{l}$  volume). Various NP densities can be targeted by submerging in a stock solution dilution series or by varying the submergence time. Internal, non-exposed channel immobilisation by this approach is untested; it was unclear how far into a microstructure the vapour would uniformly infiltrate. Thus in order to prevent any NPs bonding in the closed channels after silanisation the channels were UV glued closed under microscope before silanisation.

The quality of the silanisation procedure can be checked by the static contact angle formed by a water droplet on treated silica substrate. Post-silanisation the droplet's contact angle should increase from  $< 10^\circ$  (after surface activation) to  $57^\circ$  [97]. The homogeneity of the resulting NP layer was tested on planar substrate before applying the technique to the ECF (characterised in Sec.4.4, and Fig. 4.14).

While vapour phase deposition did provide a workaround for infiltrating the exposed channel with binding silanes, additional fibre handling and manual rinsing and dipping steps were involved. The resulting channel deposition was not as uniform as NLD-in-

MOF, with NP gradients on the channel curvature and some NP clustering (as shown later in Sec. 4.4, Fig. 4.14). This may be due to the reduced efficiency of post-silanisation solutions as compared to the continuous flow NLD technique. Overall, this deposition and characterisation process was found to require greater time than desired. A more straightforward, less time consuming approach that could potentially be conducted in situ in a transmission setup was preferable. Hence polyelectrolyte layers were investigated.

#### 4.3.2 Layer-by-layer polyelectrolyte deposition

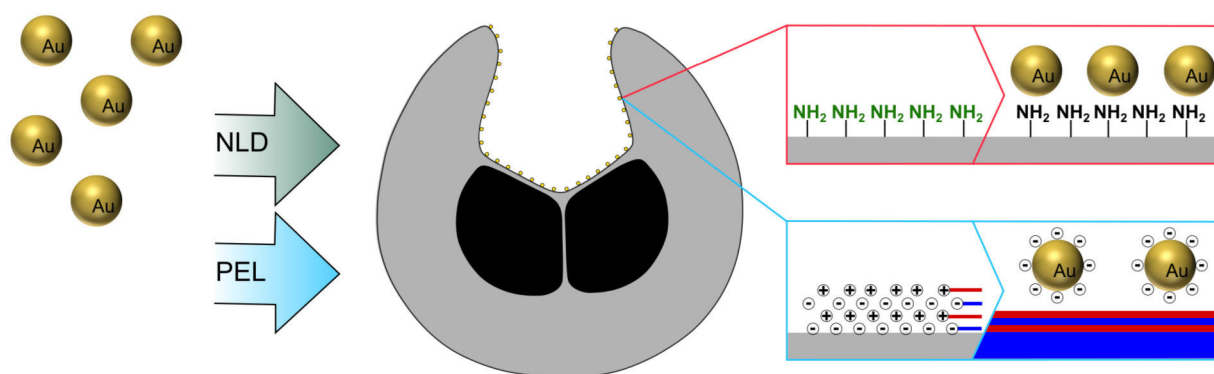


**Fig. 4.8:** ECF deposition approaches include vapour-phase NLD or a Layer-by-Layer (LbL) polyelectrolyte (PE) technique. The LbL approach involves stacking layers of alternating charged PEs within the exposed-core channel, and bonding NPs via residual charges.

Since the ECF by definition offers direct access to the core region, NP deposition can be achieved directly on the core (Fig. 4.8), potentially along specific positions and lengths. The low channel volume also enables rapid analyte exchange and improved response time. Additionally, NP deposition on only one side of the core, as opposed to all three channels of the SC-MOF, would significantly reduce loss. To achieve this, a direct immobilisation was investigated, in situ, using polyelectrolyte (PE) charged layer deposition.

Nanometre-thin polyelectrolyte layers (PEL) could be adsorbed by Layer-by-Layer (LbL) technique (Fig. 4.9). Adsorption layers are achieved by depositing solution layers of positively charged poly(diallyldimethylammonium chloride) (PDDA) and poly(allylamine hydrochloride) (PAH), and negatively charged poly(sodium 4-styrenesulfonate) (PSS). PEL coatings are realised by stacking these alternating charged layers of electrostatic polymers (Fig. 4.9), which themselves can offer a host of surface functional groups such as amine or carboxylic acid groups.

To realise the LbL PEL coating, initially, an ECF (cleaved and pre-cleaned with methanol) was mounted in the optical characterisation setup (as described further in Ch. 5.1.3) with its exposed-core channel orientated upwards. A section of the fibre surface was cleaned and charged using a portable plasma generator (Arcospot PGS061). A PTFE deposition-trough was introduced from below the fibre.

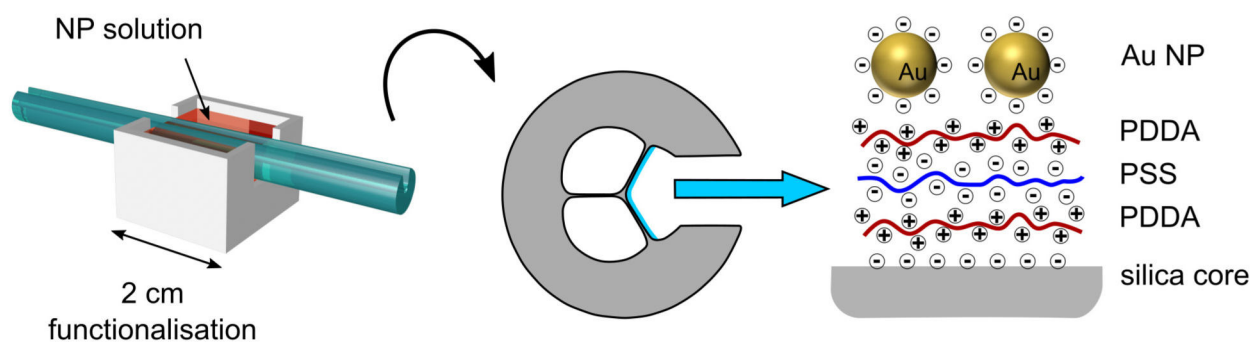


**Fig. 4.9:** Layer-by-layer (LbL) polyelectrolyte (PE) deposition on the exposed core wall of an ECF can be done in situ using a PTFE trough. Various numbers of layers can be bonded on the fibre exterior and on the exposed core and microchannel as shown.

This PTFE trough was first filled with a solution of poly(diallyldimethylammonium chloride), (PDDA, Sigma-Aldrich, average  $M_w < 100000$ ), which consisted of 170  $\mu\text{l}$  PDDA, 0.2 ml (3 M) NaCl, and 5.8 ml  $\text{H}_2\text{O}$ . The fibre portion in the trough was submerged for 10 minutes, creating a positively charged PE layer on the ECF silica surface. Afterwards the fibre was rinsed and dried. By this means, a PE layer of approx. 0.5 nm thickness can be built [229]. Finally gold NPs were introduced to the trough for immobilisation on the positively charged PE layer (Fig. 4.9).

A gold nanosphere solution (concentration  $1.55 \cdot 10^{14}$  NPs/l, diameter:  $45 \pm 4.1$  nm) fabricated by the Turkevich–Frens method [223, 224] was applied, which was suitable for 5 minutes of incubation time. A NP surface charge ( $-30$  mV) from citrate anions promotes bonding to the positively charged PDDA layer. The NP functionalised samples were subsequently rinsed and dried to remove excess, non-bonded NPs.

Polyelectrolyte deposition was typically applied to 2 cm sections of 15 cm ECF sample pieces. Capillary action, where the liquid front is essentially sucked along the microstructures due to the adhesion to silica being greater than the cohesion between water molecules, allows some deposition outside the PTFE trough region, which could be contained by an “in-fibre” acrylate trough approach (discussed in Ch. 5.4).

This technique allowed access to homogeneous low surface coverage such as densities of 4 NPs/ $\mu\text{m}^2$  (from scanning-electron microscopy (SEM) micrographs). The NP surface coverage density can be tailored for a particular NP size by altering the duration of immersion, the concentration of NP solution, or through PE layer selection, e.g., using a PE with a different charge density. A single PE layer was implemented for lowest distance between NP and silica core, but also layers including PSS and PAH were investigated (Fig. 4.10). In the end the single PDDA PE layer was found to be sufficient for NP immobilisation, and potentially helped avoid additional complications from scattering points (Ch. 5.1.3).

Overall the method of PE layer deposition was not as neatly contained in the ECF as the NLD technique within the SC-MOF, and did not replicate the deposition lengths achieved – although such a replication was not targeted, and slow continuous drawing through a PE solution could produce longer deposition regions if desired. However, this technique did offer advantages in that the sample was already mounted in the optical

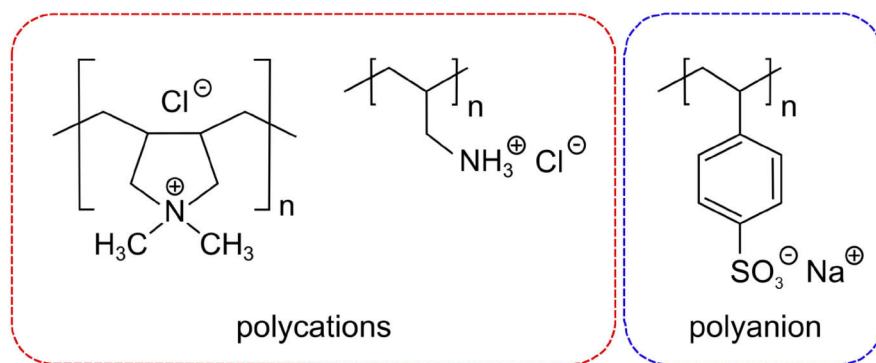


**Fig. 4.10:** Polyelectrolytes involved in LbL deposition include the polycations PDDA and PAH (in red), and the polyanion PSS (in blue).

transmission setup so deposition could be monitored, and the method was faster and less chemically intensive to apply. The plasmonic effect of the NPs could be immediately observed upon application to the core, in fact often optical guidance was lost rather easily due to growing attenuation from the depositing NPs.

#### 4.4 Characterisation of nanoparticle layer depositions

Prepared plasmonic MOFs were cleaved at different points along the deposition length and samples sent for SEM imaging to determine the homogeneity and coverage density at points along the fibre length and within the channels. This was carried out by imaging an end facet. The envisioned and realised system is shown in Fig. 4.11. SEM images showed NLD yielding highly uniform coverage along deposited fibres and around the channel curvature. Generally 2 m lengths were deposited as a means to reduce deposition time and since short lengths would be implemented during the optical transmission measurements (although 6 m is possible [126]). For higher density coverage, SEM images display a bright layer near the channel surfaces, indicating the presence of NPs. A fast immobilisation check can also be conducted under light microscope, from an end facet or side view. Higher densities result in a more strongly coloured fibre from side view, and short sections of higher particle density samples can be illuminated through the end facet and core, to observe coloured, scattered light from the NPs. Lower density depositions such as 1 : 10000 ratio of APTES : PROSI achieved successful homogeneity just as, if

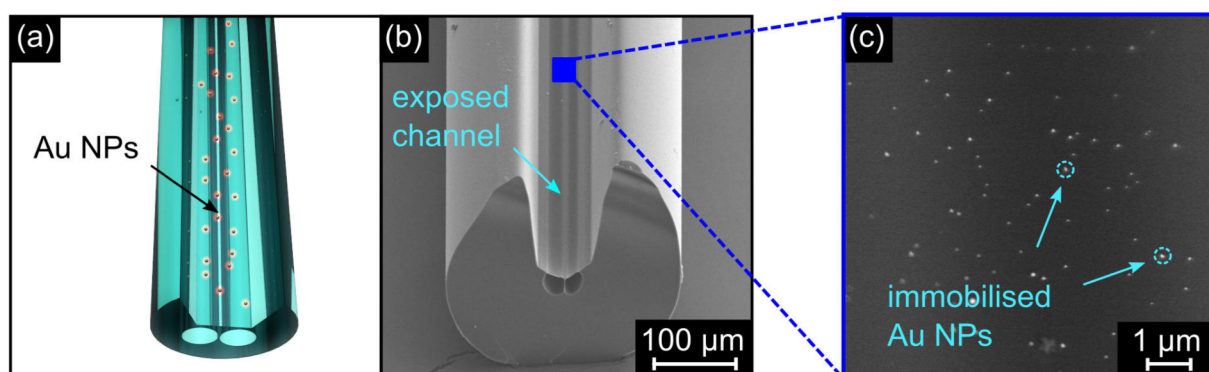


**Fig. 4.11:** (a) Rendered image of Au NPs in an ECF channel, (b) SEM of post-deposition ECF, showing the structure at an end facet, the blue box region is enlarged in (c) demonstrating the resulting NP layer on the core wall.

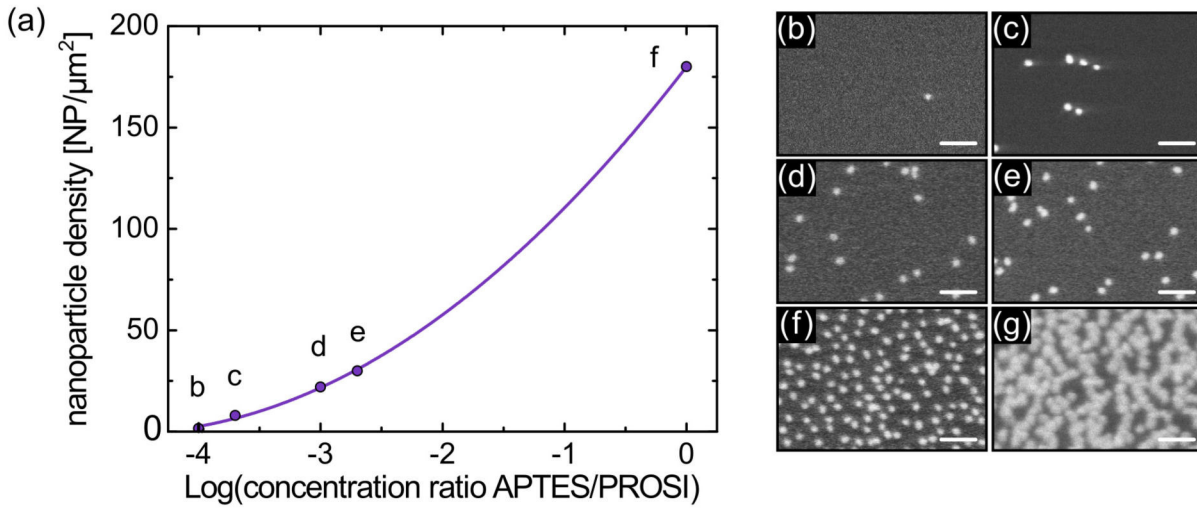


**Fig. 4.12:** (a) Deposited NP densities resulting from the ratio of bonding/nonbonding silane used. (b–f) SEM images corresponding to the silane ratios used in (a). The indicated densities are: (b) 2 NPs/μm<sup>2</sup>, (c) 8 NPs/μm<sup>2</sup>, (d) 22 NPs/μm<sup>2</sup>, (e) 30 NPs/μm<sup>2</sup>, (f) 180 NPs/μm<sup>2</sup>, and (g) an overdense layer of 500 NPs/μm<sup>2</sup>. The scale bars correspond to 200 nm with the scale bar in (g) indicating 100 nm.

not more, frequently as higher coverage densities. Provided that solutions were filtered at each use, microfluidic tubes exchanged every second deposition, and silanes checked visually for clarity to avoid introducing oligomers, quality NP layers were ensured. The main potential for inhomogeneity arose from the silanes; lower degrees of oligomerisation are difficult to observe so the silanes should be exchanged frequently or tested for quality before each use.

In summary the NLD worked very well for depositing plasmonic MOFs. Fig. 4.12 shows a number of deposition densities that were targeted and deposited homogeneously, and in the next step these hybrid plasmonic MOFs would be optically characterised. Experiments conducted on planar surfaces [230] indicate a certain trend for coverage density dependence on silane ratio, with a tendency to saturate at deposition ratio roughly 1:100. For this in-fibre deposition lower densities were targeted below saturation. Silane deposition ratios of 1:0, 1:500, 1:1000, 1:5000, and 1:10000 were deposited with their homogeneity included in Fig. 4.12b–f. The resulting NP density dependence on APTES:PROSI ratio,  $\Delta c$ , yields a curve fit:

$$N = A + B \log_{10} \Delta c + C(\log_{10} \Delta c)^2. \quad (38)$$

with the constants  $A = 179.95$  NPs/μm<sup>2</sup>,  $B = 78.00$  NPs/μm<sup>2</sup> and  $C = 8.41$  NPs/μm<sup>2</sup>, providing a guideline for further tailored density depositions.

While the NLD method consistently yielded high quality NP coatings, there are some factors that can affect the quality of deposition if not closely monitored. A suboptimal deposition can include factors such as:

- An unexpected low density or unfunctionalised fibre, which can be a consequence of a damaged end facet, contamination or air bubbles, or a problem during sur-



face activation. This can be minimised with perfect starting end facets and careful functionalisation steps.

- NP agglomeration or nanodomain formation resulting from silane oligomerisation or colloidal solution imperfection. The silanes involved were a hydrophobe and –phile, and occasionally domains or micelles with dark interiors and clustered edges were observed. Since the NPs don't bind individually at every binding site, the presence of an oligomer or cluster from solution can cause agglomerated deposits. This can be reduced by ultrasonication and filtering the colloidal NP solution before use, checking the silane solutions regularly for oligomerisation, and observing the microfluidic tubing during deposition.
- Scratches in deposited layers developing when a cluster enters through the tubing either directly from solution, or forms and detaches within the tubing or fibre. This agglomerate can scratch NPs from along the channel walls on its way out. This rarely occurs as it can generally be prevented by filtering solutions, regularly exchanging microfluidic elements, and monitoring the deposition.

The characterisation of the deposited ECF was similarly conducted by SEM imaging. In this case since the PE deposition occurred in situ, either the sample was first used and later cleaved for SEM imaging or two fibres were simultaneously deposited and one sent directly for SEM, the other later. Deposited regions were < 2 cm long and gradients along the section were not observed. Imaging could be achieved as with the SC-MOF, from an end facet, but the ECF also allowed imaging along the exposed channel to check homogeneity. In general lower densities were targeted as high density coverage resulted in the loss of optical transmission, by absorption and scattering processes, and the ECF could not be cut back as readily as a MOF sample. Cutback was prevented by the in-fibre trough, due to both its delicate structure and since cleaving within the trough would have resulted in analyte infiltrating the non-exposed channels and disrupting measurement values. Lower NP densities could always be increased if required. Some examples of ECF PEL depositions can be observed in Fig. 4.13. For comparison some

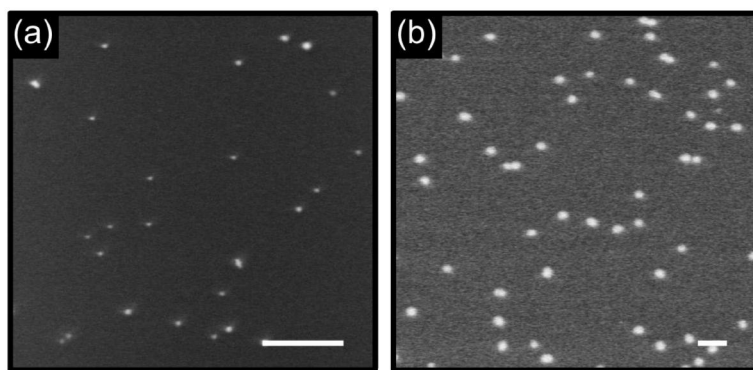


**Fig. 4.13:** SEM images of PE-assisted (PDDA) NP deposition in the exposed channel of an ECF; the NP diameter is 45 nm. (a) An example of a typical low density NP immobilisation; the scale bar indicates 1  $\mu\text{m}$ . (b) A higher density deposition with scale bar of 100 nm.

SEM images of aminosilane vapour phase deposition as discussed in Sec. 4.3.1.1 can be seen in Fig. 4.14 for the case of planar deposition and ECF deposition. Planar deposition yielded NP layers of much higher homogeneity compared to those in the ECF samples. Homogeneity problems must arise then either from addition of the NP solution; which was done either by dipping the fibre or by addition in PTFE trough; or from the channel curvature in the fibre itself. Regardless, the PE LbL technique was chosen as a faster more applicable route. Also shown in (a) is structural damage found in some ECF channels during post-deposition SEM analysis (discussed in Ch. 5.1.3).

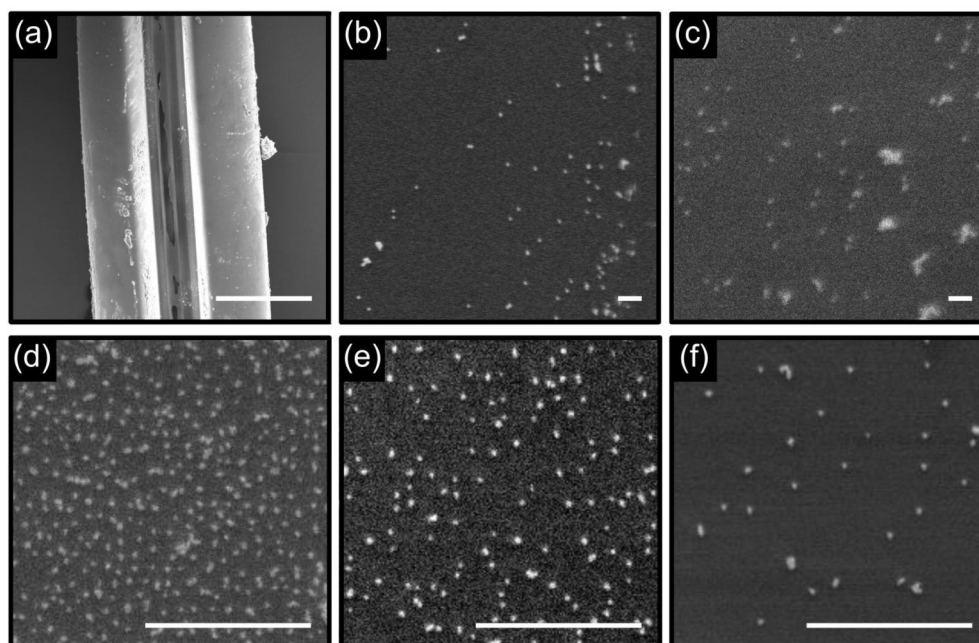


**Fig. 4.14:** SEM images of (a) structural damage found on an ECF – induced during drawing, deposition (discussed in Ch. 5.1.3), or pre-deposition – the scale bar indicates 100  $\mu\text{m}$ . (b–c) NPs on ECF core after NLD vapour deposition, the scale bar shows 100 nm. (d–f) NLD vapour deposition of NPs on planar substrate, with a scale bar of 1  $\mu\text{m}$ .

### Chapter summary

- The challenge of homogeneous internal fibre deposition was met using an NLD aminosilane wet chemistry technique.
- Specific NP densities can be targeted based on the ratio of bonding and non-bonding silanes. Homogeneous densities between 2–180  $\text{NPs}/\mu\text{m}^2$  were fabricated over metres of SC-MOF.
- The NLD approach can be implemented in vapour phase for taper or ECF deposition, however a PEL deposition yielded superior homogeneity and faster deposition times in this study.
- The ECF allows for site specific deposition regions along its core – potentially enabling multiple sensing regions in one device.

If the immobilised NP layer is to be used as a transducer for later DNA analytics investigations (through detection of a refractive index change), then the clear presence of an extinction peak in the optical fibre measurements and the position change of that peak during variation of the surrounding refractive index environment must first be ascertained. For this an “on-axis” transmission measurement system was used, coupling and guiding light along the deposited core region of the MOF in the dry state and looking at the corresponding output signal for presence of LSPR behaviour. Comparison with simulations (Ch. 3.2) allowed an approximation of the expected spectral impact for different particle densities at different fibre sample lengths.

In altering the refractive index of the microchannels, access to analytics and excitation light is required simultaneously at the same end facet of the plasmonic MOF, which is quite challenging. A number of approaches for targeting this are investigated and discussed. A number of the results shown in this chapter have been partially published [105, 106]. Another “cross-axis” measurement system is also highlighted where the NP layer is characterised by transverse-to-core illumination and collection of light. This technique can quickly check LSPR response in small targeted high coverage sections along the fibre. It therefore presents a helpful tool to verify layer homogeneity and initial plasmonic response. This chapter specifically targets the topics:

1. Do the NP coated fibres show a clear extinction effect?
2. Can the attenuation be characterised and what constitutes an applicable sample?
3. How can optofluidic sensitivity measurements be implemented on these samples?
4. Is this sensitivity adequate for a future application in biosensing?

### 5.1 Concept of LSPR characterisation using an “on-axis” measurement

The core-guided, on-axis characterisation approach involves optical guidance along the direction of the fibre axis. Guiding along the entire length of the fibre sample enables long interaction lengths with the NPs fixed on the core walls – which cannot be accessed by other transmission techniques using chips or even cross-axis fibre measurements. The core-guided technique does present challenges in the form of strong attenuation in high NP coverage fibres, and in the resulting highly demanding fibre alignment necessitated by these greatly reduced sample lengths. Indeed the small-core, high refractive index contrast fibres used in this study already require a high NA objective for in-coupling and simply fibre cleaving these delicate structures also requires close quality monitoring.

#### 5.1.1 On-axis measurement setup and protocol

A SuperK COMPACT Supercontinuum White Light Laser (NKT Photonics), providing a total output power of 120.2 mW and an output spectrum covering the range of 450–

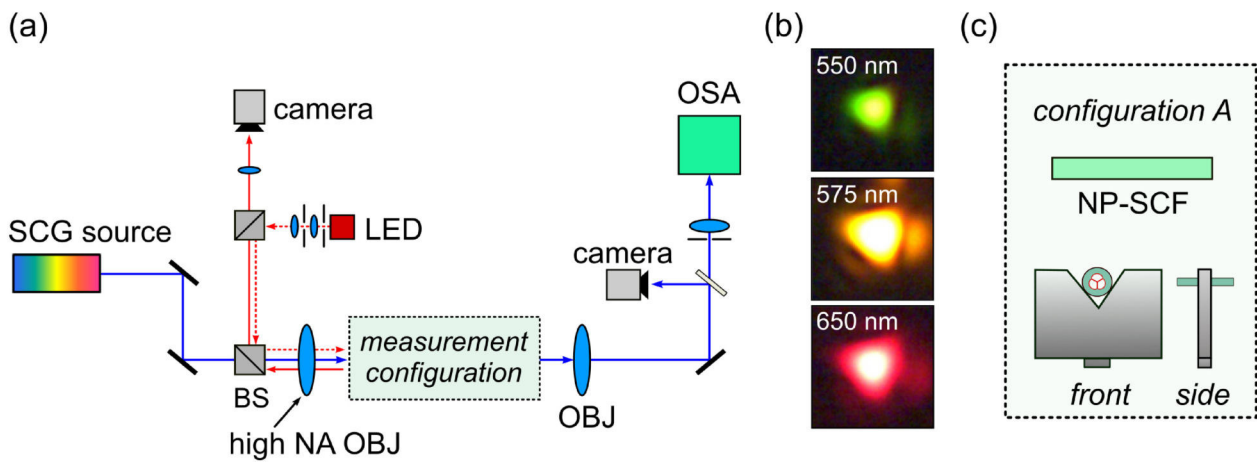


**Fig. 5.1:** (a) On-axis measurement setup detailing components and beam path. (b) Examples of output camera mode images at wavelengths of 550, 575, and 650 nm. (c) Fibre mounting configuration A for on-axis core light coupling.

2400 nm, was used for fibre in-coupling in the on-axis measurement configuration. For experiments incorporating immobilised nanospheres in the symmetric microstructured fibres, a specific light polarisation was not required. In the case of SPP experiments or nonsymmetric NPs, for example nanorods, a set of polarisation optics can be implemented in front of the in-coupling objective to set input polarisation. As detailed in Fig. 5.1, the first stage in this setup configuration (succeeding a set of beam alignment mirrors) involved mounting and in-coupling of the fibre sample. A short fibre holder was required, typically a 1 cm (Elliot Scientific Ltd.) fibre holder or a shorter v-grooved holder together with some doubled sided adhesive tape to prevent fibre movement and allow cleaving during cutback measurements (Configuration A, Fig. 5.1).

As mentioned, a high NA is required for in-coupling to these small-core SC-MOFs, in this case a  $100\times$  (NA 0.9, WD 1.0) objective was used possessing a long working distance. A  $20\times$  (NA 0.4) objective was positioned at the fibre output facet such that the out-coupled image was of sufficient size to cut off any potential non-core scattered light, using an iris aperture.

Once the fibre sample was mounted and positioned, as in Fig. 5.1a,c, coupling into the fibre core could be achieved; a process that was simplified by including a back focal imaging and a CCD camera. A back focal imaging setup permits visualisation of the fibre input facet; which both reaffirms the quality of the input fibre face and struts (a clean, smooth facet cleave enables undistorted in-coupling to the MOF), and also ensures that the laser spot ( $\sim 3$  mm diameter) is focussed directly onto the small suspended core. The back focal imaging setup consisted of a pellicle beamsplitter (removed before transmission measurement), an LED (660 nm), and a USB camera (Thorlabs DCC1545M CMOS).

The transmitted modes and scattered output of the fibre end face was monitored by a second CCD USB camera (also Thorlabs), in the far field. Transmission modes of selected wavelengths could be monitored by inclusion of wavelength filters, as in Fig. 5.1b. The MOFs studied were all multimode, although the fundamental mode alone was targeted

for excitation. The fundamental mode has the highest overlap with the fibre core and is the least difficult to excite consistently and in an isolated manner. Due to the multimode nature of the fibre it was however possible to excite other higher order modes. Higher order modes are less confined to the fibre core and could overlap to a greater extent with the microstructures – leading to a rapid attenuation and loss of light guidance. They can also lead to interference and mode beating in the output fibre spectrum. The complete absence of higher order modes or coupling to higher order modes at some point in the fibre cannot be guaranteed, however monitoring the output mode shape ensured the fundamental mode was primarily excited. This monitoring process also assisted later with analyte filling to ensure that all microstructured regions were fully infiltrated. The combination of back focal and transmitted mode imaging ensured good facet cleaves, non-broken microstructured regions, and in conjunction with an output powermeter helped deliver optimal core guidance.

The transmitted light from the end face of an Au NP deposited MOF imaged on a laser card immediately showed a bright red spot (depending on NP size, shape, and density) from the presence of the NPs along the fibre core wall. Once coupling efficiency was optimised, the output core light was passed through an iris (eliminating any cladding light) and coupled into a delivery fibre and into an Optical Spectrum Analyser, OSA (Yokogawa, measurement range 350–1750 nm).

At higher spectral wavelengths, interaction with cladding modes may need to be suppressed, the general practice for which is to either use a refractive index matching gel on the fibre or to optimise coupling at a specific wavelength. For millimetre long fibre samples or the ECF structure, refractive index gel is quite messy and undesirable, hence the latter technique was utilised for transmission measurement with optimisation at 650 nm.

A source of measurement difficulty with this system was the detector sensitivity level (around  $-80$  dBm). For high density samples this posed particularly challenging for recording clearly the LSPR spectral dip. In general sample lengths needed to be shorter than 1 cm in length. An extended measurement range was run in order to notice any anomalies or cladding mode transmission arising at higher wavelengths. A short pass filter was also included to cut out the inherent laser peak at 1064 nm (typical Nd:YAG) and the second harmonic at 532 nm, which occurred due to the internal gratings of the OSA. This filter also affected the input power to the spectrometer, making it more difficult to obtain sufficient power for clear, recordable resonance dips for higher density samples.

#### 5.1.2 Cutback measurement and analysis – SC-MOF

After initial beam alignment, mounting, imaging, coupling optimisation, and recording the optical transmission spectrum of a particular fibre sample, the cut-back method could be implemented in order to determine the attenuation loss of that particular sample coverage. This is a popular destructive technique within fibre optics for invest-

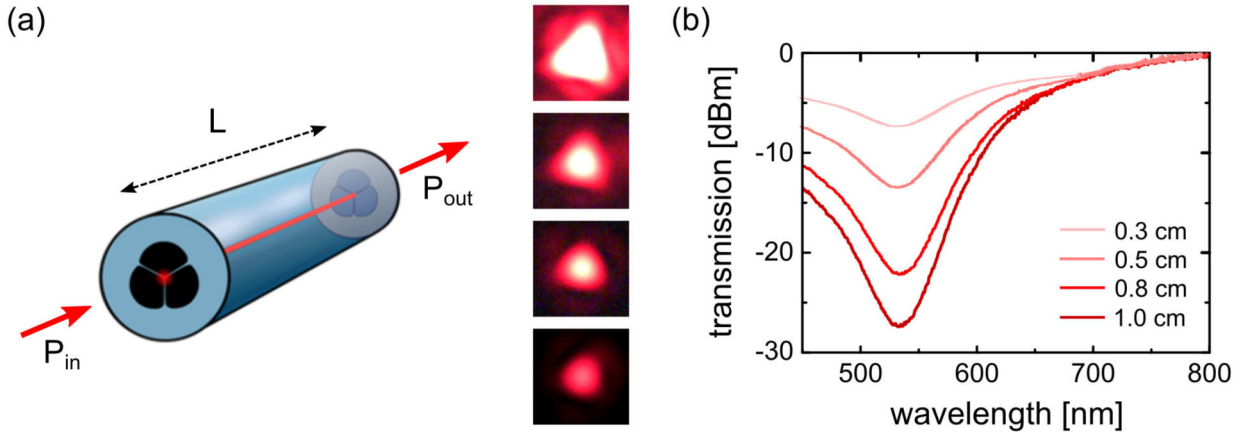


**Fig. 5.2:** (a) Cutback method with output modal images at 650 nm corresponding to different fibre lengths – descending with increasing length. Higher intensity is output as the fibre is cut shorter (due to less attenuation from NPs). This is also clear in (b) showing the spectral transmission for the corresponding cutback sequence (1 cm to 0.3 cm). The large dip in the transmission at 528 nm is from the LSPR of immobilised NPs.

igating fibre transmission characteristics, for instance attenuation or bandwidth. The power,  $P$ , propagating in a fibre in the  $z$  direction (related to the axial Poynting vector  $S_z = \frac{1}{2}\Re(\mathcal{E} \times \mathcal{H}^*)_z$ ) decreases exponentially with distance due to absorbance. Therefore the fibre's wavelength dependent attenuation per unit length can be determined using input power,  $P(z = 0)$  and output power after a distance  $L$ ,  $P(z = L)$ , as

$$\alpha \left[ \frac{\text{dB}}{\text{m}} \right] = \frac{1}{L} \cdot 10 \log_{10} \left( \frac{P(z = 0)}{P(z = L)} \right). \quad (39)$$

Cut-back, as the name suggests, involves experimentally cleaving back the end fibre facet to shorter lengths without disturbing the input coupling and retaking a transmission measurement. In Fig. 5.2a the mode intensity is seen to increase with each cutback as the number of NPs and thereby the attenuation is reduced and the output transmission increases. The transmitted spectrum after each cutback shows the characteristic LSPR dip expected from the immobilised particle size, which is more dramatic for longer sample lengths. Cutback was undertaken for a range of sample lengths and the spectral data compared for each density as in Fig. 5.2b. The transmission intensity for a particular sample density at different sample lengths is compared at each spectral wavelength to provide the total attenuation of that particular sample as in Fig. 5.3a. In the case of NP immobilised fibre samples this attenuation presents as plasmonic resonance response from the NPs. Cleaving of the end facets of the MOFs was achieved manually with great care using a ceramic cleaving tile. Due to the short sample lengths fibre cleaving devices were not feasible.

As a reference, corresponding lengths of empty SC-MOF were used. Since the deposited NPs induced strong attenuation, very short sample lengths were used and attenuation was calculated in dB/mm. This method was implemented for a selection of the plasmonic NP densities immobilised in Ch. 4.3.1 (Fig. 4.12), and their varying attenuation behaviour with NP coverage is plotted in Fig. 5.3.

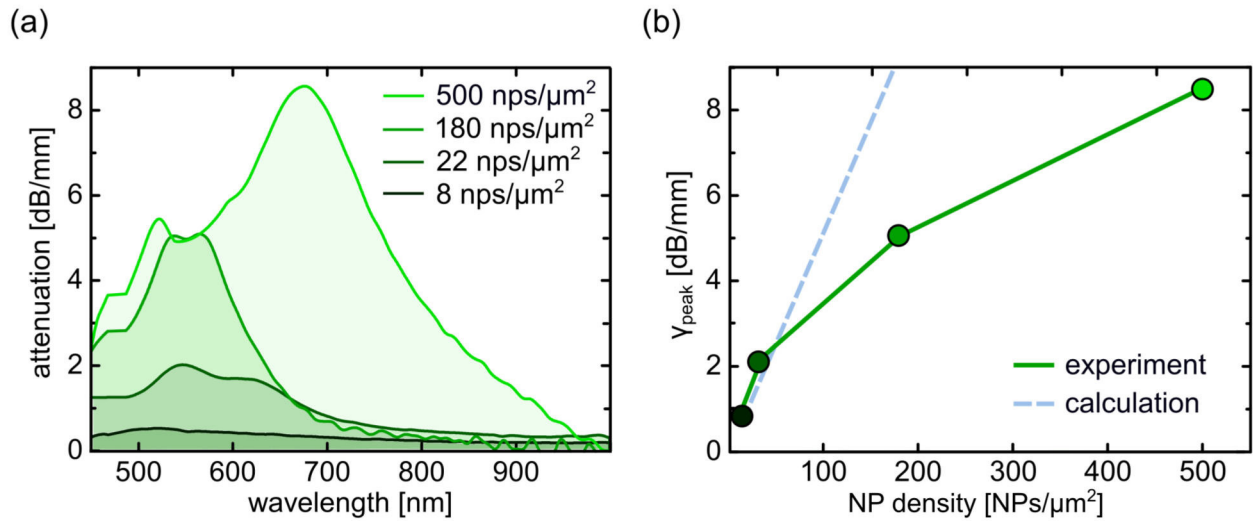


**Fig. 5.3:** (a) Attenuation of plasmonic fibre samples of various immobilised NP densities acquired through cutback measurements. (b) The corresponding attenuation peak strength (green) increases with NP density with a plateauing effect at high densities (tending towards a thin film layer and total attenuation of power). The attenuation behaviour calculated using Eq. 34 is shown (blue) for a linear increasing NP number.

The spectral distribution of the modal attenuation of the plasmonic SC-MOFs is seen to exhibit a notable increase in the vicinity of the anticipated bulk LSPR, around 528 nm (Fig. 5.3a). It is clear that a higher density of immobilised NPs leads to a greater modal attenuation (as suggested by Eq. 34). The small-core MOF used in this work allows both extremely low NP densities (2 NPs/μm<sup>2</sup>) as well as very high coverage up to 500 NPs/μm<sup>2</sup> to be accessed. In Fig. 5.3 a low density deposition of 8 NPs/μm<sup>2</sup> is shown to still produce a detectable attenuation peak at NP resonance, whereas a high density deposition of 180 NPs/μm<sup>2</sup> yields a much greater attenuation but limits sample lengths to below 1 cm. For this reason densities of around 22–30 NPs/μm<sup>2</sup> were targeted, which allow slightly longer sample lengths (still < 2 cm) and good LSPR fringe contrast in spectra. A higher almost layer like density of 500 NPs/μm<sup>2</sup> is included in the given modal attenuation plot (SEM shown in Fig. 4.12g). For the highest immobilisation densities the average inter-particle (edge-to-edge) separation,  $g$ , is reduced (for 180 NPs/μm<sup>2</sup>,  $g = 40$  nm, for 500 NPs/μm<sup>2</sup>,  $g = 10$  nm, Fig. 4.12f,g) enabling interaction between the LSPRs of neighbouring NPs. This affects the linear dependency expected between density and attenuation (Fig. 5.3b, green curve). A theoretical linear attenuation behaviour (Fig. 5.3b, blue line) is calculated based on the approach of Ch. 3.2, which assumes a low NP density that does not affect the propagating mode profile. This approach is however not valid at higher NP densities where the presence of an increased density of NPs would indeed impact the mode profile. This deviation between model and experiment can be seen in (Fig. 5.3b). The experimental samples in fact exhibit pronounced double-peak features in their attenuation, presumably arising from neighbouring NP interaction (i.e., plasmonic hybridisation) and from the polarisation dependence of the scattering process as the guided mode’s dominant electric field component varies at different NP locations along the core. As shown in [231] nearest neighbour NP coupling imposes a red shift for the

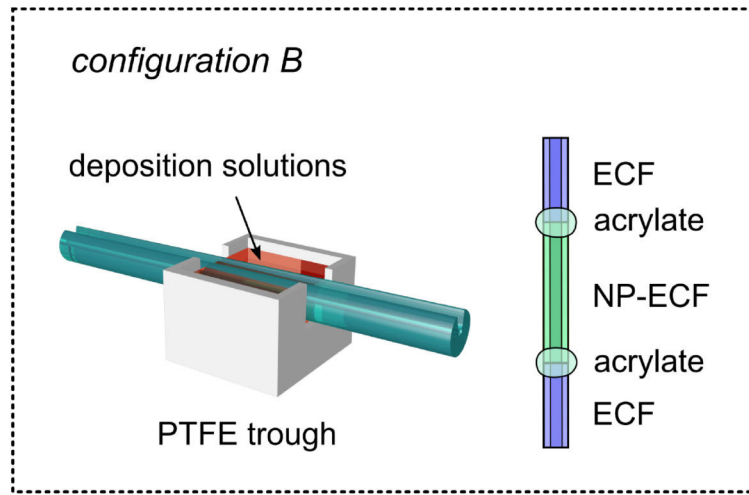


**Fig. 5.4:** ECF deposition can be conducted in real time in the on-axis measurement setup using a PTFE trough mount. The deposition can be contained to an in-fibre trough using drops of low RI acrylate such that only the green core section as indicated is deposited.

case of in-plane electric fields and blue shift for out-of-plane fields. Additionally a strong resonance wavelength shift is observed for lower NP separation distance as confirmed in the spectra presented for the highest density case.

### 5.1.3 Measurement and analysis – ECF

In the ECF case, deposition was performed in real time with the sample mounted in the on-axis optical characterisation setup in a trough mount (as shown in Configuration B, Fig. 5.4), still employing the high numerical aperture objective for fibre in-coupling. A drop of low RI acrylate (Fospia EFiRON PC-363) was applied to the ECF at the trough edges under microscope and UV-cured to prevent capillary action. For this system, power optimisation was again conducted at a single wavelength to accurately resolve the LSPR resonance dip. Preliminary simulations indicated only minor dependence on input polarisation so that polarisation control was omitted as before. Oftentimes initial bare fibre reference testing showed core guidance in the ECF, however a number of scattering sites were present along the fibre length. Measurements across a range of fibre samples showed that many times the scattering was sufficiently large such that no light propagated to the output facet, even when using bare fibres lengths  $< 20$  cm. Often additional scattering sites appeared during deposition or upon exposure to analyte, and the transmission was severely decreased or attenuated completely. This is attributed to either contamination from the fibre drawing process – the preform is cleaned after milling open the core but not after caning [222] – or to the strut fragility – the thinness of the struts over such a long length carries a high risk of mechanical damage. More significantly, the completely exposed channel region allows potential contaminants easy access.

During characterisation, fibre samples with immediately visible scattering points were discarded and those selected for deposition were rinsed with water to check whether transmission remained i.e., that no leakage into the other channels from microcracks or mechanical damage was present. During deposition such regions of high scattering were noted and sent for SEM investigation. In some regions direct physical damage or con-



tamination was evident, as shown previously in (Fig. 4.14a). Where these points were evident pre-deposition the damage could be a result of dust or salt contamination perhaps with direct physical contact on the delicate exposed region resulting in structural damage and light scattering. When the scattering occurred during deposition it was unclear if it was a result of pre-existing damage being expanded (rinsing open holes or additional etching of weak points for instance) or pre-existing contaminants aggregating and further causing sticking points for NPs etc.

Overall precautionary measures were observed such as wrapping the fibre spools in plastic and storing them under argon in a clean box to minimise exposure to dust and extra airborne contaminants. Gloves were worn during all fibre handling to further prevent contaminant transfer. Experimentally, starting samples were carefully selected and deposition processes were simplified by using less aggressive chemicals (for instance not using piranha solution for silica activation) and reducing the number of steps, i.e., fewer PE layers and shorter NP deposition times. With such precautions NP-immobilised ECFs were successfully created with well-defined, plasmonic-NP induced transmission dips.

## 5.2 Concept of LSPR characterisation using a “cross-axis” measurement setup

Worth mentioning is that the immobilised NP layer could also be characterised by transverse-to-core illumination and collection of light. In this orientation the illumination light was passed through a section of the fibre from the side such that the light was not guided by the core, rather passed through 4 monolayers of immobilised NPs sitting on the channel and core walls. This orientation allowed high density fibre samples to be characterised quickly and indicated the presence of any agglomerates or clusters of NPs from “shoulders” in the characteristic LSPR spectra. This allowed a faster precursor option for homogeneity inspection than SEM imaging. The technique was position dependent and not practical for lower density samples with lower peak contrasts. In this manner the LSPR response could be quickly checked in small targeted high coverage sections along the fibre – a helpful tool to verify layer homogeneity and initial plasmonic response.

### 5.2.1 Cross-axis measurement setup and protocol

White light illumination was introduced using a halogen light source (DH2000, Ocean Optics). A section of NP-deposited SC-MOF was stripped of coating, cleaved (using a Fujikura fibre cleaver), and mounted vertically within the collimated beam (see Fig. 5.5a). Directly behind the vertical sample, a large core (50  $\mu\text{m}$  – essentially a pinhole for the measurement) fibre was aligned such that only that part of the light transmitted directly through the plasmonically modified MOF was collected.

To achieve alignment, light was focused by a lens onto the mounted vertical sample. Behind the SC-MOF a large-core collecting fibre was aligned by microscope, selecting only the light transmitted through the SC-MOF. Firstly their separation along the propagation distance was reduced. Next, any offset across the propagation axis was eliminated

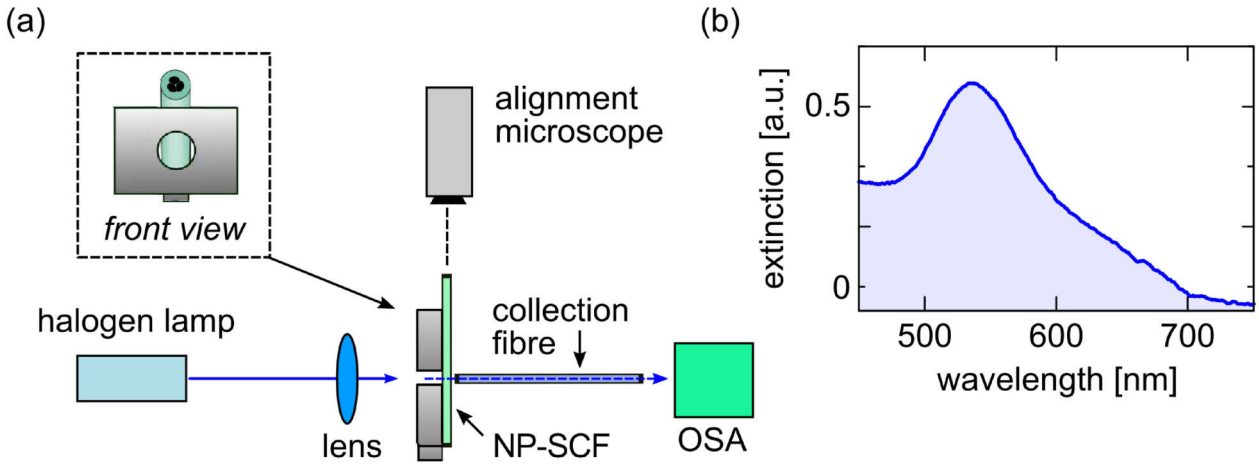


**Fig. 5.5:** (a) Cross-axis measurement setup, including the mounted plasmonic NP-SCF (here the SC-MOF) and transmitted light collection. (b) Output extinction spectrum showing LSPR behaviour.

using a prism for alignment on the incident fibre side. Finally, the along axis separation was minimised. The collection-fibre guided light to a spectrometer (Spectro 320D, Instrument systems) allowing a long wavelength measurement range, from 190–2000 nm, for analysis with SpecWinPro software.

In this configuration, plasmonically modified fibres with sufficiently high NP coverage provided sufficient light-NP interaction to exhibit a clear, discernable extinction spectrum with characteristic LSPR peak (Fig. 5.5b). The extinction spectra  $E(\lambda)$  are calculated by:

$$E(\lambda) = \ln \left( \frac{I_{\text{ref}}(\lambda)}{I_{\text{meas}}(\lambda)} \right), \quad (40)$$

with reference intensity,  $I_{\text{ref}}(\lambda)$ , measured on an SC-MOF without nanoparticle layers and measurement intensity,  $I_{\text{meas}}(\lambda)$ , which is transmitted through the plasmonic SC-MOF. Thus, the wavelength dependent absorption and scattering behaviour of different NP layer coverage could be obtained. The high signal-to-noise ratio however, prevented LSPR behaviour of low coverage fibres from being so clearly detectable. Benefits of this setup configuration include the detection of clustering or dipole-dipole interaction, which presents as spectral “shoulders” near the LSPR peak. Additionally, an indication of coverage density changes when readings are taken along the length of a modified fibre can be obtained. For instance when comparing the start and end sections of a 5 m sample, a lower extinction spectrum near the sample end would indicate less dense coverage and the need to run the deposition for longer. In this manner the cross-axis transmission setup is a good accompaniment to the NLD deposition technique – the immobilisation within the fibre could be monitored in real time.

Comparison of the resulting extinction spectra can be accomplished with bulk solution and Mie theory to provide a concrete experimental idea of position, strength, and width of resonance(s) within the SC-MOF before implementing on-axis characterisation. The curvature of the fibre surface does not however permit a quantitative comparison. The

primary weakness of this approach is the lack of core guidance. What is observed is the effect of the 4 monolayers of NPs (one layer from each channel/strut/core wall) that the light passes through, not guidance in the core or struts – indeed distortion could possibly be induced at these points. To investigate this, the fibre orientation relative to incoming light (turning and tilting) was altered with negligible effect on the spectral intensity.

### 5.2.2 Cross-axis sensitivity measurement

In order to change the RI environment of the NP-immobilised microstructured channels in the vertically mounted SC-MOF sample, an initial test using a water droplet from a syringe and employing capillary forces was undertaken. The fluid front could be observed rising up the fibre using a microscope. In this manner, a basic RI-based LSPR peak position shift could be observed with reference readings being made using a bare undeposited SC-MOF sample.

The cross-axis configuration does not require analytics and light coupling from the same fibre facet and both ends of the sample are potentially accessible for analyte filling (achievable for instance using a syringe or peristaltic pumping system as in Ch. 4), simplifying the measurement from the on-axis case. To determine the modified sensitivity of the SC-MOF capillaries (from the spectral resonance position shift), a water-based (glucose) RI series was introduced by pumping one end of the mounted sample. The spectral measurements were taken on the same sample location without varying in- or out-coupling, to guarantee reproducible spectra. The fibre was rinsed with water (repeatedly switching pump flow direction), dried (by induced air bubble), and a control spectrum was taken after each RI series measurement. This process was repeated until the original dry spectrum was reproduced, thereby ensuring previous analyte traces were removed and verifying the Au NP bond stability to the silica surface (i.e. that the NPs were not being removed in the process). Using a glucose series allowed for easier sample cleaning than for instance an oil-based RI series, but restricted the accessible RI range. Taking a 22 NPs/ $\mu\text{m}^2$  plasmonic SC-MOF sample (showing good fringe contrast

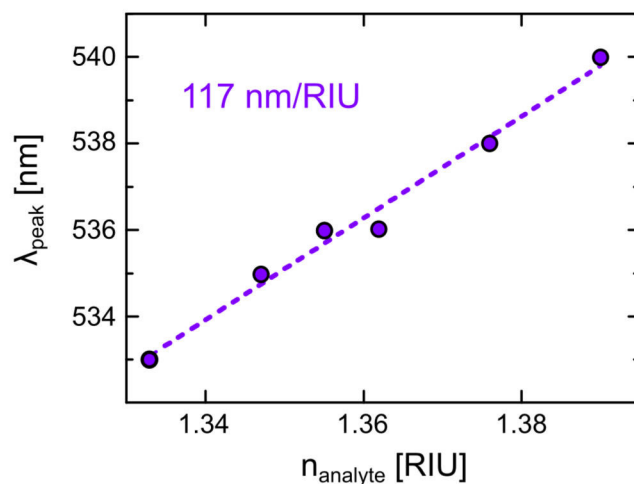


**Fig. 5.6:** Plasmonic SC-MOF sensitivity determined by cross-axis measurement setup. This yielded a sensitivity of 117 nm/RIU, for a 22 NPs/ $\mu\text{m}^2$  coverage, using a glucose RI series.

LSPR behaviour) a sensitivity of 117 nm/RIU was determined by tracking the shift in LSPR peak position at each RI value (see Fig. 5.6). This corresponds closely with predicted values for sensitivity of NPs on a silica SC-MOF (118 nm/RIU without substrate effect). Overall, this configuration has its limitations but simplifies the extinction and sensitivity measurements of high NP coverage SC-MOFs as it involves the separation of optical and fluidic paths, and precision coupling into small cores is not required.

### 5.3 Strategies for optofluidic measurement in SC-MOFs

After verification and characterisation of the attenuation effect of the plasmonic NP layer on the transmission spectrum of the SC-MOF, the sensitivity with changing RI environment of the system could be studied on-axis. The challenge presented in this section is due to:

1. The strong attenuation of samples possessing high NP density.
2. In-coupling light and fluidics simultaneously at the same fibre facet.

#### Strategy 1: Polydimethylsiloxane (PDMS) chip

The first approach involved moulding a simple PDMS chamber (see Fig. 5.7a) such that light would be incident on a thin quartz coverslip, plasma bonded to a PDMS structured flow chip. Ferrules and a sleeve would hold the fibre in the PDMS side which would be inserted under microscope to minimise distance between input facet and cover slip. An aluminium template slab was cut in order to mould the PDMS layer. The chips would consist of either an input port allowing fluidic pumping into and through, the fibre facet that would be mounted in the channel area, or an in- and output port configuration, to enable pumping across the facet.

The PDMS section was fabricated using Sylgard 184 Silicone Elastomer Kit (Dow Corning) and a base and curing agent ratio of 10:1. The components were mixed in a test tube by slow rotation until they no longer had layer separation, then vacuumed for 10 minutes. Air bubbles were released before vacuuming the mixture for a further 20 and 40 minutes with bubble release in between. The mixture was then carefully poured over the template slab and vacuumed for an additional 30 minutes. Lastly the template was baked at 60°C for 2 hours before cooling and peeling off. The moulded PDMS chambers were plasma bonded (removing organic residues and activating the surfaces) to coverslips and heated for a further hour at 90°C.

Different thicknesses of PDMS layer were investigated before settling on 2 mm. This thickness was sufficient to hold a ferrule securely and bonded strongly to the coverslip. Although bonding should be somewhat invariant on thickness, layers exceeding 3 mm thickness eventually separated from the glass – likely due to handling and the extra physical manipulation required for ferrule insertion at larger thicknesses. The ratio of agents was also varied; however the standard 10:1 gave the most desirable combination of flexibility and strength.

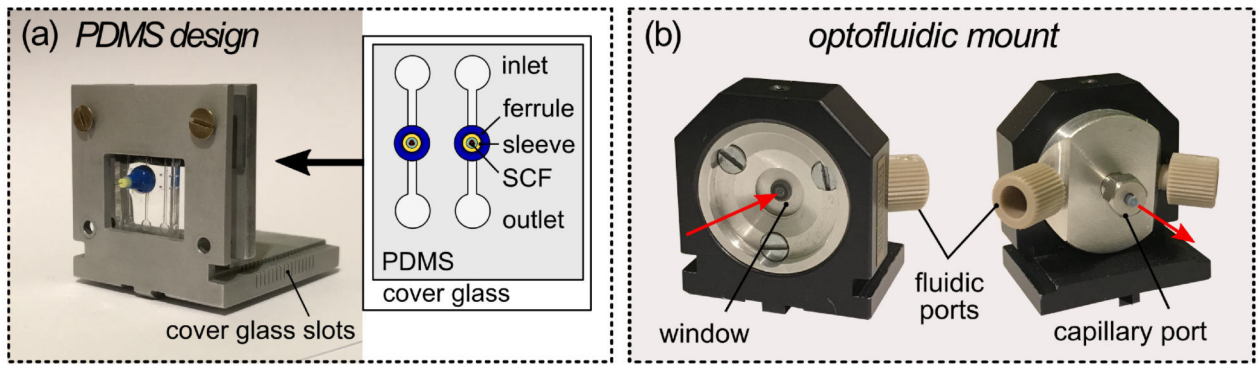


**Fig. 5.7:** Strategies for optofluidic coupling using (a) a PDMS chip and ferrules, where in- and output fluidic ports as shown in the inset are accessible from the opposite side of the holder. The chip direction here is flipped in the mount for better visual comparison with the inset. (b) An OFM, the red arrow indicates in- and out-coupled light path.

Another aluminium mount was designed for this chamber (Fig. 5.7a) in order to provide stability for microfluidic connects for pumping and to help hold and align the sample at the right height in the transmission setup. A further removable coverslip needed to be mounted at the fibre output facet to ensure a flat output face when fluids were added. This avoided droplet induced bulging and distance variations that would disturb and render the transmission unstable. A series of slots were included in the holder at 0.2 mm intervals for this purpose.

In principle this approach would work; as long as it was well vacuumed and devoid of air, the PDMS moulded cleanly without bubbles, the PDMS-glass bond held without leakage, and the coverslip was thin enough to not complicate in-coupling.

The challenge arose with mounting the fibre precisely straight and without leakage in the PDMS. Different approaches were carried out, for instance, inserting the ferrule before curing the PDMS, after curing the PDMS with adhesive support, and simply sticking the fibre in the PDMS. Curing the PDMS around the ferrule offered the lowest possibility of leakage, but the ferrule was often not precisely straight, either as a result of movement before going in the oven, during curing time, the oven having some minute tilt, or the ferrules themselves not being designed for such precision. Inserting the ferrule after curing usually resulted in leakage after fluidic pumping, eventually even with adhesive support. Simply sticking the fibre into the PDMS proved difficult to avoid damage of the fibre end facet even with a premade incision (that often prompted later leakage). In general curing around the ferrule was the best approach to avoid leakage but difficult to in-couple with the induced angles. It was possible to take measurements using this approach with some of the post-inserted ferrule samples but leakage always occurred after the third or fourth rinsing or refractive index series inclusion. Such leakage prevented the fibre sample from being completely filled or rinsed thereafter. Pumping through the fibre in one direct channel was more effective than across the fibre (positioned between input and output ports) as rinsing times were faster and air bubbles for drying could be induced more easily. Occasionally such air bubbles were a problem; if the PDMS near the

ferrule had been roughened during ferrule insertion these air bubbles could get stuck in front of the fibre face or in one channel.

Overall this approach was promising; successful measurements were conducted although a broad RI measurement series was not fully achieved. However, the ferrule inclusion issue requires further refinement and the reproducibility in this respect was too limited therefore alternate solutions were investigated.

### Strategy 2: Microfluidic holder

Light and analytics can be simultaneously coupled into the same fibre facet with a suitable optofluidic mount, OFM, (as shown using PDMS in Strategy 1), a long working distance objective and a pump system. Such a mount consists (see Fig.5.7b) of a fluidic input connection area on one side, a thin cover disc (of glass/sapphire) to in-couple light, and an output connection area directly opposite to hold, via fluidic adapter, the fibre sample. The fibre sample is held in a sleeve within a ferrule, in the output adapter, and the distance to the input window minimised under microscope. The distance between fibre input facet and external side of window was 1–2 mm. Again a pump system was incorporated, attached to the fluidic port of the mount to infiltrate the fibre system.

Challenges arose however, again due to sample length. The glass input window and any liquid between the input facet and window reduced input intensity, and made coupling additionally demanding. Coupled output power for the longest samples with sufficient LSPR fringe contrast was too low for the spectrometer at the required 2 cm length needed for the holder. At shorter lengths handling was no longer feasible. As sample lengths needed to be reduced, alternate configurations were required.

### Strategy 3: Optofluidic mount (OFM) and butt-coupling

Finally a reliable, reproducible system was reached by implementing the microfluidic holder from Strategy 2 but fixing a bare unmodified SC-MOF sample in it (see Configuration C, Fig. 5.8). This uncoated “delivery” SC-MOF was butt-coupled to the NP-functionalised short (3 mm) sample, with the facet juncture sealed within a 140  $\mu\text{m}$

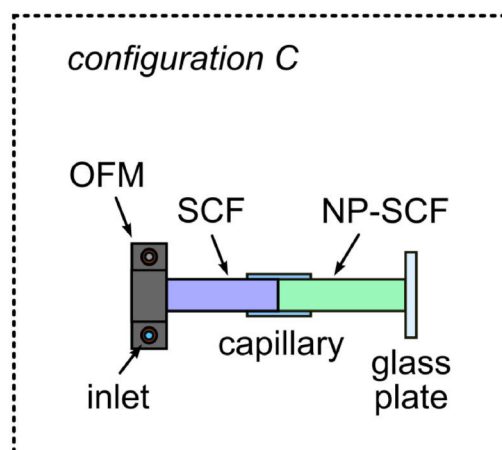


**Fig. 5.8:** Configuration for insertion into the on-axis setup: an optofluidic mount combined with butt-coupling of a non-deposited and plasmonic NP SC-MOF (shortened to NP-SCF).

inner diameter capillary whilst optimising the output mode and transmission. Thus, stable launching conditions could be maintained without significantly affecting the overall modal attenuation. This is the approach that would be implemented for sensitivity measurements using the SC-MOF in Sec. 5.5.

### Alternative strategies

Other strategies to infiltrate MOFs with fluidics include:

- Opening the cladding of a microstructured channel at a point along the fibre to directly connect fluidics into the channel. The channels could potentially be opened by chemical etching with Hydrofluoric acid, HF, with the fibre under internal pressure, however this is not extremely precise or entirely reproducible, and the HF may come in contact with the internal struts or core damaging the fibre.
- Laser drilling with a femtosecond laser and ion beam etching with a FIB (focused ion beam) could also be implemented. However FIB is rather time consuming with an estimated 14–20 hours to penetrate one MOF channel and both techniques may contaminate the microstructures with dust or debris, which would affect transmission. These techniques would also be disruptive to any immobilised NP layer.
- Filling two of the channels with an adhesive (for instance drops of UV curable epoxy-glue), depositing the third channel, and lastly cleaving the entire system to have a long, single channel (or particular NP species-per-channel) filled sample. Due to the greater length and lower attenuation such a sample could be more easily mounted and pumped for sensitivity measurements (Fig. 5.9). The danger with this sample length elongation idea is that the glue may rise considerably up the channels by capillary action before curing and any residue on the core surface will induce additional attenuation and scattering.

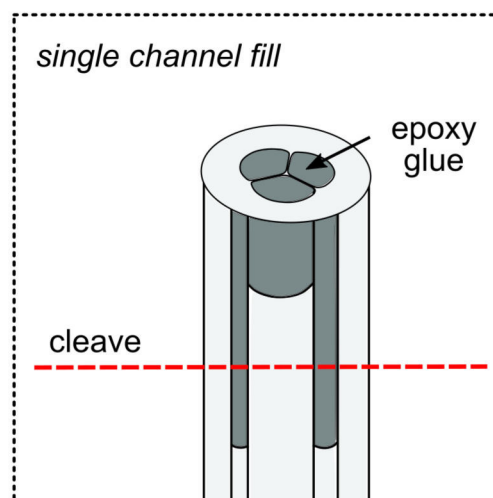


**Fig. 5.9:** Strategy involving sealing two microstructures with glue with one remaining open – accomplished by filling one at a later time, curing, and cleaving at the red dashed line.

#### 5.4 Strategies for optofluidic measurement in ECFs

The ECF presented a different type of challenge for optofluidic measurement. Due to the open exposed channel, mounting within a similar holder was not feasible. This fibre was evidently more delicate and required careful handling. The open channel would make microfluidic connection, pumping, rinsing, and contamination all issues to contend with.

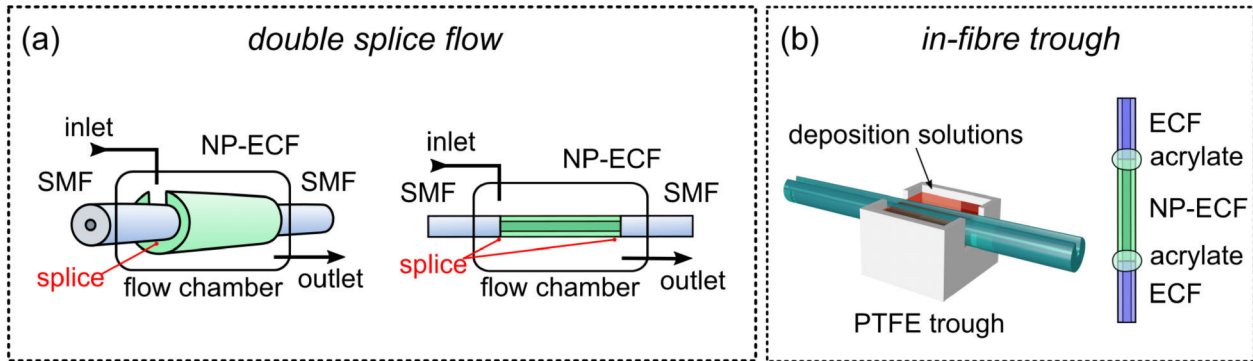


**Fig. 5.10:** Optofluidic strategy concepts include (a) a double-splice flow cell consisting of in- and outlet fluidic ports and a flow chamber housing the NP-deposited ECF (green) and splice regions, and (b) an in-fibre trough as implemented in Sec. 5.1.3, showing NP-ECF and bare ECF (blue) regions.

##### Strategy 1: Double-splice flow cell

The initial idea based on work conducted by [214] was to splice the ECF to a conventional single mode fibre (SMF) on either side in order to attain stable in-coupling conditions and easier integration with spectrometers etc. (see Fig. 5.10a). Splicing had not been carried out on the SC-MOF as the heat generated during the arc splice would be disruptive to the NP layers within the fibre. With the ECF however, NP immobilisation could be carried out directly on the core in the exposed channel without the need to access the full end facet, rather side accessibility was permitted. This meant NPs could be immobilised after splicing and layer damage avoided. Another reason the SC-MOF had not been spliced, to say a large core capillary, was that the core size and strand thickness were so fine (to the extent that even cleaving can induce damage) that it was understood a lengthy study on splicing conditions would have to be carried out to ensure core and strands survived. The ECF, conversely, had already been successfully spliced at larger core sizes (as in [232] where a 12.5  $\mu\text{m}$  ECF was spliced to an SMF, with a loss of 3 dB).

The concept is that by matching the mode field diameter of an input SMF with the ECF maximum coupling efficiency can be achieved and the splice loss minimised (not considering experimental factors such as any structural deformation upon heating, or splicer alignment tolerances). Light was coupled through an SMF section into the ECF, coupling efficiency maximised, the output mode inspected (as the ECF is multimode), and a splice made. The output power and mode were rechecked and then the ECF coupling to a second SMF section was optimised, spliced, and output rechecked. This integrated ECF region would then be encased in a flow cell (Fig. 5.10a), comprised of a



larger “flow chamber” silica capillary (1 mm inner diameter (ID)) hosting a smaller inlet capillary (150  $\mu\text{m}$  ID) connected to a syringe pump, and an outlet capillary (150  $\mu\text{m}$  ID). The entire length of the ECF would be sealed within the flow cell allowing deposition to be contained, and keeping the exposed-core surface as clean as possible (dust and contamination being a large problem with working with ECFs see Sec. 5.1.3).

In practice, splicing parameters are highly specific for each particular MOF geometry, so when splicing to a small-core (2.5  $\mu\text{m}$  diameter) ECF the likelihood of structural damage is far greater. In the work by [232] an SC-ECF (2.7  $\mu\text{m}$  core diameter, with thicker strand geometry than in this study) was achieved with splice loss of 16.5 dB. For the structure in this thesis, these parameters were not transferable for creating splices retaining fundamental mode transmission and sufficient intensity for LSPR detection.

### Strategy 2: In-fibre trough

Since the small fibre-core made splicing difficult, as an initial proof of principle an open trough system (as used during deposition Sec. 5.1.3) was deemed sufficient. Later for preliminary DNA analytics testing, a more measured chip flow approach (see Ch. 6) could be adapted. The intention was to exploit the ease of access of the exposed core channel by depositing precisely in a selected region. At first this was done using a small outer PTFE trough with a slit to mount the fibre (see Fig. 5.10b). In-coupling and transmission measurements could be taken as normal but the PTFE trough would contain a 1–2 cm midsection of the fibre. In this way various analytes could be pipetted into the trough and infiltrate the exposed fibre channel. The surface tension at the slit edges could prevent capillary forces from depositing further along the exposed core but this proved to not always be the case. This would not be a problem for NP deposition (even by mere evaporation for dry cutback method) except that the exposed core was so sensitive to surface contaminants that it immediately scattered noticeably at certain points (Sec. 5.1.3, [222]) – most likely points at which NPs or dust had clustered at the dried out meniscus point. To prevent the meniscus spreading within the fibre a low refractive index acrylate ( $n = 1.36$ ) was added under microscope to the exposed core at the points where the fibre exited the PTFE trough (indicated in Fig. 5.10b). These were cured under UV light and remedied the issue.

One advantage to keeping the exposed channel open and not continuing with a flow cell was the potential to conduct multiple depositions along it in periodic sections or in different section lengths. Furthermore it offers the possibility of plasmonic multiplexing by depositing NPs possessing different properties at various locations within the same ECF, i.e., functionalising different EC-regions to target different pathogen species detection, within one single device at the same time so that a sensor incorporating differently functionalised bands could be achieved. A comparison of the different optofluidic strategies tested is presented in Tab. 4, listing briefly the advantages and drawbacks of each approach.

Table 4: **Comparison** Optofluidic strategies investigated for SC-MOF and ECF systems

fibre type	solution	advantages	drawbacks
SC-MOF	PDMS chip	adjustable, low volume flow	delicate, poor fibre alignment
SC-MOF	OFM	robust, contained flow	longer samples required
SC-MOF	OFM butt-coupling	overcomes splicing and OFM lengths	time consuming construction
ECF	splice flow cell	contained, stable system	SC- splicing challenges
ECF	in-fibre trough	accessible core, analyte exchange	larger volumes, contamination possible

### 5.5 On-axis RI sensitivity measurements of plasmonic fibre systems

After verifying the NP attenuated plasmonic behaviour in transmission spectra, and after realising a stable, reproducible, optofluidic mounting strategy (Configurations B and C, Figs. 5.4 and 5.8 for ECF and SC-MOF respectively), solutions of different refractive index could finally be introduced to the MOF channels to check the integrated NP sensitivity in-fibre by tracking any shift in position of the attenuated LSPR peak.

#### SC-MOF

In determining the RI sensitivity of the NP functionalised SC-MOFs, a sample with NP density of 22 NPs/ $\mu\text{m}^2$  was first selected, offering a compromise between strong plasmon-waveguide mode interaction (i.e., short samples) and a handleable sample length of 1–2 cm.

Using the on-axis transmission measurement setup, the microstructures were pumped with a series of RI oils (Oil series AAA, Cargille Laboratories) via pressurised syringe pump. RI oils offer a larger range of precise RI analytes but require longer to rinse and are not appropriate for more delicate systems. Each individual RI oil was flushed through the optofluidic mount and fibre system (Sec. 5.3, Strategy 3: OFM with butt-coupling), until all air bubbles (observable on output camera) were eliminated.

Succeeding each spectral series, the system was rinsed with ethanol by repeatedly changing pump flow direction, and dried by inducing air bubbles, until remnants of the previous analyte were eliminated and the original spectrum reproduced.

For an exemplary sample (NP density of 22 NPs/ $\mu\text{m}^2$ ), Fig. 5.11a presents the series of RI measurements with the system exhibiting an increased wavelength of the transmission dip, Fig. 5.11c, with increasing analyte RI. This is the expected result of the NP LSPR shift towards longer wavelengths (from Mie theory). Linearly fitting the position of the transmission resonance dip for each spectral series value yields an RI sensitivity of 167 nm/RIU. This result lies within the typical range of spherical Au NP sensitivity values and is approx. 1.5 times higher than that obtained for the cross-axis, transverse probing of the same density of SC-MOF sample (Fig. 5.11b). It is also higher than the

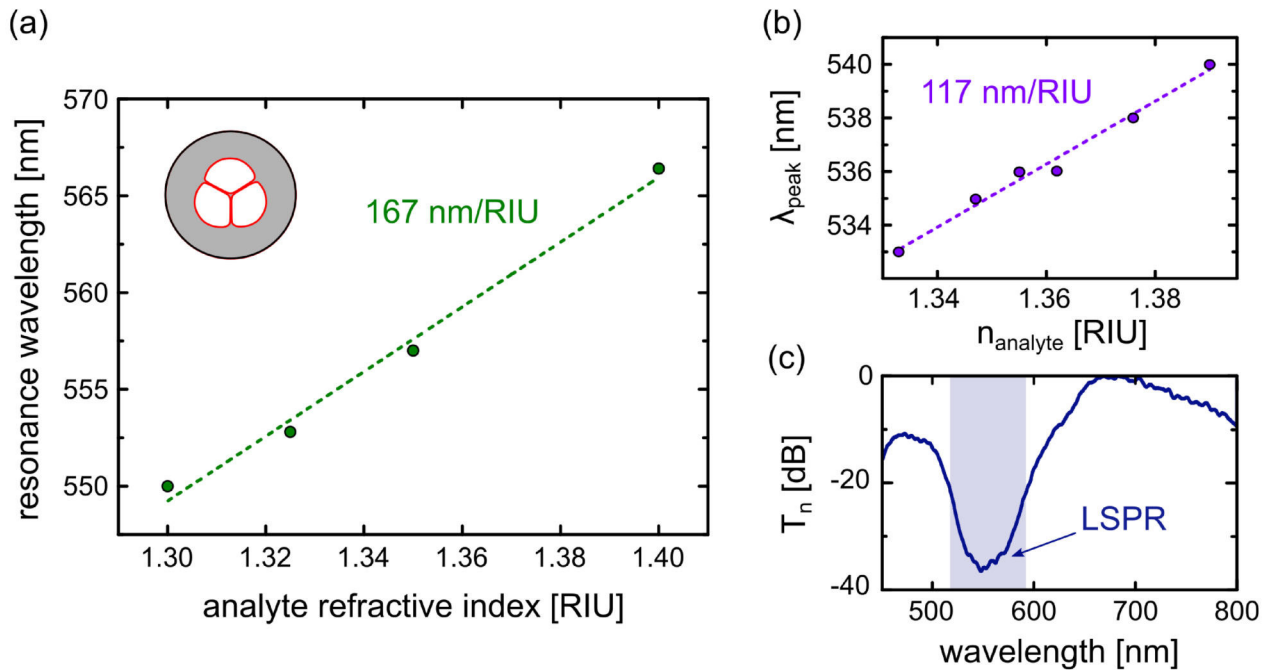


**Fig. 5.11:** (a) Experimental on-axis sensitivity of a plasmonic SC-MOF of 167 nm/RIU, determined from the slope of the resonance dip positions at each RI. Red indicates the location of NP deposition in the channels. (b) The bulk measurement sensitivity from the cross-axis setup is lower than that of on-axis at 117 nm/RIU. (c) An example of the measured LSPR dip, highlighted by the light blue region, with fringe contrast exceeding  $-20$  dB.

corresponding theoretically calculated RI sensitivity, 118 nm/RIU, calculated from Mie theory before applying a weighting factor correction for the presence of the substrate. This could be due to a different size distribution of the NP batch, a variation at the chosen cross axis sample points, or the contribution from four layers of NPs and silanes with the fibre strut geometry. Since in practice, the NPs are attached chemically to the silica surface, the theoretical value could further be improved perhaps by adding an aminosilane contribution to the calculation.

## ECF

For the exposed-core fibre case, conditions were different. In-fibre trough depositions were run until optical transmission measurements showed clear attenuated plasmonic behaviour. This was achieved for a much lower NP density but the sample lengths had the capacity for longer lengths. The example was taken of a sample with NP density ( $4 \text{ NPs}/\mu\text{m}^2$ ) on the surface of the core providing a well-defined transmission dip contrast of approximately  $-20$  dB at the wavelength of the LSPR (an example transmission spectrum is shown in Fig. 5.12c).

The RI sensitivity series was conducted in-fibre by pipette-filling the PTFE (and hence the in-fibre trough) with a glucose series, measuring, rinsing repeatedly with  $\text{H}_2\text{O}$ , and repeating. Here a glucose series was used to reduce rinsing cycles. By such procedure, the correlation between the analyte RI (at roughly the index of water) and the spectral distribution of the transmitted light was investigated. As in the previous SC-MOF sensitivity investigation, by a successive increase in the applied analyte RI, the LSPR spectral dip position was shifted towards longer wavelengths as the RI environment of the NPs

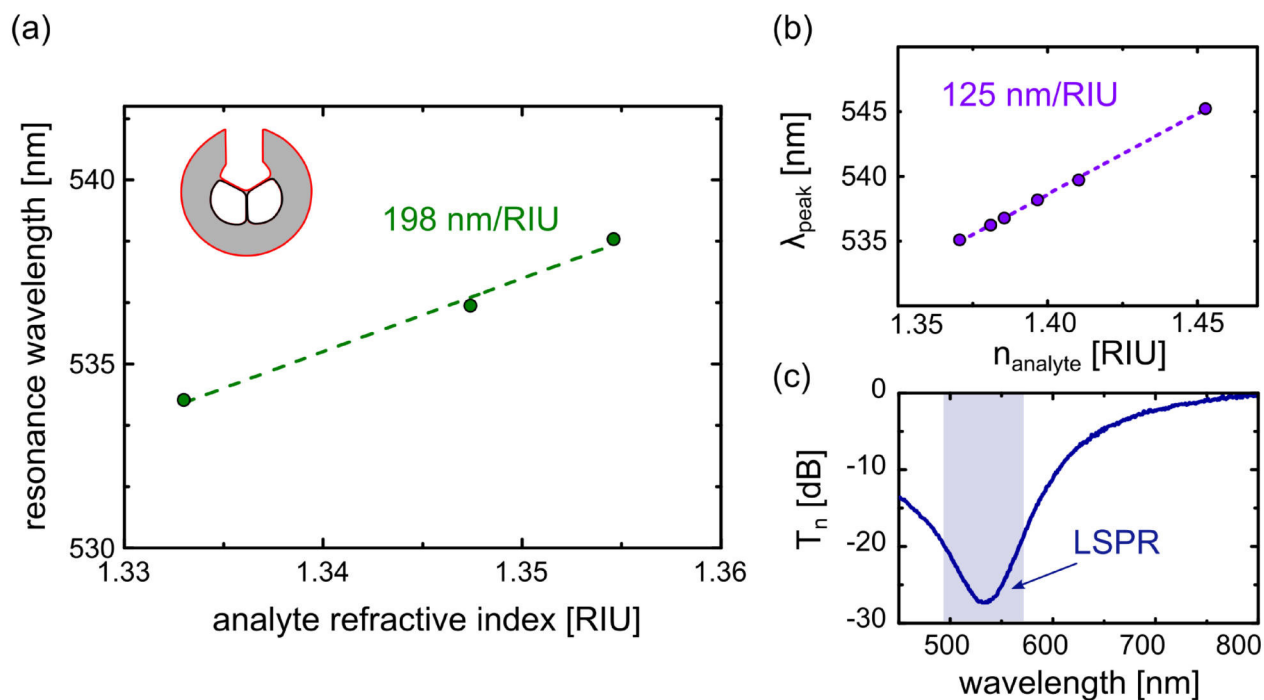


**Fig. 5.12:** (a) Experimental on-axis sensitivity of a plasmonic ECF sample yielding a value of 198 nm/RIU at roughly the index of water. Red indicates the location of NP deposition. (b) The corresponding theoretical sensitivity (125 nm/RIU). (c) An example of the measured LSPR spectral dip in the transmission spectrum (normalised to the transmission of an undeposited reference ECF). The plasmon-induced transmission drop is highlighted by the light blue region and exhibits as well-defined transmission spectrum dip yielding fringe contrast of approximately  $-20$  dB.

increased. The overall RI sensitivity in the proximity of the index of water was found from a linear plot of data to be 198 nm/RIU (Fig. 5.12a).

The system's theoretical sensitivity was investigated by finite-element simulations, involving changing the RI in the open channel, which yielded a bulk sensitivity value of 125 nm/RIU (Fig. 5.12b). This theoretical sensitivity is itself higher than that of bulk NPs immersed in solution and slightly lower than the measured experimental value of 198 nm/RIU. Factors that could influence the NP sensitivity include aggregation, changes to the NP shape (for instance non-spherical NPs reverting to spheres), or NP interaction at high densities. However, SEM images indicated homogeneous, low-density nanosphere layers, with UV-VIS spectrophotometry confirming expected resonance peak positions. This difference is therefore attributed to the fact that while the fibre substrate effect was included, the PDDA bonding layer was not considered in the simulation.

### Detection outlook

Both MOF strategies presented demonstrate comparable sensitivity – although their core sizes and NP batches differ. The SC-MOF yielded 167 nm/RIU and the ECF 198 nm/RIU; both values which are higher than bulk solution and their theoretical predictions. The resulting values of FOM for the SC-MOF and ECF systems are 1.491 and 1.626 RIU<sup>-1</sup> respectively – also higher than theory (Ch. 2.2.5, Tab. 1) due to the increased sensitivity. The lower FOM value for the SC-MOF is expected from the lower NP size but could also be due to the effect of three channels of NPs, offering greater potential for peak

broadening (for instance due to a site of inhomogeneity with one channel), rather than one as with the ECF. The ECF permits the use of an order of magnitude lower NP density coverage to viably observe RI-induced LSPR spectral shifts. With its marginally smaller core size providing lower  $A_{\text{eff}}$  values, and larger NPs allowing slightly higher sensitivity, a 31 nm/RIU greater sensing performance is permitted. Additionally, the ECF permitted increased overall sample length, thereby improving device handling, and a tailorable deposition length and location along the core – offering a monolithic type device.

Considering the minimum resolvable shift is approximately 0.1 nm, the limit of detection (LoD) here is  $5 \cdot 10^{-4}$ , which could be improved, e.g., by a better spectrometer resolution, employing more RI sensitive NPs (e.g., nanoprisms, or core-shell spheres [53,97]), added temperature stability, or improved data analysis. Although applying the plasmonic MOF systems as DNA sensors was not part of this work, initial estimations and strategies can be made towards developing this. Using the experimentally derived sensitivities of this chapter, the expected DNA induced shifts for the two systems can be calculated. The case of 24 base pairs aligned vertically on a NP surface yields a layer thickness of 8.16 nm. Changing the NP's environment from water to the RI value of DNA ( $n_{\text{DNA}} = 1.362$ , as calculated from [79]) induces corresponding shifts of 4.88 nm and 5.79 nm for the SC-MOF and ECF systems respectively.

#### Chapter summary

- Optical characterisation showed clear LSPR excitation evident in the transmitted modal spectrum of both functionalised MOF systems.
- The attenuation for low sample densities, investigated through cutback method, was in line with modal attenuation calculations.
- A range of strategies for optofluidic sensing on the two systems was studied, with an OFM butt-coupling approach implemented for the SC-MOF and an in-fibre trough method for the ECF.
- Sensitivities for both systems outperformed predictions and indicated detectable, ssDNA-induced resonance shifts of 4.9–5.8 nm.

After verifying the successful immobilisation of NPs within microstructured fibres and using these plasmonic systems experimentally for refractive index sensing, an initial investigation was run to test the system's applicability for DNA plasmonic sensing. The following chapter is a preliminary study on the utility of the realised system as a DNA biosensor. Since planar NP-DNA sensing is an existing established field, the first step was to investigate the NPs within a microfluidic planar setup with sufficient detection sensitivity. A pre-existing ensemble LSPR setup allowed real time monitoring of the signal modifications from immobilised NPs with changing environment and functionalisation. Thereby, the NPs were functionalised with ssDNA capture probe (creating a planar biosensor), hybridised with complementary target DNA (proving successful biosensing), dehybridised and reused. A fungal species, *Aspergillus spp.*, sequence was implemented (as in [79]) for this purpose. Each of these steps was observed to exhibit distinct spectral change in the LSPR peak position. In order to ensure a substantial binding shift and promote ease of detection, the capture DNA strand was further functionalised with a 5 nm gold nanosphere to enhance signal [79]. After ensuring the microfluidic pumping process, NP functionalisation, and detection aspects were operationally viable, initial steps to incorporate a plasmonic ECF into the chip setup were established. The primary considerations in this chapter include:

1. Do the gold NPs provide sufficient sensitivity experimentally for DNA detection?
2. Can a specific, reproducible DNA target capture experiment be performed?
3. How can the setup be adjusted towards an initial proof of concept of the sensing system?

### 6.1 Concept of "ensemble of nanoparticles" LSPR characterisation

Owing to the spectral LSPR dependence on the NPs' composition and local RI environment, the opportunity exists to exploit this sensitivity to surrounding media and implement NPs as label-free bioanalytical sensors. A range of biomolecules [233] can be directly bonded to the NP surface in a functionalisation step. This results in an LSPR resonance wavelength shift detectable by absorbance spectroscopy, which is the key to using NPs in bioanalytical diagnostics.

"Ensemble" LSPR, eLSPR, provides a means to access simultaneously the response of a number of NPs in a local area. This offers a statistical averaging effect of measurement in comparison to single particle measurements. The eLSPR characterisation consists of a microfluidic chamber hosting a dense NP-coated glass substrate and a DNA protocol for in situ, real time, kinetic spectroscopic measurements.

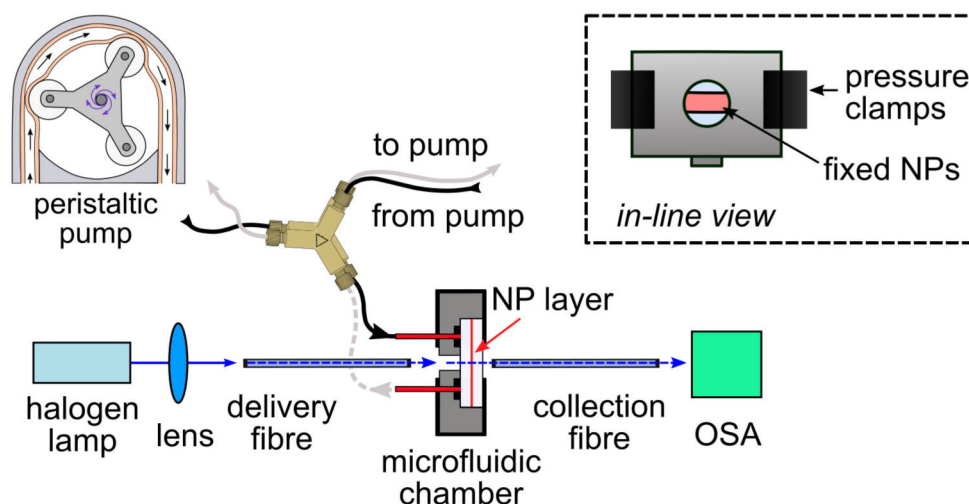


**Fig. 6.1:** eLSPR measurement setup detailing light path, pump system, and microfluidic test chamber.

### 6.1.1 Setup configuration for eLSPR

The eLSPR measurement setup [79,234,235] (as in Fig. 6.1), comprised of: a halogen light source (HL-2000-FHSA from Ocean Optics, USA), delivery and collection optical fibres, a microfluidic chamber (as deconstructed in Fig. 6.2), an Ocean Optics USB2000+ spectrometer, and a microfluidic delivery system with a peristaltic pump (Ismatec Reglo ICC, IDEX, Lake Forest, IL) – enabling gold NP biofunctionalisation with capture DNA and the subsequent binding of target DNA, under continuous flow conditions. Input light was delivered to the central region of the microfluidic chamber via delivery fibre, and collected at the output by an identical fibre attached to the spectrometer. Initial dark current and light source measurements are run prior to NP chip inclusion to the chamber. Following chip insertion, NP extinction spectra are measured continuously (a spectrum recorded every 2 s), allowing for a real-time trace of LSPR peak position and detection of any subsequent shifts. This continuous spectral measurement enables monitoring of the biosensor preparation steps (i.e., NP functionalisation with a receptor/capture molecule possessing specific binding to a target molecule) in addition to the subsequent biosensing process (detection of the analyte molecule), thereby allowing access to kinetic information. Online detection was implemented via a custom built LabView program (LabView 8.6), and post-measurement data analysis implemented through an in-house Matlab software (Matlab 7.1), both provided by [79, 234]. The LSPR spectral centroid is determined as in [236], in order to minimise peak position noise.

### 6.1.2 Chip design and integration with microfluidics

Analytes were introduced under specific flow rates (see Tab. 5 and Sec. 6.3) to the chamber by means of a peristaltic pump controlled by LabView parameters. Also crucial to the chamber flushing process was a double T junction, microfluidic valve connect, enabling injection of alternating solutions to the chamber without dead volume or time (Fig. 6.1).

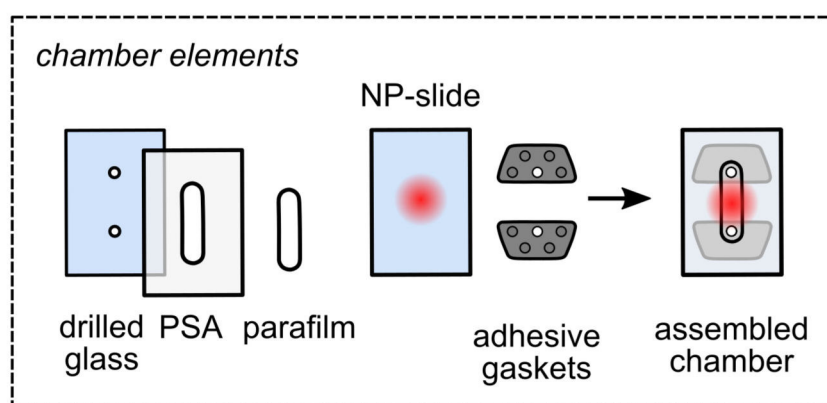


**Fig. 6.2:** Chamber design for planar eLSPR measurement. Included are: a glass slide with immobilised NPs (red spot region), drilled glass and adhesive gaskets for microfluidic connection, parafilm sealant ring, and a pressure sensitive adhesive film (PSA, Adhesives Research, ARcare<sup>®</sup> 92712) to contain liquid flow and seal the chamber. Clamps were further attached to the assembled chamber to provide pressure and prevent leakage.

The microfluidic chamber design had been created for pre-existing in-group investigations. In order to construct it, a glass slide ( $35 \times 16$  mm) with drilled in- and outlet holes was used, along with adhesive foil layers (as in Fig. 6.2). The foil layers were pressure sensitive and enabled the biosensor chip with immobilised NPs to be sandwiched against it to prevent leakage. The structure was also clamped on both sides for added pressure and inserted into an adjustable mount for in-coupling. The glass slides involved were treated prior to chamber assembly with the same cleaning process as the biosensor slide (Sec. 6.2). The final chamber construction was approximately  $100 \mu\text{m}$  in width with  $7 \mu\text{l}$  inner volume.

## 6.2 LSPR planar biosensor preparation

Cut microscope glass slides (VWR International) were cleaned by a sequence of: hand cleaning with rinsing agent; ultrasonication in acetone, in Rotisol<sup>®</sup> (Carl Roth GmbH), in ethanol, and then in ultrapure  $\text{H}_2\text{O}$ . Following this, the slides were exposed to oxygen plasma etching for 1 hour at 380 W and 1.6 mbar. To promote gold NP adhesion to the glass surface, the surface affinity could then be enhanced by amine surface group functionalisation through incubation with 1% APTES, (3-aminopropyl)triethoxysilane, (Sigma-Aldrich GmbH) in 1 mM acetic acid for 10 minutes, and ultrasonication with  $\text{H}_2\text{O}$ . To facilitate proof of principle measurement, the NP size and sensitivity was increased by incorporating 80 nm gold nanospheres. Gold nanosphere solution (British BioCell International) was centrifuged at 8000 rpm for 6 minutes, the supernatant removed, and  $20 \mu\text{l}$  of NP solution pipetted onto the centre of the treated glass chip. This centrifuged solution could be re-suspended with deionised water according to density preferences, e.g. 1 : 10 for low density, single NP measurements under optical microscope. The NP solution was incubated for 1 hour before rinsing the chip with ultrapure  $\text{H}_2\text{O}$  and drying with nitrogen.



### 6.2.1 LSPR chip characterisation and bulk RI planar measurement

Immobilised NPs on the glass chip could be inspected for homogeneity using an optical microscope – Axio Imager Z1m (Carl Zeiss Micro-imaging, Göttingen, Germany) with a tungsten halogen lamp as a continuous broadband light source – operating in dark-field mode as in [42,132]. The chip surface density could also be inspected using UV-VIS spectrophotometry, Scanning Electron Microscopy, SEM imaging, or Atomic Force Microscopy, AFM. Under visual inspection (and depending on the density deposited), the NP functionalised chips display a uniform red colour over their deposited area ( $\sim 0.5 \text{ cm}^2$ ).

The NP functionalised chips could then be incorporated into a microfluidic chamber (as described in Fig. 6.2) and optically characterised. Experimental spectra of NP extinction and scattering could be compared to Mie theory [143], with resonance position obtained as in the experimental case – using the centroid position [236].

A bulk sensitivity value for the system could be ascertained by measuring the resonance shift under RI values between 1.33 and 1.43. For 80 nm Au NPs this amounted to a sensitivity of 104.46 nm/RIU – in good comparison to theoretical calculation (Tab. 1). Sensitivity is seen to be higher for these larger diameter NPs, as indicated from theory. From the peak position variation over time the lowest detectable  $\Delta n_{\text{eff}}$  is determined to be better than  $10^{-4}$  RIU.

## 6.3 DNA deposition and hybridisation detection on planar structure

The NP functionalised chip was applied to the chamber in the eLSPR setup and subsequently connected to the peristaltic pump. If the chip was not freshly prepared it was cleaned by oxygen plasma etching for 10 s at 1.6 mbar and 380 W. The microfluidic chamber was then mounted and aligned and a measurement flow assay was conducted at a flow rate of 10–20  $\mu\text{l}/\text{min}$ . Previous work in the Nanobiophotonics Group IPHT had provided workflow assay protocols taking into account: comparison studies to other buffers' [237] baseline stability, the effects of plasma etching, ideal capture/target DNA concentration, spacer lengths, and regeneration approaches. One of these workflows, as detailed below, was adopted for the purpose of this investigation. The necessitated volumes of the solutions used depended on the microfluidic chamber volume, tube diameters and flow rates.

The first assay steps 1–8 detail the creation of the LSPR-DNA biosensor, steps 9–12 detail the biosensing of target DNA species, and steps 13–16 show evidence of the reusability of the system. These step groups will be explained in the following subsections. In an effort to minimise measurement uncertainty in the resonance peak position, five repetitions were performed at each measurement step and averaged. The peristaltic pump was run at 20  $\mu\text{l}/\text{min}$  for washing steps, and at 10  $\mu\text{l}/\text{min}$  for adsorption steps. The dilution and running buffers must be the same to prevent impeding the measurement with a refractive index change.

The biosensing workflow procedure is as follows:

1. 10 min washing with citrate buffer, CB, and spectral measurement under continuous CB flow
  2. 10 min injection of 5  $\mu$ M thiolated *Aspergillus spp.* capture DNA (in CB)
  3. 5 min washing with CB
  4. 5 min washing with running saline sodium citrate buffer 5 $\times$ SSC
  5. 15 min injection of a 1  $\mu$ M, 6-mercapto-1-hexanol, MCH, solution in 5 $\times$ SSC (coadsorption)
  6. 10 min washing with 5 $\times$ SSC
  7. 15 min injection of 100  $\mu$ g/ml salmon sperm DNA, LSFD, in 5 $\times$ SSC (surface blocking)
  8. 10 min washing with 5 $\times$ SSC + spectral measurement under continuous 5 $\times$ SSC flow
  9. 20 min injection of 1  $\mu$ M non-target *Candida spp.* DNA functionalised with 5 nm particles (in 5 $\times$ SSC)
  10. 10 min washing with 5 $\times$ SSC + spectral measurement under continuous 5 $\times$ SSC flow
  11. 20 min injection of 1  $\mu$ M complementary *Aspergillus spp.* DNA labelled with 5 nm NPs (in 5 $\times$ SSC)
  12. 10 min washing with 5 $\times$ SSC + spectral measurement under continuous 5 $\times$ SSC flow
  13. 10 min injection of 10 mM HCl (sensor regeneration)
  14. 10 min washing with 5 $\times$ SSC + spectral measurement under continuous 5 $\times$ SSC flow ( $\rightarrow$  8)
- After step 13, the protocol could be repeated starting from step 8 for other DNA sequences. Upon sensor regeneration, the array was incubated again with NP-functionalised *Aspergillus spp.* target DNA sequence and spectrally measured.
15. 20 min injection of target DNA sequence labelled with 5 nm particles
  16. 10 min washing with 5 $\times$ SSC + spectral measurement under continuous 5 $\times$ SSC flow ( $\rightarrow$  14.)

A complete table and spectral measurement procedure corresponding to the workflow assay is contained in Tab. 5 and Fig. 6.3.

Table 5: **Workflow** Fluidic pumping protocol as implemented in the eLSPR system. The use of left, L, and right, R, pumping channels helps prevent air bubbles and dead volumes. The resulting spectral behaviour of the system is plotted in Fig. 6.3

duration [s]	channel L [ $\mu\text{l}/\text{min}$ ]	solution in L	channel R [ $\mu\text{l}/\text{min}$ ]	solution in R	chamber R/L	volume L [ $\mu\text{l}$ ]	volume R [ $\mu\text{l}$ ]
900	3	5 $\mu\text{M}$ capture	10	CB	R	45	150
900	10	5 $\mu\text{M}$ capture	3	CB	L	150	45
300	10	5 $\times$ SSC	3	CB	L	50	15
300	10	5 $\times$ SSC	3	MCH in 5 $\times$ SSC	L	50	15
900	3	5 $\times$ SSC	10	MCH in 5 $\times$ SSC	R	45	150
300	10	5 $\times$ SSC	3	LSFD in 5 $\times$ SSC	L	50	15
900	3	5 $\times$ SSC	10	LSFD in 5 $\times$ SSC	R	45	150
300	10	5 $\times$ SSC	3	Non-target with NP	L	50	15
1200	3	5 $\times$ SSC	10	Non-target with NP	R	60	200
300	10	5 $\times$ SSC	3	Target with NP	L	50	15
1200	3	5 $\times$ SSC	10	Target with NP	R	60	200
600	10	5 $\times$ SSC	3	10 mM HCl	L	100	30
600	3	5 $\times$ SSC	20	10 mM HCl	R	30	200
600	10	5 $\times$ SSC	3	Target with NP	L	50	15
900	3	5 $\times$ SSC	10	Target with NP	R	60	200

### 6.3.1 Biofunctionalisation of immobilised gold nanospheres

The immobilised gold nanospheres were biofunctionalised with thiol-modified single-strand, ssDNA, i.e. capture DNA. As outlined in Ch. 2.4, thiols have a particularly high affinity to gold. The adsorption of the thiolated ssDNA induces a wavelength shift of the LSPR peak, typically of 2–3 nm (2.5 nm in the spectrum in Fig. 6.3), in the adsorption spectrum. This entire procedure was undertaken in a 500  $\mu\text{M}$  citrate buffer pH = 3.0 [188].

Single-strand DNA may also adsorb along its strand to the gold NP surface, thus hindering binding access for the complementary target DNA and lowering hybridisation efficiency. In order to minimise this effect, coadsorption with a short alkanethiol, MCH, was implemented. By binding of its own thiol terminal group to the gold NP surface, this molecule covered and blocked the remaining NP surfaces, thereby decreasing unspecific binding along the DNA strand and promoting maximal accessibility for hybridisation with the target DNA. In this way, the NP surface was passivated against the nonspecific adsorption of DNA (along the strands) and the hybridisation yield was optimised.

Unspecific binding of DNA elsewhere in the chamber also needed to be minimised and this can be achieved through incubation with short-strand herring or salmon sperm DNA, which similarly blocked the remaining surfaces.

### 6.3.2 Biodetection of target DNA samples and control

Once the biosensor chip was achieved, complementary target ssDNA in running buffer (5 $\times$ SSC) was introduced until the signal reached a plateau and demonstrated maximum resonance peak wavelength shift; typically 15 minutes. Binding with the complementary strand typically yields a slightly lower shift in the signal peak wavelength; within

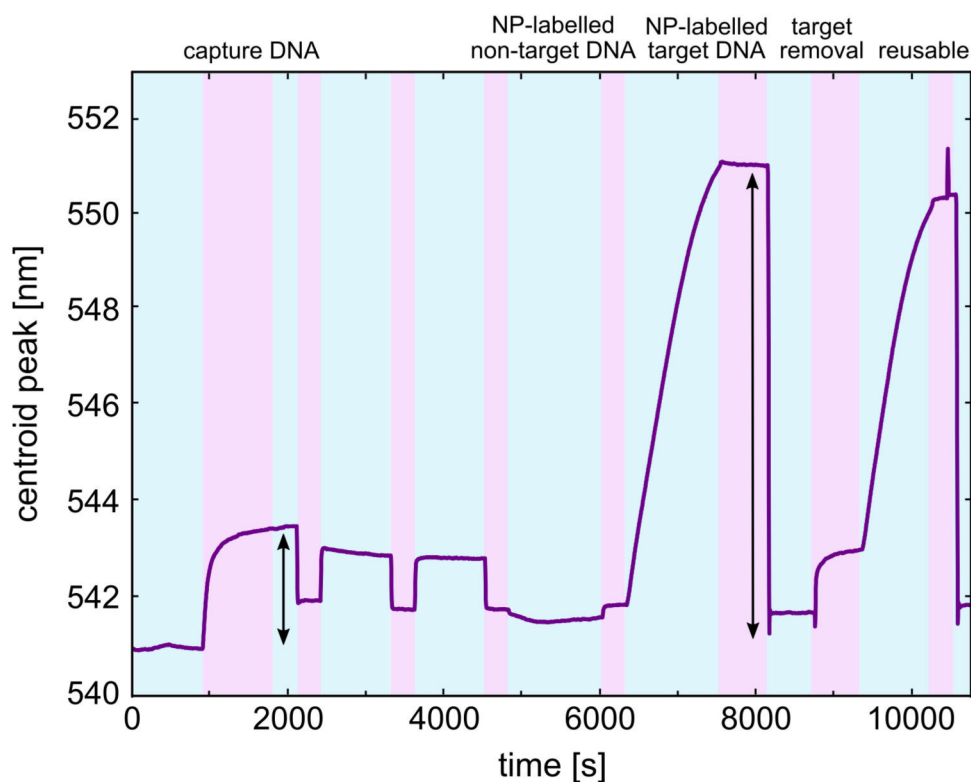


**Fig. 6.3:** Demonstration of DNA detection and LSPR shift, using planar substrate, following the workflow procedure outlined in Tab. 5. The LSPR peak shifts correspond to analyte changes occurring at different times, with the binding-event induced shifts from capture and target ssDNA indicated by double-sided arrows (2.5 and 10 nm shifts respectively).

the 1–3 nm range. In this case the target DNA strand was functionalised with a small 5 nm gold nanosphere which enhanced binding signal to 7–12 nm. Fig. 6.3 indicates an induced shift of 10 nm upon introduction of the functionalised target strand. This shift was not observable when another non-target DNA strand (also labelled with a 5 nm gold nanosphere) was introduced prior to the target species. This demonstrates the specificity of the technique.

### 6.3.3 Regeneration of sensor post-hybridisation

Assay steps 13–16 demonstrate the regeneration and reusability of the system. Flowing HCl through the sensor is one way of destroying the base pair hydrogen bonds and dehybridising the strands. Thus the target DNA is specifically removed but the capture DNA remains thiol bonded to the gold and available for further hybridisation. This fact is shown by running the next detection, step 15, where a 10 nm peak shift once more occurs upon binding with the NP-labelled complementary DNA strand, indicating the biosensor remains intact and reusable (Fig. 6.3).

## 6.4 DNA deposition and hybridisation detection on ECF structure

Following this investigation into NP-DNA sensing on planar chip, a subsequent application to the fibre geometry was considered.

The primary benefit offered by incorporating the eLSPR setup towards a proof of principle investigation was the pre-existing workflow assay protocols, coupled with the

controlled flow rates and volumes the setup presented, which would not have been immediately available to the fibre-in-trough layout. A considerable amount of time and a further study would have been needed to design and implement a corresponding level of control on the pure fibre system. The available microfluidic chip enabled thorough rinsing and precise injection of DNA steps in a contained, enclosed environment, the likes of which could later be begun to be incorporated on-fibre. The NPs used throughout this work for optical fibre measurements (Ch. 5) were of diameters 34 and 45 nm. In theory, given an 8.16 nm thick DNA layer (estimated to be the strand length of 24 bases) of RI:  $n_{\text{DNA}} = 1.362$  (calculated as in [79]), these NP sizes should induce capture DNA shifts of 1.79 nm and 2.11 nm respectively. Using the sensitivities recorded experimentally for the plasmonic fibre systems however, shifts of 4.88 nm and 5.79 nm are expected Tab. 6. The subsequent binding target DNA event should induce a slightly reduced shift (due to its further distance from the NP surface). These values are detectable both by the eLSPR system and by the optical fibre transmission measurement system.

However, to further facilitate measurement the NP size was increased by incorporating 80 nm gold nanospheres in the flow chamber. The larger NPs offered higher NP sensitivity and thereby system sensitivity, and increased the surface area available for DNA binding events. These were expected to provide a capture DNA shift of 3.19 nm. In order to enhance these values even further, the target DNA was functionalised with a small gold nanosphere, raising the complementary binding to 10 nm (Fig. 6.3). The calculated ssDNA induced shift values are summarised in Tab. 6 for the different NP sizes and systems used.

Table 6: **Predictions** ssDNA induced LSPR shift calculated for the case of a 24 base pair, 8.16 nm ssDNA layer with an RI of 1.362 in water environment. Values are given based on theoretical calculations of NP-on-substrate sensitivity,  $S_{\text{NP}}$ , and experimentally acquired sensitivity,  $S_{\text{MOF}}$ , of the SC-MOF system with 34 nm NPs and the ECF system with 45 nm NPs. \* refers to experimental NP-on-planar substrate sensitivity.

NP dia. [nm]	theory $S_{\text{NP}}$ [nm]	experimental $S_{\text{MOF}}$ [nm]
34	1.790	4.883
45	2.112	5.789
80	3.187	3.054*

The most direct approach to applying this on-fibre involved adding the fibre directly to the microfluidic chamber and rotating the system to lay parallel to the optical table (Fig. 6.4). The fibre could be in-coupled from the supercontinuum laser (as used in Ch. 5) to excite the fundamental core mode and out-coupled to the spectrometer and analysis program. The microfluidics remained unchanged. The greatest challenges in integration involved preventing fibre breakage under pressure and at the sharp chip edges, preventing chamber leakage, and optimising analyte flow with an incorporated ECF. The chip was placed in an oxygen plasma etcher prior to fibre insertion, in order to remove organic adsorbates – decreasing surface roughness and contact angle – and reduce bubble

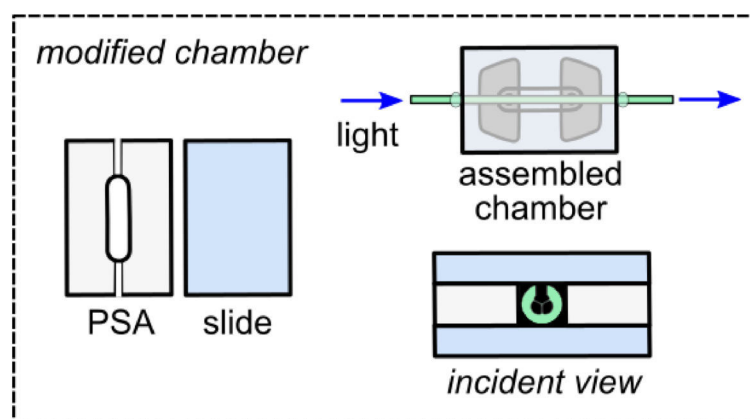


**Fig. 6.4:** Modified eLSPR chamber design including ECF mounted parallel to flow direction.

zone formation. Sections of the interior adhesive foil region were removed by scalpel to form a channel in the foil in which the fibre could sit, greatly aiding in aligning the fibre within the chip (Fig. 6.4). The in-fibre trough length was also extended to the distance of the boundary edge of the flow chip. In this manner leakage from the ECF end faces and the microfluidic chamber were avoided, as well as breakage within the chip, yet considerable vigilance was still required to keep the fibre sample intact. Leakage checks were run separate to guidance by implementing different flow rates of H<sub>2</sub>O over time periods of hours. Guidance and plasmonic response was also verified on the optical transmission setup (as in Ch. 5) with the ECF incorporated in the flow chip. Finally simultaneous guidance with pumping was confirmed.

As of yet however, this setup configuration has not been implemented for a full DNA detection in the eLSPR setup. This is largely due to the highly challenging production required for one 'NP-functionalised fibre-in-chip', which includes:

- Depositing and transferring the NP-in-fibre trough. As discussed in (Ch. 5.1.3, Ch. 5.4, [222]) the ECF is extremely sensitive to surface contaminants such that it scattered noticeably at certain points during experiments often leading to severe attenuation and the need to discard that sample in favour of a new one. The deposition procedure developed in this work requires the microscope application of a low refractive index acrylate ( $n = 1.36$ ) to create an in-fibre trough in the exposed ECF channel. This is then cured under UV light before applying a PE layer deposition and finally Au NPs. Further handling and exposure of this fibre is not advisable – transporting it in a box under argon between optical setups minimised additional attenuation.
- Fabricating the modified microfluidic chip system and incorporating the plasmonic fibre. The flow chamber fabrication while done by hand was merely time consumptive. The greatest challenges in integration involved inserting the deposited ECF without damage or contamination. Preventing fibre breakage under pressure and at the sharp chip edges was an issue due to the fragile exposed-core channel of this fibre geometry. It was entirely possible to insert this fibre successfully only to discover core damage later during the fluidic stage of investigation.

- Preventing microfluidic chamber leakage, and optimising analyte flow with an incorporated ECF. The modified microfluidic chamber design created in this initial investigation was quite straightforward, as in Fig. 6.4 – the fibre was aligned directly beneath the inlet and outlet tubes. However optimising the analyte flow through the chamber and along the fibre would involve an entirely separate microfluidic study in order to optimise flow rates and direction for deposition. The flow rate should be sufficiently low for DNA and chemical incubation but high enough to exchange the analyte in the entire chamber in minimal time. The analyte in the fibre channel should be entirely exchanged without bubble formation or layers remaining bound at the channel curvature. However the flow rate should not be so high as to damage deposition on the fibre channel – which may necessitate a repositioning of the fibre sample. The surfaces were treated by plasma cleaning to avoid bubble sticking and mechanical pressure applied to prevent external chip leakage. These measures were however not always sufficient and once a leak occurred the fibre could not survive reopening the microfluidic chamber without damage, neither could a full sensing experiment be conducted as the analytes could not be thoroughly flushed through the system at each step.

In order to circumvent these issues, homogeneous NLD depositions were run with the ECF in situ within the chamber but transmission was ultimately attenuated before the binding events could be detected. Deposition was achieved, but due to the extra volume within the chamber once sufficient signal attenuation was observed and deposition pumping ceased, the remaining colloidal solution within the cell continued to deposit leading to high densities and over attenuation of the signal.

In full the steps required involve: depositing the NP-in-fibre trough, fabricating the modified flow chamber, inserting the plasmonic fibre, proving coupling and plasmonic response in the optical transmission setup, checking for leakage, transferring the system to the eLSPR setup, preparing workflow chemical solutions, and finally running the experiment. If the fibre is damaged, or the core transmission is otherwise attenuated (Ch. 5.1.3) during this time, a new sample preparation is required. Only after achieving all of the above steps including optimising the microfluidic design and pressure parameters, can a DNA plasmonic fibre sensor be demonstrated. In theory this can be accomplished but it is beyond the scope of this study and a considerable amount of time and further refinement is required for the design and implementation necessary to show the entire functioning system.

### Chapter summary

- A preliminary plasmonic DNA sensing investigation for *Aspergillus spp.* sequence on planar substrate was conducted using an eLSPR system.
- Au NPs can be functionalised post-deposition with ssDNA-modified thiol groups. After hybridisation with target DNA, the DNA can be denatured – the NP remains bound to the surface, the thiol-modified capture strand remains bound to the NP – and the system can be reused.
- 80 nm Au nanospheres were implemented for greater resonance shift, yielding RI sensitivity on-chip of 104.46 nm/RIU – closely comparable to the theoretical predictions from Tab. 1.
- Theoretically this NP system offers a shift of 3.05 nm upon coverage with ssDNA. However, the target DNA can be functionalised with a 5 nm Au NP – experimentally increasing the binding induced shift to 10 nm.
- An initial strategy for modifying the microfluidic chamber to incorporate an ECF system was investigated.



## CONCLUSION AND FUTURE PROSPECTS

---

In summary the objective of this work to combine small-core microstructured optical fibres with label-free NP-based analyte sensing was achieved, and preliminary work towards application in pathogen sensing was additionally explored. An in-depth study of plasmonic NP deposition within microstructured fibres and on their exposed-core relatives was conducted along with their subsequent optical characterisations. The concept of SCFs harbouring immobilised plasmonic Au NPs surrounding their guiding core was realised, yielding an entirely integrated optofluidic platform for efficient RI sensing. The NP functionalised fibres were seen to exhibit clear LSPR behaviour in their output transmission spectra corresponding to the deposited NP species. This observation validates the use of NP functionalised fibre platforms for biosensing application. The small core geometries implemented were studied for maximising the available modal scattering area and by extension the potential for sensing lower NP concentrations. They were observed to experimentally perform well as evanescent field sensors, converting changes in the NP LSPR spectra from microstructure analyte exchange to characteristic traceable transmission behaviour.

### SC-MOF

For the case of the SC-MOF, the extremely small optical core size and large adjacent microstructures acting as microfluidic channels, allowed access to over two orders of magnitude of Au nanosphere coverage density. The small suspended “nanowire” core was in direct contact with the fixed NPs and analytes over several centimetres. This permitted an intense plasmonic interaction with the propagating mode, enabling the investigation of sparse as well as very high density particle ensembles. Various NP densities were targeted and deposited successfully and the corresponding modal attenuation compared well with the analytic model predictions. Furthermore, directly immobilising the NPs within the silica fibre microstructures resulted in a reusable sensing system. The core – which is incidentally the smallest evidenced in literature for NP immobilisation – being entirely encapsulated within the fibre, offered superior handling properties in comparison to freely-suspended waveguide systems, for instance tapers.

An optofluidic strategy was devised to perform analyte infiltrated measurements. The resulting sensitivity of these new plasmonic sensors was determined by analyte filling with an RI series to be 167 nm/RIU, for the example of functionalisation with 34 nm diameter gold nanospheres (22 NPs/ $\mu\text{m}^2$ ), and using sample lengths in the millimetre range. This proved to be a value 1.5 times higher than that of “cross-axis” measurements taken transverse to the fibre core, and to sensitivity values of bulk NPs in water [56].

### ECF

Prior to this study the ECF geometry in particular was largely unstudied with regard to plasmonic sensing. It had been implemented in a small number of cases as a fluorescence

sensor [103, 238], an interferometric biosensor [214], and more recently for analysing the properties of propagating surface plasmons [122] and for tunable third-harmonic generation [107, 239].

This work deposited NP ensembles within tailored, predefined regions on the open channel and fibre core. This yielded a monolithic, highly sensitive RI plasmon-based sensor that allowed for quick, reliable detection of small RI variation. Various deposition strategies were explored including vapour phase aminosilane deposition and using a double-splice flow cell for NLD. In the end the deposition of Au nanospheres (45 nm diameter) was achieved by means of polyelectrolyte layer deposition. The NP ensemble density was thereby controlled electrostatically and deposited over lengths of 2 cm within the exposed core channel of longer sample lengths (typically 15 cm ECF).

The ECF core implemented had a diameter of 2.5  $\mu\text{m}$ , akin to the SC-MOF, which similarly enabled strong interaction of surfactants with the propagating mode. Comparably low NP densities were targeted with the case of an ensemble density of 4  $\mu\text{m}^2$  demonstrating a pronounced LSPR dip with fringe contrast of approximately  $-20$  dB. RI sensitivities of 198 nm/RIU were observed at this NP density; a value 1.9 times higher than the corresponding value for bulk NPs in solution [106]. Compared to finite-element simulations with RI variation in the exposed channel (indicating a sensitivity of 125 nm/RIU without substrate correction), the theoretical sensitivity was larger than that of bulk NPs in solution and slightly below that of the experimentally measured value. This offset was attributed to not including possible PEL layer contributions. The system's limit of detection was evaluated as  $5 \cdot 10^{-4}$ , which is improvable, e.g., by using NPs with greater RI sensitivity (e.g., nanoprisms [97]), better spectrometer resolution, added temperature stability, or improved data analysis.

### System comparison

Comparing both SCF systems (although the cores are not identical nor are the NPs) the ECF strategy demonstrates comparable sensitivity to the SC-MOF, but permits the viable detection of RI-induced resonance shifts using an order of magnitude lower NP density. Specifically, the functionalised SC-MOF demonstrated a sensitivity of 167 nm/RIU for 34 nm spheres with density 22 NPs/ $\mu\text{m}$  (sample length: 3 mm); the functionalised ECF a sensitivity of 198 nm/RIU for 45 nm spheres with density 4 NPs/ $\mu\text{m}$  (sample length: 2 cm). A 2 cm long deposition segment with density lower than 8 NPs/nm using the SC-MOF structure would not have induced a usable LSPR effect on the fibre transmission. Such low density plasmonic SC-MOF was typically cutback from much longer lengths without approaching comparable fringe contrast.

In one respect device handling was improved by implementing the ECF. Since the overall fibre length could be significantly increased, while the NP functionalised core length could be tailored separate to this, a monolithic-type fibre device was achievable. On the other hand the exposed-core nature of the ECF made contamination and fragility an issue that the SC-MOF, apart from splicing, did not suffer from.

For the case of the ECF, NP immobilisation along only one channel of the SC allows a longer interaction distance to reach a predetermined extinction ratio (as attenuation is lower), hence easier handling, more rapid analyte response times, and lower sample volumes for optofluidic application. Real-time core/channel observation and collection of scattered light is additionally available due to the exposed nature of the core.

Both monolithic sensing systems enable reusability due to the immobilisation of the NPs – essential for targeted applications in molecular diagnostics. Due to the small cores and integrated arrangement of optical core proximity to microfluidic microstructured channels, these fibres present fully integrated optofluidic sensing systems, allowing real-time monitoring of analytes and requiring low sample volumes ( $\sim 3 \mu\text{l}$  over 1 cm sample length) – both highly relevant within noninvasive bioanalytics, molecular disease diagnostics and environmental science. This approach offers an efficient, easy-to-use, and multiplex-compatible sensing platform for rapid small-volume detection with capacity for integration into an optofluidic, bioanalytic, or microfluidic system.

Through this study both experimentally and by simulation, the initial thesis objectives were explored and compounded upon, realising:

- A thorough investigation of light-matter interaction of immobilised metallic NPs i.e. LSPRs with the propagating fundamental modes of MOFs.
- Sensing application with plasmonic-functionalised fibres, i.e., detecting RI induced LSPR shifts.
- Detection of binding events of ssDNA-sequences on NPs on planar substrate and their corresponding hybridisation events – towards the eventual application as a real world pathogen detection device.

Further concomitant investigations included:

- How MOF properties could enhance functionality and performance of photonic-plasmonic biosensors.
- Which NPs parameters are optimal for obtaining high RI sensitivity for biosensing using MOFs.
- Whether flexible fibre-biosensors could be designed with the potential for application in a clinical environment.

### **System improvement**

The most significant advantage offered by the ECF is its potential for distributed sensing. The openly accessible channel, allows access to a completely tailorable interaction length between guided mode and NP ensemble. Tailoring this interaction length, i.e., depositing NPs only within predefined positions on the ECF, offers a distinct advantage over other fibre-based concepts, where typically NPs could only be deposited along the entire

sample length, as is the case with the SC-MOF. This further presents the possibility of plasmonic multiplexing by immobilising NPs with different properties (geometry, size, composition etc.) at various locations along the same ECF. The various plasmonic ECF regions would then be functionalised to sense for different pathogen species within one sample – in one device simultaneously.

In order to obtain similar tailored deposition regions within the more integrated SC-MOF two additional deposition mechanisms exist that, following further development, may be promising for future application. These involve using UV-sensitive organosilanes and a microwave induced particle deposition.

### **UV-sensitive organosilanes**

The idea behind a UV activated organosilane approach is to assemble the Au NPs into micropatterns or segments by means of UV light-assisted “uncaging” of surface amines [240–243]. In a simple scheme, APTES could be used as an amine terminated silane for NP bonding, and NVOC (nitroveratryloxycarbonyl chloride) as an amino caging, photocleavable group. To cage the surface amine groups and block them from binding to gold, an activated APTES treated surface could be incubated in an NVOC chloride – chloroform solution. To uncage amino sections the sample would then be irradiated through a photomask with a Xe lamp for instance. The UV light essentially strips away the NVOC group and exposes the amino group again for NP binding. In this way sections of fibre could be masked to prevent deposition, and other deposition targeted regions exposed to the UV light.

Optimising a working protocol for this method would be time, cost, and chemistry intensive. However, the final concept of exposing or masking regions on the SC-MOF and applying UV light before NP incubation is very simple and highly attractive to achieve a patterned internal deposition – which is essential if one wants to apply a plasmonic SC-MOF for real world sensing.

### **Microwave induced particle deposition**

Alternatively, Microwave irradiation (MW) – owing to the speed and homogeneity of its locally produced heating – exists as a rapid synthesis approach for nanostructures with high shape and dimensional control [244–246]. Recently, a simple and fast one-step procedure to procure Ag NP films within the interior hole of glass fibre capillaries was demonstrated by one such microwave-assisted preparation method [247,248]. Microwave irradiation of a mixture of silver acetate and ethanol reducing agent enabled the simultaneous formation and deposition of homogeneous, high density, monolayer NP coatings. Only a small analyte volume and short (1.5–3 minutes) and simple (capillary action filling) incubation process was required – without any pre-surface modifications or added surfactants.

While Au NPs can be formed by MW assisted deposition [247], no evidence of reproducing the adhesive effect of Ag with Au particles has been published. Even for the

Ag monolayer, the SC-MOF would require a far lower density for LSPR sensing than presented in literature.

Ultimately, through manually controlled MW operation and drawing an SC-MOF sample through the MW area, segmented targeted deposition regions similar to the ECF are envisaged that are enclosed within the structurally more robust SC-MOF.

### **Sensitivity improvement**

The last point to mention is that the Au nanospheres used in this work provide a good starting transducer for developing a biosensor due to reduced polarisation requirements, shape stability without capping agents, and high binding affinity and quality. These nanoparticles however possess some of the lowest sensitivities [53]. Once the sensor systems demonstrate successful DNA binding detection they should be further optimised by increasing sensitivity through choice of NP.

### **Towards real world sensing**

The next step in this topic would be the LSPR mediated, microscopic detection of DNA binding events using the ECF system. As mentioned, preliminary studies were taken to investigate the feasibility of this. Single strand capture DNA was successfully attached to 80 nm Au NPs on planar substrate and the corresponding LSPR shift recorded (2.5 nm shift upon capture ssDNA binding). The introduction of non-complementary ssDNA yielded no LSPR shift (indicating no binding with capture). The subsequent introduction of complementary target ssDNA resulted in hybridisation and an enhanced LSPR shift (10 nm shift upon hybridisation with NP labelled target DNA). Target strands were demonstrated to be removable through denaturation, and the sensor reusable. It was also possible to run NP immobilisation on ECF in the envisaged chamber but with high optical attenuation due to the delicate nature of the ECF structure, its high sensitivity to attenuation, and the surplus of rapidly depositing NPs in the chamber.

While it would be certainly possible to monitor the NP scattering behaviour from the side looking directly onto the exposed core and detect DNA binding in this respect, the goal of this work was to use the guided mode to deliver this information. This would lead ultimately to a simpler application requiring less complex setups, and a larger sample of NPs (distributed multiplexed sensing).

A double-splice flow cell as proposed in Ch. 5.4 would be highly practical to achieve and implement DNA sensing. In this scheme the ECF sensing region would be protected from atmospheric contamination and fibre handling would be minimised. The flow cell would add mechanical support without contact pressure as imposed by the eLSPR microfluidic chip system – since the flow cell would adhere to the outer spliced fibres and not the ECF. Such a flow chamber configuration has been applied by collaborators [214] with larger core ECFs for application as a Sagnac-interferometer biosensor. Splicing small-core ECFs is however extremely difficult [232] and requires an intensive parameter and feasibility study. The small suspended-core and thin supporting struts of these structures

make for highly challenging alignment and are easily distorted during splicing. The resulting splices suffer from high attenuation due to non-perfect alignment, structural distortion and breakage, and generated debris. Very recently a small-core ECF – possessing shorter, thicker strands than in this study – was spliced at one end to an ultrahigh NA fibre [249] and used for NP detection. Details on splice quality were not provided but this is highly promising for ECF integration. Potentially tapering a large-core ECF could allow more straightforward splicing at the large-core facets and sufficient modal attenuation in the small-core tapered-midsection. An ECF taper would prove more robust than a standard taper due to the extra protection from the cladding region, and applying a flow cell around this section would offer further protection while maintaining optofluidic containment. This is a hypothetical suggestion however.

The ideal configuration for a plasmonic fibre biosensor would involve site-specific immobilisation of a highly sensitive NP species allowing DNA access for attachment and hybridisation, a chamber area within the fibre with means for rapid small volume exchange, and a robust, well-fabricated SCF.

Some future directions of SC fibres as plasmonic biosensors may include application as whispering gallery mode, WGM, sensors [250], or incorporating antigen fibre Bragg gratings through site specific depositions as diffractometric biosensors – e.g. focal molography [251,252]. The SC-MOFs in this study are furthermore multimodal and exploiting their higher order modes may prove desirable for some applications and could be considered in future work.

## BIBLIOGRAPHY

---

- [1] O. Lazcka, F. J. Del Campo, and F. X. Munoz. Pathogen detection: A perspective of traditional methods and biosensors. *Biosensors and bioelectronics*, 22(7):1205–1217, 2007. (Cited on page 1.)
- [2] P. D’Orazio. Biosensors in clinical chemistry–2011 update. *Clinica Chimica Acta*, 412(19-20):1749–1761, 2011. (Cited on page 1.)
- [3] S. M. Yoo and S. Y. Lee. Optical biosensors for the detection of pathogenic microorganisms. *Trends in biotechnology*, 34(1):7–25, 2016. (Cited on page 1.)
- [4] K. S. Gracias and J. L. McKillip. A review of conventional detection and enumeration methods for pathogenic bacteria in food. *Canadian journal of microbiology*, 50(11):883–890, 2004. (Cited on page 1.)
- [5] B. W. Brooks, J. Devenish, C. L. Lutze-Wallace, D. Milnes, R. H. Robertson, and G. Berlie-Surujballi. Evaluation of a monoclonal antibody-based enzyme-linked immunosorbent assay for detection of campylobacter fetus in bovine preputial washing and vaginal mucus samples. *Veterinary microbiology*, 103(1-2):77–84, 2004. (Cited on page 1.)
- [6] A. Sassolas, B. D. Leca-Bouvier, and L. J. Blum. DNA biosensors and microarrays. *Chemical reviews*, 108(1):109–139, 2008. (Cited on pages 1, 33, and 34.)
- [7] W. Joseph. From DNA biosensors to gene chips. *Nucleic Acids Res*, 28(301):1–3016, 2000. (Cited on page 1.)
- [8] S. Hahn, S. Mergenthaler, B. Zimmermann, and W. Holzgreve. Nucleic acid based biosensors: the desires of the user. *Bioelectrochemistry*, 67(2):151–154, 2005. (Cited on page 1.)
- [9] F. Bertucci, R. Houlgatte, C. Nguyen, P. Viens, B. R. Jordan, and D. Birnbaum. Gene expression profiling of cancer by use of DNA arrays: how far from the clinic? *The lancet oncology*, 2(11):674–682, 2001. (Cited on page 1.)
- [10] Y. Wang and J. K. Salazar. Culture-independent rapid detection methods for bacterial pathogens and toxins in food matrices. *Comprehensive Reviews in Food Science and Food Safety*, 15(1):183–205, 2016. (Cited on page 1.)
- [11] R. S. Marks, C. R. Lowe, D. C. Cullen, H. H. Weetall, and I. Karube. Handbook of biosensors and biochips. (Cited on pages 1, 2, and 3.)
- [12] J. Lamartine. The benefits of DNA microarrays in fundamental and applied biomedicine. *Materials Science and Engineering: C*, 26(2-3):354–359, 2006. (Cited on page 1.)

- [13] P. A. Bryant, D. Venter, R. Robins-Browne, and N. Curtis. Chips with everything: DNA microarrays in infectious diseases. *The Lancet infectious diseases*, 4(2):100–111, 2004. (Cited on page 1.)
- [14] M. D. Winfield and E. A. Groisman. Role of nonhost environments in the lifestyles of salmonella and escherichia coli. *Appl. Environ. Microbiol.*, 69(7):3687–3694, 2003. (Cited on page 1.)
- [15] I. Rahman, M. Shahamat, M. A. Chowdhury, and R. R. Colwell. Potential virulence of viable but nonculturable shigella dysenteriae type 1. *Appl. Environ. Microbiol.*, 62(1):115–120, 1996. (Cited on page 1.)
- [16] I. Effendi and B. Austin. Dormant/unculturable cells of the fish pathogen aeromonas salmonicida. *Microbial ecology*, 30(2):183–192, 1995. (Cited on page 1.)
- [17] C. Rovey, G. Greub, H. Lepidi, J. P. Casalta, G. Habib, F. Collart, and D. Raoult. PCR detection of bacteria on cardiac valves of patients with treated bacterial endocarditis. *Journal of clinical microbiology*, 43(1):163–167, 2005. (Cited on page 1.)
- [18] J. Rosamond and A. Allsop. Harnessing the power of the genome in the search for new antibiotics. *Science*, 287(5460):1973–1976, 2000. (Cited on page 1.)
- [19] M. Fox. Optical properties of solids, 2002. (Cited on page 1.)
- [20] S. M. Borisov and O. S. Wolfbeis. Optical biosensors. *Chemical reviews*, 108(2):423–61, 2008. (Cited on page 1.)
- [21] P. Damborský, J. Švitel, and J. Katrlík. Optical biosensors. *Essays in biochemistry*, 60(1):91–100, 2016. (Cited on page 1.)
- [22] X. Fan, I. M. White, S. I. Shopova, H. Zhu, J. D. Suter, and Y. Sun. Sensitive optical biosensors for unlabeled targets: A review. *analytica chimica acta*, 620(1-2):8–26, 2008. (Cited on page 1.)
- [23] J. Cao, T. Sun, and K. T. V. Grattan. Gold nanorod-based localized surface plasmon resonance biosensors: A review. *Sensors and actuators B: Chemical*, 195:332–351, 2014. (Cited on pages 1 and 2.)
- [24] Y. Li, W. A. Dick, and O. H. Tuovinen. Fluorescence microscopy for visualization of soil microorganisms—a review. *Biology and fertility of soils*, 39(5):301–311, 2004. (Cited on page 2.)
- [25] S. Ko and S. A. Grant. Development of a novel FRET method for detection of listeria or salmonella. *Sensors and Actuators B: Chemical*, 96(1-2):372–378, 2003. (Cited on page 2.)
- [26] N. A. Rakow and K. S. Suslick. A colorimetric sensor array for odour visualization. *Nature*, 406(6797):710, 2000. (Cited on page 2.)



- [27] H. N. Kim, W. X. Ren, J. S. Kim, and J. Yoon. Fluorescent and colorimetric sensors for detection of lead, cadmium, and mercury ions. *Chemical Society Reviews*, 41(8):3210–3244, 2012. (Cited on page 2.)
- [28] H. Peng, L. Zhang, T. H. M. Kjällman, C. Soeller, and J. Travas-Sejdic. DNA hybridization detection with blue luminescent quantum dots and dye-labeled single-stranded DNA. *Journal of the American Chemical Society*, 129(11):3048–3049, 2007. (Cited on page 2.)
- [29] D. R. Walt. Optical methods for single molecule detection and analysis. *Analytical chemistry*, 85(3):1258–1263, 2013. (Cited on page 2.)
- [30] B. Huang, H. Wu, D. Bhaya, A. Grossman, S. Granier, B. K. Kobilka, and R. N. Zare. Counting low-copy number proteins in a single cell. *Science*, 315(5808):81–84, 2007. (Cited on page 2.)
- [31] J. Elf, G. W. Li, and X. S. Xie. Probing transcription factor dynamics at the single-molecule level in a living cell. *Science*, 316(5828):1191–1194, 2007. (Cited on page 2.)
- [32] E. C. Jensen. Use of fluorescent probes: their effect on cell biology and limitations. *The Anatomical Record: Advances in Integrative Anatomy and Evolutionary Biology*, 295(12):2031–2036, 2012. (Cited on page 2.)
- [33] N. C. Shaner, P. A. Steinbach, and R. Y. Tsien. A guide to choosing fluorescent proteins. *Nature methods*, 2(12):905, 2005. (Cited on page 2.)
- [34] M. Nissen, B. Doherty, J. Hamperl, J. Kobelke, K. Weber, T. Henkel, and M. A. Schmidt. UV absorption spectroscopy in water-filled antiresonant hollow core fibers for pharmaceutical detection. *Sensors*, 18(2):478, 2018. (Cited on pages 2 and 4.)
- [35] L. Kröckel, T. Frosch, and M. A. Schmidt. Multiscale spectroscopy using a monolithic liquid core waveguide with laterally attached fiber ports. *Analytica chimica acta*, 875:1–6, 2015. (Cited on page 2.)
- [36] E. Klantsataya, P. Jia, H. Ebendorff-Heidepriem, T. Monro, and A. François. Plasmonic fiber optic refractometric sensors: From conventional architectures to recent design trends. *Sensors*, 17(1):12, 2017. (Cited on pages 2 and 8.)
- [37] M. Gupta, H. Jiao, and A. O’Keefe. Cavity-enhanced spectroscopy in optical fibers. *Optics letters*, 27(21):1878–1880, 2002. (Cited on page 2.)
- [38] A. M. Armani, R. P. Kulkarni, S. E. Fraser, R. C. Flagan, and K. J. Vahala. Label-free, single-molecule detection with optical microcavities. *science*, 317(5839):783–787, 2007. (Cited on page 2.)

- [39] M. Chamanzar, Z. Xia, S. Yegnanarayanan, and A. Adibi. Hybrid integrated plasmonic-photonic waveguides for on-chip localized surface plasmon resonance (LSPR) sensing and spectroscopy. *Optics express*, 21(26):32086–32098, 2013. (Cited on page 2.)
- [40] C. Monat, P. Domachuk, and B. J. Eggleton. Integrated optofluidics: A new river of light. *Nature photonics*, 1(2):106, 2007. (Cited on page 2.)
- [41] P. Kozma, F. Kehl, E. Ehrentreich-Förster, C. Stamm, and F. F. Bier. Integrated planar optical waveguide interferometer biosensors: A comparative review. *Biosensors and Bioelectronics*, 58:287–307, 2014. (Cited on page 2.)
- [42] T. Schneider, N. Jahr, J. Jatschka, A. Csaki, O. Stranik, and W. Fritzsche. Localized surface plasmon resonance (LSPR) study of DNA hybridization at single nanoparticle transducers. *Journal of nanoparticle research*, 15(4):1531, 2013. (Cited on pages 2, 3, 7, and 87.)
- [43] A. Dmitriev. *Nanoplasmonic sensors*. Springer Science & Business Media, 2012. (Cited on page 2.)
- [44] A. G. Brolo. Plasmonics for future biosensors. *Nature Photonics*, 6(11):709, 2012. (Cited on page 2.)
- [45] S. A. Maier and H. A. Atwater. Plasmonics: Localization and guiding of electromagnetic energy in metal/dielectric structures. *Journal of applied physics*, 98(1):10, 2005. (Cited on pages 2 and 17.)
- [46] S. A. Maier. *Plasmonics: fundamentals and applications*. Springer Science & Business Media, 2007. (Cited on pages 2, 13, 15, 16, 17, 18, and 25.)
- [47] K. A. Willets and R. P. Van Duyne. Localized surface plasmon resonance spectroscopy and sensing. *Annu. Rev. Phys. Chem.*, 58:267–297, 2007. (Cited on pages 2, 13, and 22.)
- [48] J. Zhao, X. Zhang, C. R. Yonzon, A. J. Haes, and R. P. Van Duyne. Localized surface plasmon resonance biosensors. 2006. (Cited on page 2.)
- [49] J. J. Mock, D. R. Smith, and S. Schultz. Local refractive index dependence of plasmon resonance spectra from individual nanoparticles. *Nano letters*, 3(4):485–491, 2003. (Cited on page 2.)
- [50] T. R. Jensen, M. D. Malinsky, C. L. Haynes, and R. P. Van Duyne. Nanosphere lithography: tunable localized surface plasmon resonance spectra of silver nanoparticles. *The Journal of Physical Chemistry B*, 104(45):10549–10556, 2000. (Cited on page 2.)

- [51] A. Steinbrück, O. Stranik, A. Csaki, and W. Fritzsche. Sensoric potential of gold–silver core–shell nanoparticles. *Analytical and bioanalytical chemistry*, 401(4):1241, 2011. (Cited on page 2.)
- [52] P. R. West, S. Ishii, G. V. Naik, N. K. Emani, V. M. Shalaev, and A. Boltasseva. Searching for better plasmonic materials. *Laser & Photonics Reviews*, 4(6):795–808, 2010. (Cited on pages 2 and 18.)
- [53] A. Csaki, M. Thiele, J. Jatschka, A. Dathe, D. Zopf, O. Stranik, and W. Fritzsche. Plasmonic nanoparticle synthesis and bioconjugation for bioanalytical sensing. *Engineering in Life Sciences*, 15(3):266–275, 2015. (Cited on pages 2, 16, 26, 34, 44, 83, and 99.)
- [54] J. Yguerabide and E. E. Yguerabide. Light-scattering submicroscopic particles as highly fluorescent analogs and their use as tracer labels in clinical and biological applications: II. experimental characterization. *Analytical biochemistry*, 262(2):157–176, 1998. (Cited on page 2.)
- [55] J. N. Anker, W. P. Hall, O. Lyandres, N. C. Shah, J. Zhao, and R. P. Van Duyne. Biosensing with plasmonic nanosensors. In *Nanoscience and Technology: A Collection of Reviews from Nature Journals*, pages 308–319. World Scientific, 2010. (Cited on pages 2, 6, and 15.)
- [56] A. Steinbrück, A. Csaki, and W. Fritzsche. Metal nanoparticles for molecular plasmonics. In *Reviews in Plasmonics 2010*, pages 1–37. Springer, 2012. (Cited on pages 2 and 95.)
- [57] G. Raschke, S. Kowarik, T. Franzl, C. Sönnichsen, T. A. Klar, J. Feldmann, A. Nichtl, and K. Kürzinger. Biomolecular recognition based on single gold nanoparticle light scattering. *Nano letters*, 3(7):935–938, 2003. (Cited on page 2.)
- [58] A. J. Haes and R. P. Van Duyne. A nanoscale optical biosensor: sensitivity and selectivity of an approach based on the localized surface plasmon resonance spectroscopy of triangular silver nanoparticles. *Journal of the American Chemical Society*, 124(35):10596–10604, 2002. (Cited on pages 2, 3, and 22.)
- [59] A. J. Haes and R. P. Van Duyne. Preliminary studies and potential applications of localized surface plasmon resonance spectroscopy in medical diagnostics. *Expert Review of Molecular Diagnostics*, 4(4):527–537, 2004. (Cited on page 2.)
- [60] J. A. Schuller, E. S. Barnard, W. Cai, Y. C. Jun, J. S. White, and M. L. Brongersma. Plasmonics for extreme light concentration and manipulation. *Nature materials*, 9(3):193, 2010. (Cited on page 2.)

- [61] S. Faez, Y. Lahini, S. Weidlich, R. F. Garmann, K. Wondraczek, M. Zeisberger, M. A. Schmidt, M. Orrit, and V. N. Manoharan. Fast, label-free tracking of single viruses and weakly scattering nanoparticles in a nanofluidic optical fiber. *ACS nano*, 9(12):12349–12357, 2015. (Cited on pages 3 and 4.)
- [62] J. M. Bingham, K. A. Willets, N. C. Shah, D. Q. Andrews, and R. P. Van Duyne. Localized surface plasmon resonance imaging: simultaneous single nanoparticle spectroscopy and diffusional dynamics. *The Journal of Physical Chemistry C*, 113(39):16839–16842, 2009. (Cited on page 3.)
- [63] S. M. Marinakos, S. Chen, and A. Chilkoti. Plasmonic detection of a model analyte in serum by a gold nanorod sensor. *Analytical chemistry*, 79(14):5278–5283, 2007. (Cited on page 3.)
- [64] N. Nath and A. Chilkoti. A colorimetric gold nanoparticle sensor to interrogate biomolecular interactions in real time on a surface. *Analytical chemistry*, 74(3):504–509, 2002. (Cited on page 3.)
- [65] K. Jia, J. L. Bijeon, P. M. Adam, and R. E. Ionescu. A facile and cost-effective template approach to design gold nano-structured substrates for high throughput plasmonic sensitive detection of biomolecules. *Analyst*, 138(4):1015–1019, 2013. (Cited on page 3.)
- [66] O. Kedem, A. Vaskevich, and I. Rubinstein. Critical issues in localized plasmon sensing. *The Journal of Physical Chemistry C*, 118(16):8227–8244, 2014. (Cited on page 3.)
- [67] O. Kedem, A. B. Tesler, A. Vaskevich, and I. Rubinstein. Sensitivity and optimization of localized surface plasmon resonance transducers. *ACS nano*, 5(2):748–760, 2011. (Cited on page 3.)
- [68] G. Kalyuzhny, A. Vaskevich, M. A. Schneeweiss, and I. Rubinstein. Transmission surface-plasmon resonance (T-SPR) measurements for monitoring adsorption on ultrathin gold island films. *Chemistry—A European Journal*, 8(17):3849–3857, 2002. (Cited on page 3.)
- [69] S. Chen, M. Svedendahl, M. Käll, L. Gunnarsson, and A. Dmitriev. Ultrahigh sensitivity made simple: nanoplasmonic label-free biosensing with an extremely low limit-of-detection for bacterial and cancer diagnostics. *Nanotechnology*, 20(43):434015, 2009. (Cited on page 3.)
- [70] A. B. Dahlin, S. Chen, M. P. Jonsson, L. Gunnarsson, M. Käll, and F. Höök. High-resolution microspectroscopy of plasmonic nanostructures for miniaturized biosensing. *Analytical chemistry*, 81(16):6572–6580, 2009. (Cited on page 3.)

- [71] J. A. Ruemmele, W. P. Hall, L. K. Ruvuna, and R. P. Van Duyne. A localized surface plasmon resonance imaging instrument for multiplexed biosensing. *Analytical chemistry*, 85(9):4560–4566, 2013. (Cited on page 3.)
- [72] N. Jahr, M. Anwar, O. Stranik, N. Hädrich, N. Vogler, A. Csaki, J. Popp, and W. Fritzsche. Spectroscopy on single metallic nanoparticles using subwavelength apertures. *The Journal of Physical Chemistry C*, 117(15):7751–7756, 2013. (Cited on page 3.)
- [73] H. Wang, G. Rong, B. Yan, L. Yang, and B. M. Reinhard. Optical sizing of immunolabel clusters through multispectral plasmon coupling microscopy. *Nano letters*, 11(2):498–504, 2011. (Cited on page 3.)
- [74] R. T. Hill. Plasmonic biosensors. *Wiley Interdisciplinary Reviews: Nanomedicine and Nanobiotechnology*, 7(2):152–168, 2015. (Cited on page 3.)
- [75] I. Ament, J. Prasad, A. Henkel, S. Schmachtel, and C. Sonnichsen. Single unlabeled protein detection on individual plasmonic nanoparticles. *Nano letters*, 12(2):1092–1095, 2012. (Cited on page 3.)
- [76] S. Chen, M. Svedendahl, R. P. Van Duyne, and M. Käll. Plasmon-enhanced colorimetric ELISA with single molecule sensitivity. *Nano letters*, 11(4):1826–1830, 2011. (Cited on page 3.)
- [77] G. J. Nusz, S. M. Marinakos, S. Rangarajan, and A. Chilkoti. Dual-order snapshot spectral imaging of plasmonic nanoparticles. *Applied optics*, 50(21):4198–4206, 2011. (Cited on page 3.)
- [78] L. Guo, A. R. Ferhan, K. Lee, and D. H. Kim. Nanoarray-based biomolecular detection using individual Au nanoparticles with minimized localized surface plasmon resonance variations. *Analytical chemistry*, 83(7):2605–2612, 2011. (Cited on page 3.)
- [79] D. Zopf, A. Pittner, A. Dathe, N. Grosse, A. Csáki, K. Arstila, J. J. Toppari, W. Schott, D. Dontsov, G. Uhlrich, et al. Plasmonic nanosensor array for multiplexed DNA-based pathogen detection. *ACS sensors*, 4(2):335–343, 2019. (Cited on pages 3, 35, 83, 84, 85, and 91.)
- [80] L. Soares, A. Csáki, J. Jatschka, W. Fritzsche, O. Flores, R. Franco, and E. Pereira. Localized surface plasmon resonance (LSPR) biosensing using gold nanotriangles: detection of DNA hybridization events at room temperature. *Analyst*, 139(19):4964–4973, 2014. (Cited on pages 3 and 7.)
- [81] G. K. Joshi, S. Deitz-McElyea, M. Johnson, S. Mali, M. Korc, and R. Sardar. Highly specific plasmonic biosensors for ultrasensitive microRNA detection in plasma from pancreatic cancer patients. *Nano letters*, 14(12):6955–6963, 2014. (Cited on page 3.)

- [82] K. Nagayama, M. Kakui, M. Matsui, I. Saitoh, and Y. Chigusa. Ultra-low-loss (0.1484 dB/km) pure silica core fibre and extension of transmission distance. *Electronics Letters*, 38(20):1168–1169, 2002. (Cited on page 3.)
- [83] P. J. Roberts, F. Couny, H. Sabert, B. J. Mangan, D. P. Williams, L. Farr, M. W. Mason, A. Tomlinson, T. A. Birks, J. C. Knight, et al. Ultimate low loss of hollow-core photonic crystal fibres. *Optics express*, 13(1):236–244, 2005. (Cited on page 3.)
- [84] B. Lee, S. Roh, and J. Park. Current status of micro-and nano-structured optical fiber sensors. *Optical Fiber Technology*, 15(3):209–221, 2009. (Cited on page 4.)
- [85] T. Wieduwilt, A. Tuniz, S. Linzen, S. Goerke, J. Dellith, U. Hübner, and M. A. Schmidt. Ultrathin niobium nanofilms on fiber optical tapers—a new route towards low-loss hybrid plasmonic modes. *Scientific reports*, 5:17060, 2015. (Cited on pages 4 and 5.)
- [86] P. Polynkin, A. Polynkin, N. Peyghambarian, and M. Mansuripur. Evanescent field-based optical fiber sensing device for measuring the refractive index of liquids in microfluidic channels. *Optics letters*, 30(11):1273–1275, 2005. (Cited on page 4.)
- [87] A. R. Camara, P. M. P. Gouvêa, A. C. M. S. Dias, A. M. B. Braga, R. F. Dutra, R. E. de Araujo, and I. C. S. Carvalho. Dengue immunoassay with an LSPR fiber optic sensor. *Optics express*, 21(22):27023–27031, 2013. (Cited on page 4.)
- [88] M. A. Schmidt, A. Argyros, and F. Sorin. Hybrid optical fibers—an innovative platform for in-fiber photonic devices. *Advanced Optical Materials*, 4(1):13–36, 2016. (Cited on page 4.)
- [89] J. S. Y. Chen, Tijmen G Euser, Nicola J Farrer, P. J. Sadler, M. Scharrer, and P. St. J. Russell. Photochemistry in photonic crystal fiber nanoreactors. *Chemistry—A European Journal*, 16(19):5607–5612, 2010. (Cited on pages 4 and 5.)
- [90] C. M. B. Cordeiro, M. A. R. Franco, G. Chesini, E. C. S. Barretto, R. Lwin, C. H. B. Cruz, and M. C. J. Large. Microstructured-core optical fibre for evanescent sensing applications. *Optics Express*, 14(26):13056–13066, 2006. (Cited on page 4.)
- [91] V. S. Afshar, S. C. Warren-Smith, and T. M. Monro. Enhancement of fluorescence-based sensing using microstructured optical fibres. *Optics Express*, 15(26):17891–17901, 2007. (Cited on page 4.)
- [92] F. Couny, F. Benabid, and P. S. Light. Large-pitch kagome-structured hollow-core photonic crystal fiber. *Optics letters*, 31(24):3574–3576, 2006. (Cited on page 4.)
- [93] J. Cao, M. H. Tu, T. Sun, and K. T. V. Grattan. Wavelength-based localized surface plasmon resonance optical fiber biosensor. *Sensors and Actuators B: Chemical*, 181:611–619, 2013. (Cited on pages 4 and 5.)

- [94] A. M. Aravanis, L. P. Wang, F. Zhang, L. A. Meltzer, M. Z. Mogri, M. B. Schneider, and K. Deisseroth. An optical neural interface: in vivo control of rodent motor cortex with integrated fiberoptic and optogenetic technology. *Journal of neural engineering*, 4(3):S143, 2007. (Cited on page 4.)
- [95] A. Urrutia, J. Goicoechea, and F. J. Arregui. Optical fiber sensors based on nanoparticle-embedded coatings. *Journal of Sensors*, 2015, 2015. (Cited on page 5.)
- [96] J. Luo, J. Yao, Y. Lu, W. Ma, and X. Zhuang. A silver nanoparticle-modified evanescent field optical fiber sensor for methylene blue detection. *Sensors*, 13(3):3986–3997, 2013. (Cited on page 5.)
- [97] T. Wieduwilt, M. Zeisberger, M. Thiele, B. Doherty, M. Chemnitz, A. Csaki, W. Fritzsche, and M. A. Schmidt. Gold-reinforced silver nanoprisms on optical fiber tapers—a new base for high precision sensing. *APL Photonics*, 1(6):066102, 2016. (Cited on pages 5, 7, 37, 42, 51, 57, 58, 83, and 96.)
- [98] J. Cao, E. K. Galbraith, T. Sun, and K. T. V. Grattan. Cross-comparison of surface plasmon resonance-based optical fiber sensors with different coating structures. *IEEE Sensors Journal*, 12(7):2355–2361, 2012. (Cited on pages 5 and 7.)
- [99] H. Y. Lin, C. H. Huang, G. L. Cheng, N. K. Chen, and H. C. Chui. Tapered optical fiber sensor based on localized surface plasmon resonance. *Optics Express*, 20(19):21693–21701, 2012. (Cited on pages 5 and 7.)
- [100] T. Wieduwilt, K. Kirsch, J. Dellith, R. Willsch, and H. Bartelt. Optical fiber micro-taper with circular symmetric gold coating for sensor applications based on surface plasmon resonance. *Plasmonics*, 8(2):545–554, 2013. (Cited on page 5.)
- [101] S. Kaye, Z. Zeng, M. Sanders, K. Chittur, P. M. Koelle, R. Lindquist, U. Manne, Y. Lin, and J. Wei. Label-free detection of DNA hybridization with a compact LSPR-based fiber-optic sensor. *Analyst*, 142(11):1974–1981, 2017. (Cited on page 5.)
- [102] B. Sciacca and T. M. Monro. Dip biosensor based on localized surface plasmon resonance at the tip of an optical fiber. *Langmuir*, 30(3):946–954, 2014. (Cited on pages 5 and 8.)
- [103] T. M. Monro, W. Belardi, K. Furusawa, J. C. Baggett, N. G. R. Broderick, and D. J. Richardson. Sensing with microstructured optical fibres. *Measurement Science and Technology*, 12(7):854, 2001. (Cited on pages 5, 7, and 96.)
- [104] J. M. Fini. Microstructure fibres for optical sensing in gases and liquids. *Measurement Science and Technology*, 15(6):1120, 2004. (Cited on pages 5 and 7.)
- [105] B. Doherty, A. Csáki, M. Thiele, M. Zeisberger, A. Schwuchow, J. Kobelke, W. Fritzsche, and M. A. Schmidt. Nanoparticle functionalised small-core suspended-core

fibre—a novel platform for efficient sensing. *Biomedical optics express*, 8(2):790–799, 2017. (Cited on pages 5, 11, 16, 37, 42, and 65.)

- [106] B. Doherty, M. Thiele, S. Warren-Smith, E. Schartner, H. Ebendorff-Heidepriem, W. Fritzsche, and M. A. Schmidt. Plasmonic nanoparticle-functionalized exposed-core fiber—an optofluidic refractive index sensing platform. *Optics letters*, 42(21):4395–4398, 2017. (Cited on pages 5, 11, 16, 37, 51, 65, and 96.)
- [107] S. C. Warren-Smith, J. Wie, M. Chemnitz, R. KostECKI, H. Ebendorff-Heidepriem, T. M. Monro, and M. A. Schmidt. Third harmonic generation in exposed-core microstructured optical fibers. *Optics express*, 24(16):17860–17867, 2016. (Cited on pages 5, 51, and 96.)
- [108] A. J. Haes, S. Zou, G. C. Schatz, and R. P. Van Duyne. A nanoscale optical biosensor: the long range distance dependence of the localized surface plasmon resonance of noble metal nanoparticles. *The Journal of Physical Chemistry B*, 108(1):109–116, 2004. (Cited on pages 6 and 26.)
- [109] J. J. Storhoff, R. Elghanian, R. C. Mucic, C. A. Mirkin, and R. L. Letsinger. One-pot colorimetric differentiation of polynucleotides with single base imperfections using gold nanoparticle probes. *Journal of the American Chemical Society*, 120(9):1959–1964, 1998. (Cited on page 6.)
- [110] C. A. Mirkin, R. L. Letsinger, R. C. Mucic, and J. J. Storhoff. A DNA-based method for rationally assembling nanoparticles into macroscopic materials. *Nature*, 382(6592):607, 1996. (Cited on page 6.)
- [111] L. Olofsson, T. Rindzevicius, I. Pfeiffer, M. Käll, and F. Höök. Surface-based gold-nanoparticle sensor for specific and quantitative DNA hybridization detection. *Langmuir*, 19(24):10414–10419, 2003. (Cited on page 6.)
- [112] J. J. Storhoff, A. D. Lucas, V. Garimella, Y. P. Bao, and U. R. Müller. Homogeneous detection of unamplified genomic DNA sequences based on colorimetric scatter of gold nanoparticle probes. *Nature biotechnology*, 22(7):883, 2004. (Cited on page 6.)
- [113] P. Kvasnička and J. Homola. Optical sensors based on spectroscopy of localized surface plasmons on metallic nanoparticles: Sensitivity considerations. *Biointerphases*, 3(3):FD4–FD11, 2008. (Cited on pages 7, 13, 23, and 25.)
- [114] T. M. Monro, S. Warren-Smith, E. P. Schartner, A. François, S. Heng, H. Ebendorff-Heidepriem, and S. Afshar. Sensing with suspended-core optical fibers. *Optical Fiber Technology*, 16(6):343–356, 2010. (Cited on pages 7 and 38.)
- [115] T. G. Euser, J. S. Y. Chen, M. Scharrer, P. St. J. Russell, N. J. Farrer, and P. J. Sadler. Quantitative broadband chemical sensing in air-suspended solid-core fibers. *Journal of Applied Physics*, 103(10):103108, 2008. (Cited on page 7.)



- [116] A. M. Cubillas, S. Unterkofler, T. G. Euser, B. J. M. Etzold, A. C. Jones, P. J. Sadler, P. Wasserscheid, and P. St. J. Russell. Photonic crystal fibres for chemical sensing and photochemistry. *Chemical Society Reviews*, 42(22):8629–8648, 2013. (Cited on page 7.)
- [117] G. O. S. Williams, J. S. Y. Chen, T. G. Euser, P. St. J. Russell, and A. C. Jones. Photonic crystal fibre as an optofluidic reactor for the measurement of photochemical kinetics with sub-picomole sensitivity. *Lab on a Chip*, 12(18):3356–3361, 2012. (Cited on page 7.)
- [118] T. Tenderenda, M. Murawski, M. Szymanski, L. Szostkiewicz, M. Becker, M. Rothhardt, H. Bartelt, P. Mergo, K. Skorupski, P. Marc, et al. Fiber Bragg grating inscription in few-mode highly birefringent microstructured fiber. *Optics letters*, 38(13):2224–2226, 2013. (Cited on page 7.)
- [119] M. Becker, J. Bergmann, S. Brückner, M. Franke, E. Lindner, M. W. Rothhardt, and H. Bartelt. Fiber bragg grating inscription combining DUV sub-picosecond laser pulses and two-beam interferometry. *Optics express*, 16(23):19169–19178, 2008. (Cited on page 7.)
- [120] T. Wieduwilt, J. Dellith, F. Talkenberg, H. Bartelt, and M. A. Schmidt. Reflectivity enhanced refractive index sensor based on a fiber-integrated fabry-perot microresonator. *Optics express*, 22(21):25333–25346, 2014. (Cited on page 7.)
- [121] A. Hassani and M. Skorobogatiy. Design of the microstructured optical fiber-based surface plasmon resonance sensors with enhanced microfluidics. *Optics Express*, 14(24):11616–11621, 2006. (Cited on page 8.)
- [122] E. Klantsataya, A. François, H. Ebendorff-Heidepriem, P. Hoffmann, and T. Monro. Surface plasmon scattering in exposed core optical fiber for enhanced resolution refractive index sensing. *Sensors*, 15(10):25090–25102, 2015. (Cited on pages 8 and 96.)
- [123] X. C. Yang, Y. Lu, B. L. Liu, and J. Q. Yao. Temperature sensor based on photonic crystal fiber filled with liquid and silver nanowires. *IEEE Photonics Journal*, 8(3):1–9, 2016. (Cited on page 8.)
- [124] M. Hautakorpi, M. Mattinen, and H. Ludvigsen. Surface-plasmon-resonance sensor based on three-hole microstructured optical fiber. *Optics express*, 16(12):8427–8432, 2008. (Cited on page 8.)
- [125] N. Luan, R. Wang, W. Lv, and J. Yao. Surface plasmon resonance sensor based on d-shaped microstructured optical fiber with hollow core. *Optics express*, 23(7):8576–8582, 2015. (Cited on page 8.)

- [126] A. Csaki, F. Jahn, I. Latka, T. Henkel, D. Malsch, T. Schneider, K. Schröder, K. Schuster, A. Schwuchow, R. Spittel, et al. Nanoparticle layer deposition for plasmonic tuning of microstructured optical fibers. *Small*, 6(22):2584–2589, 2010. (Cited on pages 8, 55, and 61.)
- [127] K. Schroder, A. Csaki, A. Schwuchow, F. Jahn, K. Strelau, I. Latka, T. Henkel, D. Malsch, K. Schuster, K. Weber, et al. Functionalization of microstructured optical fibers by internal nanoparticle mono-layers for plasmonic biosensor applications. *IEEE Sensors Journal*, 12(1):218–224, 2011. (Cited on pages 8 and 52.)
- [128] A. Schwuchow, M. Zobel, A. Csaki, K. Schröder, J. Kobelke, W. Fritzsche, and K. Schuster. Monolayers of different metal nanoparticles in microstructured optical fibers with multiplex plasmonic properties. *Optical Materials Express*, 2(8):1050–1055, 2012. (Cited on page 8.)
- [129] J. Kosman, J. Jatschka, A. Csaki, W. Fritzsche, B. Juskowiak, and O. Stranik. A new strategy for silver deposition on Au nanoparticles with the use of peroxidase-mimicking DNAzyme monitored via a localized surface plasmon resonance technique. *Sensors*, 17(4):849, 2017. (Cited on page 9.)
- [130] Y. Hong, Y. M. Huh, D. S. Yoon, and J. Yang. Nanobiosensors based on localized surface plasmon resonance for biomarker detection. *Journal of Nanomaterials*, 2012:111, 2012. (Cited on page 13.)
- [131] X. Lu, M. Rycenga, S. E. Skrabalak, B. Wiley, and Y. Xia. Chemical synthesis of novel plasmonic nanoparticles. *Annual review of physical chemistry*, 60:167–192, 2009. (Cited on pages 13, 20, and 25.)
- [132] F. P. Zamborini, L. Bao, and R. Dasari. Nanoparticles in measurement science. *Analytical chemistry*, 84(2):541–576, 2011. (Cited on pages 14 and 87.)
- [133] U. Kreibig and M. Vollmer. *Optical properties of metal clusters*, volume 25. Springer Science & Business Media, 2013. (Cited on pages 15 and 26.)
- [134] K. L. Kelly, E. Coronado, L. L. Zhao, and G. C. Schatz. The optical properties of metal nanoparticles: the influence of size, shape, and dielectric environment, 2003. (Cited on pages 15, 16, 18, and 20.)
- [135] G. Mie. Contributions to the optics of turbid media, particularly of colloidal metal solutions. *Contributions to the optics of turbid media, particularly of colloidal metal solutions Transl. into ENGLISH from Ann. Phys.(Leipzig), v. 25, no. 3, 1908 p 377-445*, 1976. (Cited on pages 15 and 18.)
- [136] M. Rycenga, C. M. Cobley, J. Zeng, W. Li, C. H. Moran, Q. Zhang, D. Qin, and Y. Xia. Controlling the synthesis and assembly of silver nanostructures for plasmonic applications. *Chemical reviews*, 111(6):3669–3712, 2011. (Cited on page 16.)

- [137] J. Zhao, A. O. Pinchuk, J. M. McMahon, S. Li, L. K. Ausman, A. L. Atkinson, and G. C. Schatz. Methods for describing the electromagnetic properties of silver and gold nanoparticles. *Accounts of chemical research*, 41(12):1710–1720, 2008. (Cited on page 16.)
- [138] M. E. Stewart, C. R. Anderton, L. B. Thompson, J. Maria, S. K. Gray, J. A. Rogers, and R. G. Nuzzo. Nanostructured plasmonic sensors. *Chemical reviews*, 108(2):494–521, 2008. (Cited on pages 16 and 19.)
- [139] J. D. Jackson. *Classical electrodynamics*, 1999. (Cited on page 16.)
- [140] P. Drude. Zur elektronentheorie der metalle. *Annalen der physik*, 306(3):566–613, 1900. (Cited on page 17.)
- [141] K. Kneipp, M. Moskovits, and H. Kneipp. *Surface-enhanced Raman scattering: physics and applications*, volume 103. Springer Science & Business Media, 2006. (Cited on page 17.)
- [142] S. K. Srivastava and B. D. Gupta. Fiber optic plasmonic sensors: past, present and future. *The Open Optics Journal*, 7(1), 2013. (Cited on page 18.)
- [143] C. F. Bohren and D. R. Huffman. *Absorption and scattering of light by small particles*. John Wiley & Sons, 2008. (Cited on pages 18, 20, and 87.)
- [144] H. Reddy, U. Guler, A. V. Kildishev, A. Boltasseva, and V. M. Shalaev. Temperature-dependent optical properties of gold thin films. *Optical Materials Express*, 6(9):2776–2802, 2016. (Cited on page 18.)
- [145] S. Link and M. A. El-Sayed. Spectral properties and relaxation dynamics of surface plasmon electronic oscillations in gold and silver nanodots and nanorods, 1999. (Cited on pages 18 and 26.)
- [146] P. Laven. Mieplot (a computer program for scattering of light from a sphere using mie theory & the debye series). <http://www.philiplaven.com/mieplot.htm>, 2011. (Cited on page 19.)
- [147] P. B. Johnson and R. W. Christy. Optical constants of the noble metals. *Physical review B*, 6(12):4370, 1972. (Cited on page 20.)
- [148] A. Curry, G. Nusz, A. Chilkoti, and A. Wax. Substrate effect on refractive index dependence of plasmon resonance for individual silver nanoparticles observed using darkfield micro-spectroscopy. *Optics Express*, 13(7):2668–2677, 2005. (Cited on pages 21, 22, and 44.)
- [149] T. Okamoto. Near-field spectral analysis of metallic beads. In *Near-field optics and surface plasmon polaritons*, pages 97–123. Springer, 2001. (Cited on page 22.)

- [150] K. H. Su, Q. H. Wei, X. Zhang, J. J. Mock, D. R. Smith, and S. Schultz. Interparticle coupling effects on plasmon resonances of nanogold particles. *Nano letters*, 3(8):1087–1090, 2003. (Cited on page 22.)
- [151] D. D. Evanoff, R. L. White, and G. Chumanov. Measuring the distance dependence of the local electromagnetic field from silver nanoparticles. *The Journal of Physical Chemistry B*, 108(5):1522–1524, 2004. (Cited on page 22.)
- [152] M. M. Miller and A. A. Lazarides. Controlling the sensing volume of metal nanosphere molecular sensors. *MRS Online Proceedings Library Archive*, 820, 2004. (Cited on page 22.)
- [153] A. J. Haes and R. P. Van Duyne. A unified view of propagating and localized surface plasmon resonance biosensors. *Analytical and bioanalytical chemistry*, 379(7-8):920–930, 2004. (Cited on page 22.)
- [154] B. Špačková, P. Wrobel, M. Bocková, and J. Homola. Optical biosensors based on plasmonic nanostructures: a review. *Proceedings of the IEEE*, 104(12):2380–2408, 2016. (Cited on pages 23 and 25.)
- [155] M. M. Miller and A. A. Lazarides. Sensitivity of metal nanoparticle surface plasmon resonance to the dielectric environment. *The Journal of Physical Chemistry B*, 109(46):21556–21565, 2005. (Cited on page 23.)
- [156] L. J. Sherry, S. H. Chang, G. C. Schatz, R. P. Van Duyne, B. J. Wiley, and Y. Xia. Localized surface plasmon resonance spectroscopy of single silver nanocubes. *Nano letters*, 5(10):2034–2038, 2005. (Cited on page 25.)
- [157] J. Pérez-Juste, I. Pastoriza-Santos, L. M. Liz-Marzán, and P. Mulvaney. Gold nanorods: synthesis, characterization and applications. *Coordination chemistry reviews*, 249(17-18):1870–1901, 2005. (Cited on page 25.)
- [158] S. Link and M. A. El-Sayed. Shape and size dependence of radiative, non-radiative and photothermal properties of gold nanocrystals. *International reviews in physical chemistry*, 19(3):409–453, 2000. (Cited on page 25.)
- [159] A. D. McFarland and R. P. Van Duyne. Single silver nanoparticles as real-time optical sensors with zeptomole sensitivity. *Nano letters*, 3(8):1057–1062, 2003. (Cited on page 26.)
- [160] M. S Yavuz, Y. Cheng, J. Chen, C. M. Cobley, Q. Zhang, M. Rycenga, J. Xie, C. Kim, K. H. Song, A. G. Schwartz, et al. Gold nanocages covered by smart polymers for controlled release with near-infrared light. *Nature materials*, 8(12):935, 2009. (Cited on page 26.)
- [161] P. E. Chow. *Gold nanoparticles: properties, characterization and fabrication*. Nova Science Publishers, 2010. (Cited on page 26.)

- [162] A. Steinbrück, A. Csaki, G. Festag, and W. Fritzsche. Preparation and optical characterization of core-shell bimetal nanoparticles. *Plasmonics*, 1(1):79, 2006. (Cited on page 26.)
- [163] A. Csaki, T. Schneider, J. Wirth, N. Jahr, A. Steinbrück, O. Stranik, F. Garwe, R. Müller, and W. Fritzsche. Molecular plasmonics: light meets molecules at the nanoscale. *Philosophical Transactions of the Royal Society A: Mathematical, Physical and Engineering Sciences*, 369(1950):3483–3496, 2011. (Cited on page 26.)
- [164] K. H. Song, C. Kim, C. M. Cobley, Y. Xia, and L. V. Wang. Near-infrared gold nanocages as a new class of tracers for photoacoustic sentinel lymph node mapping on a rat model. *Nano letters*, 9(1):183–188, 2008. (Cited on page 26.)
- [165] J. Chen, C. Glaus, R. Laforest, Q. Zhang, M. Yang, M. Gidding, M. J. Welch, and Y. Xia. Gold nanocages as photothermal transducers for cancer treatment. *Small*, 6(7):811–817, 2010. (Cited on page 26.)
- [166] L. Tong, H. Wei, S. Zhang, Z. Li, and H. Xu. Optical properties of single coupled plasmonic nanoparticles. *Physical Chemistry Chemical Physics*, 15(12):4100–4109, 2013. (Cited on page 26.)
- [167] V. A. G. Rivera, F. A. Ferri, and E. Marega Jr. Localized surface plasmon resonances: noble metal nanoparticle interaction with rare-earth ions. In *Plasmonics-Principles and Applications*. IntechOpen, 2012. (Cited on page 26.)
- [168] A. O. Pinchuk, A. M. Kalsin, B. Kowalczyk, G. C. Schatz, and B. A. Grzybowski. Modeling of electrodynamic interactions between metal nanoparticles aggregated by electrostatic interactions into closely-packed clusters. *The Journal of Physical Chemistry C*, 111(32):11816–11822, 2007. (Cited on page 26.)
- [169] M. Chergui, A. Melikyan, and H. Minassian. Calculation of surface plasmon frequencies of two, three, and four strongly interacting nanospheres. *The Journal of Physical Chemistry C*, 113(16):6463–6471, 2009. (Cited on page 26.)
- [170] W. Zhu, R. Esteban, A. G. Borisov, J. J. Baumberg, P. Nordlander, H. J. Lezec, J. Aizpurua, and K. B. Crozier. Quantum mechanical effects in plasmonic structures with subnanometre gaps. *Nature communications*, 7:11495, 2016. (Cited on page 26.)
- [171] R. Esteban, A. G. Borisov, P. Nordlander, and J. Aizpurua. Bridging quantum and classical plasmonics with a quantum-corrected model. *Nature communications*, 3:825, 2012. (Cited on page 26.)
- [172] G. Toscano, S. Raza, A. P. Jauho, N. A. Mortensen, and M Wubs. Modified field enhancement and extinction by plasmonic nanowire dimers due to nonlocal response. 2012. (Cited on page 26.)

- [173] U. Kreibig, A. Althoff, and H. Pressmann. Veiling of optical single particle properties in many particle systems by effective medium and clustering effects. *Surface Science*, 106(1-3):308–317, 1981. (Cited on page 26.)
- [174] U. Kreibig and L. Genzel. Optical absorption of small metallic particles. *Surface Science*, 156:678–700, 1985. (Cited on page 26.)
- [175] A. W. Snyder and J. D. Love. Waveguides with exact solutions. In *Optical Waveguide Theory*, pages 238–279. Springer, 1983. (Cited on pages 27, 28, and 29.)
- [176] C. Yeh and F. I. Shimabukuro. *The essence of dielectric waveguides*. Springer, 2008. (Cited on page 27.)
- [177] F. M. Cox, A. Argyros, and M. C. J. Large. Liquid-filled hollow core microstructured polymer optical fiber. *Optics Express*, 14(9):4135–4140, 2006. (Cited on page 30.)
- [178] S. Smolka, M. Barth, and O. Benson. Highly efficient fluorescence sensing with hollow core photonic crystal fibers. *Optics Express*, 15(20):12783–12791, 2007. (Cited on page 30.)
- [179] C. I. L. Justino, A. C. Freitas, R. Pereira, A. C. Duarte, and T. A. P. Rocha Santos. Recent developments in recognition elements for chemical sensors and biosensors. *TrAC Trends in Analytical Chemistry*, 68:2–17, 2015. (Cited on page 32.)
- [180] J. P. Chambers, B. P. Arulanandam, L. L. Matta, A. Weis, and J. J. Valdes. Biosensor recognition elements. Technical report, Texas Univ at San Antonio Dept of Biology, 2008. (Cited on page 32.)
- [181] Y. K. Cho, S. Kim, Y. A. Kim, H. K. Lim, K. Lee, D. S. Yoon, G. Lim, Y. E. Pak, T. H. Ha, and K. Kim. Characterization of DNA immobilization and subsequent hybridization using in situ quartz crystal microbalance, fluorescence spectroscopy, and surface plasmon resonance. *Journal of colloid and interface science*, 278(1):44–52, 2004. (Cited on page 32.)
- [182] J. Wang. Survey and summary: From DNA biosensors to gene chips. *Nucleic acids research*, 28(16):3011–3016, 2000. (Cited on page 32.)
- [183] J. P. Rast, G. Amore, C. Calestani, C. B. Livi, A. Ransick, and E. H. Davidson. Recovery of developmentally defined gene sets from high-density cDNA macroarrays. *Developmental biology*, 228(2):270–286, 2000. (Cited on page 33.)
- [184] N. Prabhakar, K. Arora, S. P. Singh, H. Singh, and B. D. Malhotra. DNA entrapped polypyrrole–polyvinyl sulfonate film for application to electrochemical biosensor. *Analytical biochemistry*, 366(1):71–79, 2007. (Cited on page 33.)

- [185] K. Arora, N. Prabhakar, S. Chand, and B. D. Malhotra. E scherichia coli geno-sensor based on polyaniline. *Analytical Chemistry*, 79(16):6152–6158, 2007. (Cited on page 33.)
- [186] H. Ravan, S. Kashanian, N. Sanadgol, A. Badoei-Dalfard, and Z. Karami. Strategies for optimizing DNA hybridization on surfaces. *Analytical biochemistry*, 444:41–46, 2014. (Cited on page 33.)
- [187] J. Liu. Adsorption of DNA onto gold nanoparticles and graphene oxide: surface science and applications. *Physical Chemistry Chemical Physics*, 14(30):10485–10496, 2012. (Cited on pages 33 and 35.)
- [188] X. Zhang, B. Liu, N. Dave, M. R. Servos, and J. Liu. Instantaneous attachment of an ultrahigh density of nonthiolated DNA to gold nanoparticles and its applications. *Langmuir*, 28(49):17053–17060, 2012. (Cited on pages 33 and 89.)
- [189] L. Pray. Discovery of DNA structure and function: Watson and Crick. *Nature Education*, 1(1):100, 2008. (Cited on page 34.)
- [190] J. D. Watson, F. H. C. Crick, et al. Molecular structure of nucleic acids. *Nature*, 171(4356):737–738, 1953. (Cited on page 34.)
- [191] A. W. Peterson, R. J. Heaton, and R. M. Georgiadis. The effect of surface probe density on dna hybridization. *Nucleic acids research*, 29(24):5163–5168, 2001. (Cited on page 34.)
- [192] O. Tokel and U. Inci, F. and Demirci. Advances in plasmonic technologies for point of care applications. *Chemical reviews*, 114(11):5728–5752, 2014. (Cited on page 34.)
- [193] F. R. R. Teles and L. P. Fonseca. Trends in DNA biosensors. *Talanta*, 77(2):606–623, 2008. (Cited on page 34.)
- [194] K. A. Peterlinz, R. M. Georgiadis, T. M. Herne, and M. J. Tarlov. Observation of hybridization and dehybridization of thiol-tethered DNA using two-color surface plasmon resonance spectroscopy. *Journal of the American Chemical Society*, 119(14):3401–3402, 1997. (Cited on page 34.)
- [195] J. C. Love, L. A. Estroff, J. K. Kriebel, R. G. Nuzzo, and G. M. Whitesides. Self-assembled monolayers of thiolates on metals as a form of nanotechnology. *Chemical reviews*, 105(4):1103–1170, 2005. (Cited on page 34.)
- [196] T. M. Herne and M. J. Tarlov. Characterization of DNA probes immobilized on gold surfaces. *Journal of the American Chemical Society*, 119(38):8916–8920, 1997. (Cited on page 35.)

- [197] R. Georgiadis, K. P. Peterlinz, and A. W. Peterson. Quantitative measurements and modeling of kinetics in nucleic acid monolayer films using SPR spectroscopy. *Journal of the American Chemical Society*, 122(13):3166–3173, 2000. (Cited on page 35.)
- [198] R. Levicky, T. M. Herne, M. J. Tarlov, and S. K. Satija. Using self-assembly to control the structure of DNA monolayers on gold: a neutron reflectivity study. *Journal of the American Chemical Society*, 120(38):9787–9792, 1998. (Cited on page 35.)
- [199] H. D. Hill, J. E. Millstone, M. J. Banholzer, and C. A. Mirkin. The role radius of curvature plays in thiolated oligonucleotide loading on gold nanoparticles. *ACS nano*, 3(2):418–424, 2009. (Cited on page 35.)
- [200] A. B. Steel, R. L. Levicky, T. M. Herne, and M. J. Tarlov. Immobilization of nucleic acids at solid surfaces: effect of oligonucleotide length on layer assembly. *Biophysical journal*, 79(2):975–981, 2000. (Cited on page 35.)
- [201] S. Tombelli, M. Minunni, and M. Mascini. Analytical applications of aptamers. *Biosensors and Bioelectronics*, 20(12):2424–2434, 2005. (Cited on page 36.)
- [202] A. Jung, I. Stemmler, A. Brecht, and G. Gauglitz. Covalent strategy for immobilization of DNA-microspots suitable for microarrays with label-free and time-resolved optical detection of hybridization. *Fresenius' journal of analytical chemistry*, 371(2):128–136, 2001. (Cited on page 36.)
- [203] H. J. Watts, D. Yeung, and H. Parkes. Real-time detection and quantification of dna hybridization by an optical biosensor. *Analytical chemistry*, 67(23):4283–4289, 1995. (Cited on page 36.)
- [204] M. Chemnitz, M. Zeisberger, and M. A. Schmidt. Performance limits of single nano-object detection with optical fiber tapers. *JOSA B*, 34(9):1833–1841, 2017. (Cited on pages 37 and 42.)
- [205] M. D. O'Donnell, K. Richardson, R. Stolen, A. B. Seddon, D. Furniss, V. K. Tikhomirov, C. Rivero, M. Ramme, R. Stegeman, G. Stegeman, et al. Tellurite and fluorotellurite glasses for fiberoptic Raman amplifiers: glass characterization, optical properties, Raman gain, preliminary fiberization, and fiber characterization. *Journal of the American Ceramic Society*, 90(5):1448–1457, 2007. (Cited on pages 38 and 39.)
- [206] S. Selleri, E. Coscelli, M. Sozzi, A. Cucinotta, F. Poli, and D. Passaro. Air-suspended solid-core fibers for sensing. In *Optical Sensors 2009*, volume 7356, page 73561L. International Society for Optics and Photonics, 2009. (Cited on page 38.)
- [207] R. KostECKI, H. Ebendorff-Heidepriem, C. Davis, G. McAdam, S. C. Warren-Smith, and T. M. Monro. Silica exposed-core microstructured optical fibers. *Optical Materials Express*, 2(11):1538–1547, 2012. (Cited on pages 38 and 52.)



- [208] H. Ebendorff-Heidepriem, S. C. Warren-Smith, and T. M. Monro. Suspended nanowires: fabrication, design and characterization of fibers with nanoscale cores. *Optics Express*, 17(4):2646–2657, 2009. (Cited on pages 38 and 47.)
- [209] W. Sellmeier. Zur erkarung der abnormen farbenfolge im spectrum einiger. substanzen. *Annalen der Physik und Chemie*, 219:272–282, 1871. (Cited on page 39.)
- [210] G. Ghosh, M. Endo, and T. Iwasaki. Temperature-dependent sellmeier coefficients and chromatic dispersions for some optical fiber glasses. *Journal of Lightwave Technology*, 12(8):1338–1342, 1994. (Cited on page 39.)
- [211] F. Warken, E. Vetsch, D. Meschede, M. Sokolowski, and A. Rauschenbeutel. Ultra-sensitive surface absorption spectroscopy using sub-wavelength diameter optical fibers. *Optics Express*, 15(19):11952–11958, 2007. (Cited on page 42.)
- [212] T. Ung, L. M. Liz-Marzan, and P. Mulvaney. Gold nanoparticle thin films. *Colloids and surfaces A: Physicochemical and engineering aspects*, 202(2-3):119–126, 2002. (Cited on page 48.)
- [213] V. A. Markel. Introduction to the Maxwell Garnett approximation: tutorial. *JOSA A*, 33(7):1244–1256, 2016. (Cited on page 48.)
- [214] X. Li, L. V. Nguyen, Y. Zhao, H. Ebendorff-Heidepriem, and S. C. Warren-Smith. High-sensitivity Sagnac-interferometer biosensor based on exposed core microstructured optical fiber. *Sensors and Actuators B: Chemical*, 269:103–109, 2018. (Cited on pages 49, 78, 96, and 99.)
- [215] P. J. A. Sazio, A. Amezcua-Correa, C. E. Finlayson, J. R. Hayes, T. J. Scheidemantel, N. F. Baril, B. R. Jackson, D. J. Won, F. Zhang, E. R. Margine, et al. Microstructured optical fibers as high-pressure microfluidic reactors. *Science*, 311(5767):1583–1586, 2006. (Cited on page 50.)
- [216] X. Zhang, R. Wang, F. M. Cox, B. T. Kuhlmeier, and M. C. J. Large. Selective coating of holes in microstructured optical fiber and its application to in-fiber absorptive polarizers. *Optics express*, 15(24):16270–16278, 2007. (Cited on page 50.)
- [217] F. M. Cox, A. Argyros, M. C. J. Large, and S. Kalluri. Surface enhanced raman scattering in a hollow core microstructured optical fiber. *Optics Express*, 15(21):13675–13681, 2007. (Cited on page 50.)
- [218] D. K. Schwartz. Mechanisms and kinetics of self-assembled monolayer formation. *Annual review of physical chemistry*, 52(1):107–137, 2001. (Cited on page 50.)
- [219] K. A. Peterlinz and R. Georgiadis. In situ kinetics of self-assembly by surface plasmon resonance spectroscopy. *Langmuir*, 12(20):4731–4740, 1996. (Cited on page 50.)

- [220] P. Russell. Photonic crystal fibers. *science*, 299(5605):358–362, 2003. (Cited on page 51.)
- [221] J. C. Knight, T. A. Birks, P. St. J. Russell, and D. M. Atkin. All-silica single-mode optical fiber with photonic crystal cladding. *Optics letters*, 21(19):1547–1549, 1996. (Cited on page 51.)
- [222] E. P. Schartner, A. Dowler, and H. Ebendorff-Heidepriem. Fabrication of low-loss, small-core exposed core microstructured optical fibers. *Optical Materials Express*, 7(5):1496–1502, 2017. (Cited on pages 52, 70, 79, and 92.)
- [223] J. Turkevich, P. C. Stevenson, and J. Hillier. A study of the nucleation and growth processes in the synthesis of colloidal gold. *Discussions of the Faraday Society*, 11:55–75, 1951. (Cited on pages 53 and 60.)
- [224] G. Frens. Controlled nucleation for the regulation of the particle size in monodisperse gold suspensions. *Nature physical science*, 241(105):20, 1973. (Cited on pages 53 and 60.)
- [225] K. R. Brown, D. G. Walter, and M. J. Natan. Seeding of colloidal Au nanoparticle solutions. 2. improved control of particle size and shape. *Chemistry of Materials*, 12(2):306–313, 2000. (Cited on page 53.)
- [226] S. K. Sivaraman, S. Kumar, and V. Santhanam. Monodisperse sub-10 nm gold nanoparticles by reversing the order of addition in Turkevich method—The role of chloroauric acid. *Journal of colloid and Interface Science*, 361(2):543–547, 2011. (Cited on page 53.)
- [227] B. K. Pong, H. I. Elim, J. X. Chong, W. Ji, B. L. Trout, and J. Y. Lee. New insights on the nanoparticle growth mechanism in the citrate reduction of gold (iii) salt: formation of the Au nanowire intermediate and its nonlinear optical properties. *The Journal of Physical Chemistry C*, 111(17):6281–6287, 2007. (Cited on page 53.)
- [228] S. Kumar, J. Aaron, and K. Sokolov. Directional conjugation of antibodies to nanoparticles for synthesis of multiplexed optical contrast agents with both delivery and targeting moieties. *Nature protocols*, 3(2):314, 2008. (Cited on page 54.)
- [229] T. Franzl, D. S. Koktysh, T. A. Klar, A. L. Rogach, J. Feldmann, and N. Gaponik. Fast energy transfer in layer-by-layer assembled cdte nanocrystal bilayers. *Applied Physics Letters*, 84(15):2904–2906, 2004. (Cited on page 60.)
- [230] B. Doherty. *Plasmonic nanoparticles in microstructured fibres*. Master’s thesis, Friedrich-Schiller-Universität, Jena, 2015. (Cited on page 62.)
- [231] S. A. Maier, M. L. Brongersma, P. G. Kik, and H. A. Atwater. Observation of near-field coupling in metal nanoparticle chains using far-field polarization spectroscopy. *Physical Review B*, 65(19):193408, 2002. (Cited on page 69.)

- [232] S. C. Warren-Smith, R. KostECKI, L. V. Nguyen, and T. M. Monro. Fabrication, splicing, bragg grating writing, and polyelectrolyte functionalization of exposed-core microstructured optical fibers. *Optics express*, 22(24):29493–29504, 2014. (Cited on pages 78, 79, and 99.)
- [233] A. Csáki, O. Stranik, and W. Fritzsche. Localized surface plasmon resonance based biosensing. *Expert review of molecular diagnostics*, 18(3):279–296, 2018. (Cited on page 84.)
- [234] S. Thamm, A. Csaki, and W. Fritzsche. LSPR detection of nucleic acids on nanoparticle monolayers. In *DNA Nanotechnology*, pages 163–171. Springer, 2018. (Cited on page 85.)
- [235] J. Jatschka, A. Dathe, A. Csáki, W. Fritzsche, and O. Stranik. Propagating and localized surface plasmon resonance sensing—A critical comparison based on measurements and theory. *Sensing and bio-sensing research*, 7:62–70, 2016. (Cited on page 85.)
- [236] A. B. Dahlin, J. O. Tegenfeldt, and F. Höök. Improving the instrumental resolution of sensors based on localized surface plasmon resonance. *Analytical chemistry*, 78(13):4416–4423, 2006. (Cited on pages 85 and 87.)
- [237] J. Jatschka. *Detection of small biomolecules by plasmonic nanoparticles (LSPR-sensing)*. PhD thesis, Friedrich-Schiller-Universität, Jena, 2018. (Cited on page 87.)
- [238] S. C. Warren-Smith, H. Ebendorff-Heidepriem, T. C. Foo, R. Moore, C. Davis, and T. M. Monro. Exposed-core microstructured optical fibers for real-time fluorescence sensing. *Optics Express*, 17(21):18533–18542, 2009. (Cited on page 96.)
- [239] S. C. Warren-Smith, M. Chemnitz, H. Schneidewind, R. KostECKI, H. Ebendorff-Heidepriem, T. M. Monro, and M. A. Schmidt. Nanofilm-induced spectral tuning of third harmonic generation. *Optics letters*, 42(9):1812–1815, 2017. (Cited on page 96.)
- [240] H. Sugimura, K. Ushiyama, A. Hozumi, and O. Takai. Micropatterning of alkyl- and fluoroalkylsilane self-assembled monolayers using vacuum ultraviolet light. *Langmuir*, 16(3):885–888, 2000. (Cited on page 98.)
- [241] H. Sugimura and N. Nakagiri. Nanoscopic surface architecture based on scanning probe electrochemistry and molecular self-assembly. *Journal of the American Chemical Society*, 119(39):9226–9229, 1997. (Cited on page 98.)
- [242] T. Sato, D. G. Hasko, and H. Ahmed. Nanoscale colloidal particles: Monolayer organization and patterning. *Journal of Vacuum Science & Technology B: Microelectronics and Nanometer Structures Processing, Measurement, and Phenomena*, 15(1):45–48, 1997. (Cited on page 98.)

- [243] M. Bhagawati, C. You, and J. Piehler. Quantitative real-time imaging of protein–protein interactions by LSPR detection with micropatterned gold nanoparticles. *Analytical chemistry*, 85(20):9564–9571, 2013. (Cited on page 98.)
- [244] S. Horikoshi, H. Abe, K. Torigoe, M. Abe, and N. Serpone. Access to small size distributions of nanoparticles by microwave-assisted synthesis. formation of Ag nanoparticles in aqueous carboxymethylcellulose solutions in batch and continuous-flow reactors. *Nanoscale*, 2(8):1441–1447, 2010. (Cited on page 98.)
- [245] I. Bilecka and M. Niederberger. Microwave chemistry for inorganic nanomaterials synthesis. *Nanoscale*, 2(8):1358–1374, 2010. (Cited on page 98.)
- [246] N. N. Mallikarjuna and R. S. Varma. Microwave-assisted shape-controlled bulk synthesis of noble nanocrystals and their catalytic properties. *Crystal growth & design*, 7(4):686–690, 2007. (Cited on page 98.)
- [247] S. Yüksel, A. M. Schwenke, G. Soliveri, S. Ardizzone, K. Weber, D. Cialla-May, S. Hoepfener, U. S. Schubert, and J. Popp. Trace detection of tetrahydrocannabinol (THC) with a SERS-based capillary platform prepared by the in situ microwave synthesis of AgNPs. *Analytica chimica acta*, 939:93–100, 2016. (Cited on page 98.)
- [248] G. Soliveri, S. Ardizzone, S. Yüksel, D. Cialla-May, J. Popp, U. S. Schubert, and S. Hoepfener. Microwave-assisted silver nanoparticle film formation for SERS applications. *The Journal of Physical Chemistry C*, 120(2):1237–1244, 2016. (Cited on page 98.)
- [249] N. P. Mauranyapin, L. S. Madsen, L. Booth, L. Peng, S. C. Warren-Smith, E. P. Schartner, H. Ebendorff-Heidepriem, and W. P. Bowen. Quantum noise limited nanoparticle detection with exposed-core fiber. *Optics Express*, 27(13):18601–18611, 2019. (Cited on page 100.)
- [250] P. Wang, Y. Wang, Z. Yang, X. Guo, X. Lin, X. C. Yu, Y. F. Xiao, W. Fang, L. Zhang, G. Lu, et al. Single-band 2-nm-line-width plasmon resonance in a strongly coupled Au nanorod. *Nano letters*, 15(11):7581–7586, 2015. (Cited on page 100.)
- [251] C. Fattinger. Focal molography: coherent microscopic detection of biomolecular interaction. *Physical Review X*, 4(3):031024, 2014. (Cited on page 100.)
- [252] A. Frutiger, Y. Blickenstorfer, S. Bischof, C. Forró, M. Lauer, V. Gatterdam, C. Fattinger, and J. Vörös. Principles for sensitive and robust biomolecular interaction analysis: The limits of detection and resolution of diffraction-limited focal molography. *Physical Review Applied*, 11(1):014056, 2019. (Cited on page 100.)

## ACKNOWLEDGEMENTS

---

A PhD benefits greatly from a broad behind-the-scenes support network. I would therefore like to thank everyone that supported me during my doctoral journey, those who were with me from the beginning and those who joined along the way. In particular I want to express my gratitude to the following individuals:

Prof. Dr. Markus Schmidt for his scientific guidance and supervision throughout my entire PhD time. For the weekly Monday morning meetings and steadfast enthusiasm for science.

Apl. Prof. Dr. Wolfgang Fritzsche for his ever available support, for introducing me to this topic, and for the opportunity to work in his many labs.

Dr. Andrea Csáki in particular for the many chemistry and biology related discussions. For acting as a second supervisor and supporting me through many new chemistry endeavours. Her contributions were invaluable.

Dr. Matthias Thiele who instructed me on NP fabrication and provided a ready supply of everything. He was my organisational role model.

Franka Jahn for the limitless provision of SEM images of NPs and fibres.

Dr. David Zopf for use of the eLSPR system, fruitful microfluidic and plasmonic discussions, and “no worries” attitude in stressful times.

Dr. Anka Schuchow who introduced me to many fibre measurement techniques.

Dr. Stephen Warren-Smith, who brought the ECF used in this work to IPHT. For his splicing guidance and MOF related discussions.

Dr. Mario Chemnitz for random German clarifications and microfluidic brainstorming.

Dr. Alessandro Tuniz for our time together as the Monday morning plasmonics meeting.

My students Mona Nissen and Miguel Lorenzo, for their valuable work on tricky topics.

Dr. Dorit Schmidt, for career and life advice and always being there to help.

The entire Nanobiophotonics group and PhDs for their terrific scientific attitude and inclusion.

All of my former and recent colleagues for the great time together as the Fibre Photonics group.

The members and organisers of GRK 2101 on both sides for the opportunity for broader scientific development and networking.

Dr. Sina Saravi for every time I forgot something about science, for keeping me grounded and reminding me how ‘clean and green’ Jena is.

Finally, I thank my friends and family for the unwavering support and adventures during my PhD, and for sticking by me through the years of academia.

**Journal articles**

1. M. Nissen, **B. Doherty**, J. Hamperl, J. Kobelke, K. Weber, T. Henkel and M. A. Schmidt, "UV absorption spectroscopy in water-filled antiresonant hollow core fibers for pharmaceutical detection," *Sensors* 18.2, 478 (2018).
2. **B. Doherty**, M. Thiele, S. Warren-Smith, E. Schartner, H. Ebendorff-Heidepriem, W. Fritzsche, and M. A. Schmidt, "Plasmonic nanoparticle-functionalized exposed core fiber – an optofluidic refractive index sensing platform," *Opt. Lett.* 42, 4395 (2017).
3. **B. Doherty**, A. Csáki, M. Thiele, M. Zeisberger, A. Schwuchow, J. Kobelke, W. Fritzsche, and M. A. Schmidt, "Nanoparticle functionalised small-core suspended-core fibre – a novel platform for efficient sensing," *Biomed. Opt. Express* 8, 790 (2017).
4. T. Wieduwilt, M. Zeisberger, M. Thiele, **B. Doherty**, M. Chemnitz, A. Csaki, W. Fritzsche, and M. A. Schmidt, "Gold-reinforced silver nanoprisms on optical fiber tapers – a new base for high precision sensing," *APL Photonics* 1(6), 066102 (2016).
5. C. Franke, O. Stenzel, S. Wilbrandt, M. Schürmann, J. Wolf, V. Todorova, **B. Doherty**, N. Kaiser, "Charakterisierung der optischen Konstanten von Substraten für den NIR/MIR-Spektralbereich," *Wiley-VCH - Vakuum in Forschung und Praxis* 28.1, 28 (2016).

**Conference proceedings**

1. **B. Doherty**, and M. A. Schmidt, "Plasmonic microstructured fibres for biosensing," in NSERC CREATE Guided Light, Photonics North, (Montréal, CA, 2018).
2. **B. Doherty**, and M. A. Schmidt, "Plasmonic nanoparticles in microstructured fibres as detection platforms," in NanoBioSensors, (TU Dresden, DE, 2017).
3. **B. Doherty**, and M. A. Schmidt, "Plasmonic small-core microstructured fibres," in GRK Autumn School, (Centre d'Optique, Photonique et Laser (COPL), CA, 2017).
4. **B. Doherty**, and M. A. Schmidt, "Plasmonic nanoparticles in microstructured fibres as detection platforms," in Doctoral Conference, Dornburg Seminars, (Dornburg, DE, 2017).
5. **B. Doherty**, Andrea Csáki and M. A. Schmidt, "Plasmonic fibres for detecting human-relevant microbial water contaminants," in Doctoral Conference on Optics DokDok, Dornburg Seminars, (Dornburg, DE, 2015).

## EHRENWÖRTLICHE ERKLÄRUNG

---

Ich erkläre hiermit ehrenwörtlich, dass ich die vorliegende Arbeit selbstständig, ohne unzulässige Hilfe Dritter und ohne Benutzung anderer als der angegebenen Hilfsmittel und Literatur angefertigt habe. Die aus anderen Quellen direkt oder indirekt übernommenen Daten und Konzepte sind unter Angabe der Quelle gekennzeichnet.

Bei der Auswahl und Auswertung folgenden Materials haben mir die nachstehend aufgeführten Personen in der jeweils beschriebenen Weise unentgeltlich geholfen:

1. Franka Jahn, Leibniz-IPHT Jena, durch die Erstellung der REM-Bilder.
2. Dr. Matthias Thiele, Leibniz-IPHT Jena, durch die Bereitstellung von Nanopartikeln.
3. Dr. Jens Kobelke, Leibniz-IPHT Jena, durch die Herstellung von SC-MOF.
4. Dr. Eric Schartner and Prof. Heike Ebendorff-Heidepriem, University of Adelaide, durch die Herstellung von ECF.

Weitere Personen waren an der inhaltlich-materiellen Erstellung der vorliegenden Arbeit nicht beteiligt. Insbesondere habe ich hierfür nicht die entgeltliche Hilfe von Vermittlungs- bzw. Beratungsdiensten (Promotionsberater oder andere Personen) in Anspruch genommen. Niemand hat von mir unmittelbar oder mittelbar geldwerte Leistungen für Arbeiten erhalten, die im Zusammenhang mit dem Inhalt der vorgelegten Dissertation stehen.

Die Arbeit wurde bisher weder im In- noch Ausland in gleicher oder ähnlicher Form einer anderen Prüfungsbehörde vorgelegt.

Die geltende Promotionsordnung der Physikalisch-Astronomischen Fakultät ist mir bekannt. Ich versichere ehrenwörtlich, dass ich nach bestem Wissen die reine Wahrheit gesagt und nichts verschwiegen habe.

Jena, 8th October 2019

---

Brenda Doherty